UTTAC-72, 2004

ANNUAL REPORT

April 1, 2003 – March 31, 2004

TANDEM ACCELERATOR CENTER
UNIVERSITY OF TSUKUBA

http://www.tac.tsukuba.ac.jp/

PREFACE

This annual report covers the work carried out at University of Tsukuba Tandem Accelerator Center (UTTAC) during the fiscal year 2003 (1 April 2003 ~ 31 March 2004). The two tandem accelerators, 12UD Pelletron and 1MV Tandetron, have been operated stably throughout this period, except for several small troubles.

The main research field with 12UD Pelletron has recently been shifted to the applied accelerator category from rather fundamental, physics-directed sciences. The accelerator mass spectroscopy of ^{36}Cl has been refined and applied to environmental studies. The hydrogen recoil detection analysis of mineral samples has been continued in collaboration with geologists. Irradiation effects of fast heavy ions in the electronic stopping range were applied to fabrication of 3-dimensional nano/microstructure of TiO_2. On the other hand, the fundamental studies of nuclear, atomic, as well as condensed-matter physics are in steady progress. In nuclear physics, the total-reaction cross section for protons on ^{12}C near the (p,n) threshold and the analyzing powers in the ^{6}Li(d,p)^{7}Li reaction at 90 keV were studied. A polarized deuteron target was developed for measurement of spin-correlation parameters in D(d,p) reaction at 20 MeV. In atomic and condensed-matter physics, fundamental data of non-equilibrium charge states of swift heavy ions are being accumulated for detailed understanding of the collision-induced charge changing processes.

The 1MV Tandetron has been used routinely for Rutherford backscattering spectroscopy (RBS) of synthesized semiconductor and magnetic films, and for trace-element analysis by particle induced X-ray emission (PIXE). Besides such applied use, we have successfully accelerated B, C, Al, Si, and Cu cluster ions at MeV energies and provided for challenging studies of cluster-surface electronic interactions.

In the end of this fiscal year, UTTAC successfully organized two workshops entitled *Unstable Nuclei and Nuclear Synthesis with Storage Ring*, and *Electronic Excitation and Related Phenomena in Atomic Collisions*. Also, eighteen UTTAC seminars were held to stimulate research activities and to exchange academic information. Notably, UTTAC accepted a series of accelerator-facility tour for totally ~700 visitors this year, of which 390 are high-school students. Such "open-facility" service is of social importance for promotion of natural science, especially in the next generation.

The former director of UTTAC, Professor Kohei Furuno, retired from his duty, effective on 1 April 2003. His long-term effort for development and maintenance of the UTTAC facility is greatly acknowledged. UTTAC restarted this spring as Applied Accelerator Division of Research Facility Center for Science and Technology. The familiar name UTTAC will be used as before, with *C*enter replaced by *C*omplex (means multi-accelerator facility).

Hiroshi Kudo
Director

CONTENTS

4. ION BEAM APPLICATION

1.1 Accelerator operation 2003

K. Sasa, K. Shima, T. Komatsubara, S. Ishii, H. Kimura, H. Oshima, Y. Tajima, T. Takahashi, Y. Yamato and H. Kudo.

The 12UD Pelletron tandem accelerator

The total operating time and the experimental beam time were 2047.5 and 1475.4 hours, respectively. The operating time was about 102 % relative to that in 2002. Figure 1 shows the accelerator operation hours per month. The beam time histogram with respect to the terminal voltage is shown in Figure 2. Figure 3 represents percentage operation time of the three ion sources and ion species. Figure 4 shows the percentage of experimental beam time of the running research fields.

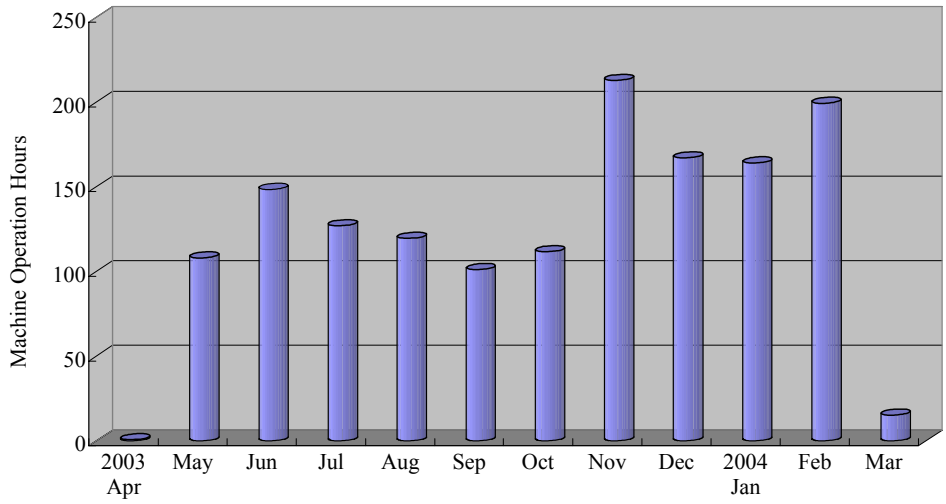

Figure 1. Accelerator operation hours per month for the fiscal year 2003.

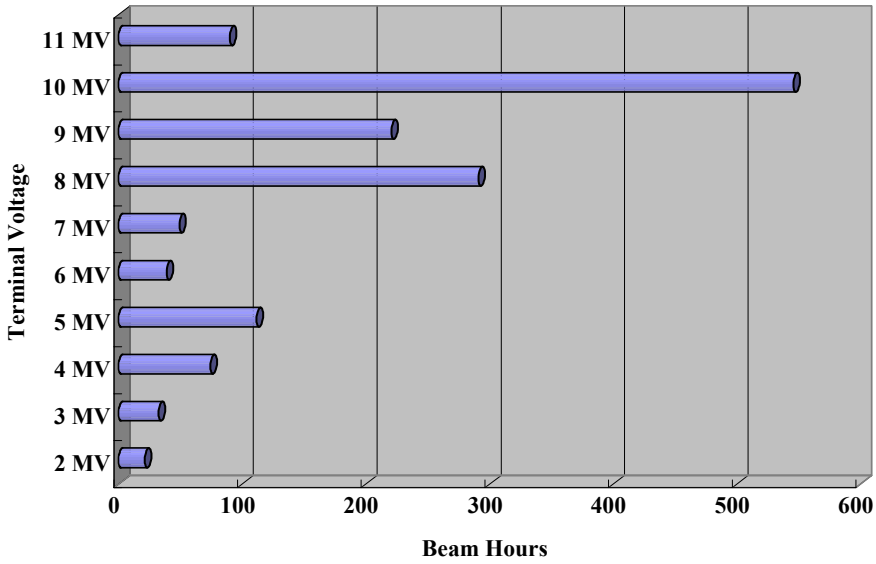

Figure 2. Beam time histogram as a function of the terminal voltage.

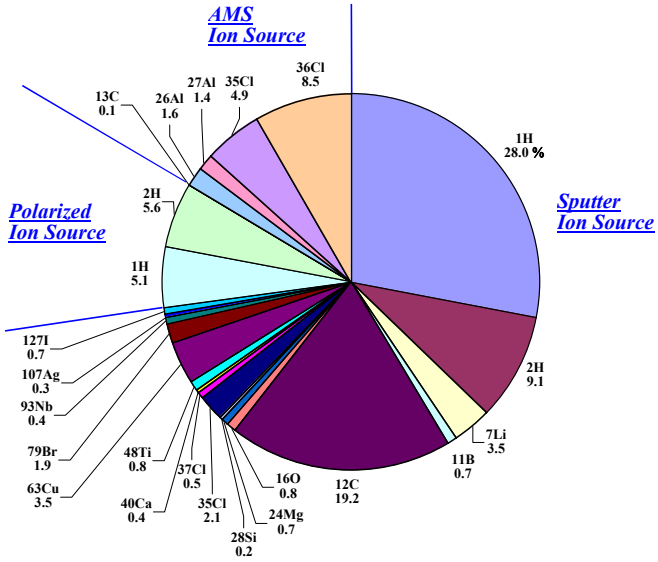

Figure 3. Percentage operation hours of the three ion sources.

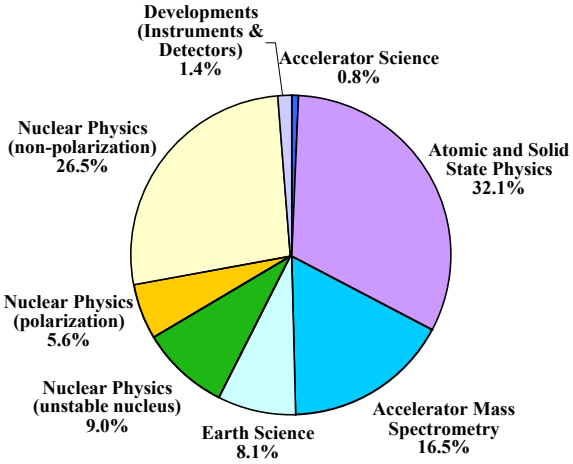

Figure 4. Percentage experimental beam time of the research fields.

The scheduled maintenance was finished on April 1, 2003. After high-voltage conditioning, the beams have been provided for experiments since May 10. The operation of the 12UD Pelletron tandem accelerator was in stable operation at the terminal voltage of lower than 10.5 MV in the year 2003. When the terminal voltage is increased to 11MV, the accelerating tubes in the first and second units on the low energy side have been troubled in the last few years. In the middle of 2003, the terminal voltage could not be increased more than 10.5 MV. We observed continuous fluctuation of corona currents and X-ray bursts without shorting the first and second units. High voltage conditionings did not suppress these phenomena.

The scheduled maintenance in the spring 2004 was started on March 3 and finished on April 9. We replaced the compressed type accelerating tubes by the standard type in the first and second units on the low energy side at this time. Figure 5 shows the old and new arrangements of accelerating tubes in the first and second units. Another major works of this maintenance were as follows. All corona points were

renewed along the column and the accelerating tube. Stripper foils in the foil unit-A and B were also replaced by new foils. We repaired the oiling system, the shorting rod contacts, and the insulating sheets of the chain pulley. The vacuum system of the analyzing magnet was modified by replacing the turbo molecular pump by the ion pump. The power supplies for quadrupole magnets in the second target room have also been renewed. The 1000 kg SF_6 gas was added to the main accelerator tank during the scheduled maintenance.

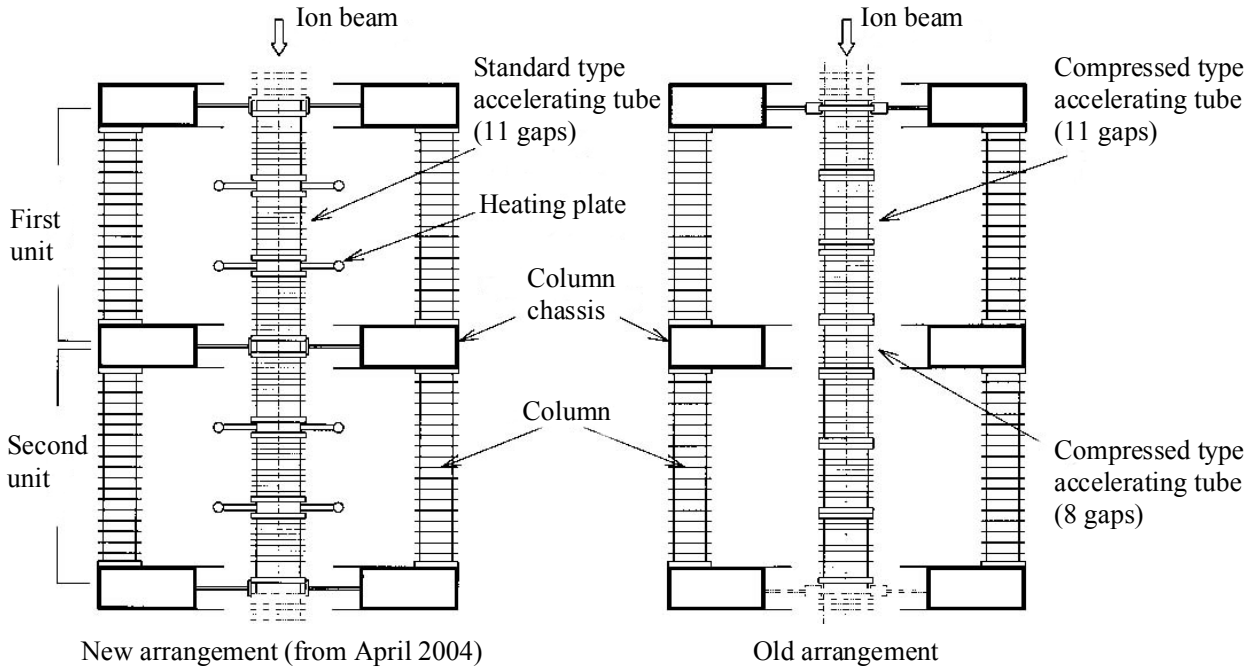

Figure 5. Old and new arrangements of accelerating tubes in the first and second units.

The 1MV Tandetron accelerator

The total operation time of the 1MV Tandetron accelerator was 347 hours in the fiscal year 2003. While the usual run for RBS material analysis has been continued throughout the year, the experiments with cluster beams have been increased drastically since C_n (n=1-8) beams of equal velocity (0.24 MeV/u) have been successfully provided on June 2003. This technical development allowed us to start a research program, “Fast cluster impact processes”, including electron emission, sputtering, radiation damage, secondary particle emission. Surely, these are well known phenomena, but our knowledge is restricted only for impact of single-atom (n=1) ions. So far unknown aspects of these phenomena might be revealed by cluster impacts through the nano-space perturbation that are never realized by single-atom or small molecular ions. For this research program, a variety of cluster beams are required. The transport conditions of the cluster beams have been investigated in detail and are summarized in Table 1.

Table 1. Experimental conditions of high-energy cluster ions for the B (11°) and C (15°) beam courses.

Beam course	Energy		$^{11}B_1^+$	B_2^+	B_3^+	B_4^+
15°	29.1 keV/u	320 keV/atom	●	●	●	●
	43.6 keV/u	480 keV/atom	●	●	●	●

Beam course	Energy		$^{12}C_1^+$	C_2^+	C_3^+	C_4^+	C_5^+	C_6^+	C_7^+	C_8^+
11°	20 keV/u	240 keV/atom	●	●	●	●	●	●	●	●
	30 keV/u	360 keV/atom	●	●	●	●	●			
	42 keV/u	504 keV/atom	●	●	●	●				

Beam course	Energy		$^{27}Al_1^+$	Al_2^+	Al_3^+	Al_4^+
11°	8.89 keV/u	240 keV/atom	●	●	●	●

Beam course	Energy		$^{28}Si_1^+$	Si_2^+	Si_3^+	Si_4^+
11°	8.57 keV/u	240 keV/atom	●	●	●	●

Beam course	Energy		$^{63}Cu_1^+$	$^{63}Cu_2^+$
15°	7.62 keV/u	480 keV/atom	●	●

References

[1] K. Sasa et al., UTTAC71 (2003) 1.

1.2 Design of laser coupling with a compact 2.45 GHz ECR ion source

K. Sasa

A compact 2.45 GHz electron cyclotron resonance (ECR) ion source was installed for a second stage of a hybrid ion source [1] as a charge state multiplier and a stable beam extractor. Particles extracted from the solid sample by the laser ablation have a broad energy distribution and an unstable beam flux. Once the sample materials produced by the laser ablation are trapped in the ECR plasma, the efficient production of highly charged ions in the ECR plasma ensures the elimination of molecular ions or micro-particles.

The simple structure of the compact 2.45 GHz ECR ion source was originated by E. Tojyo [2]. The magnetic field is given by two pieces of Nd-Fe-B permanent magnets, corresponding to a closed resonance surface of 875 Gauss. A 2.45GHz microwave power and supporting gas are supplied into the plasma chamber in the transverse direction. The inner diameter and the length of the plasma chamber are designed to 32 mm and 72 mm, respectively. Figure 1 shows the cross-sectional view of the laser coupling with a compact 2.45 GHz ECR ion source. Table 1 shows the main characteristics of the compact 2.45 GHz ECR ion source.

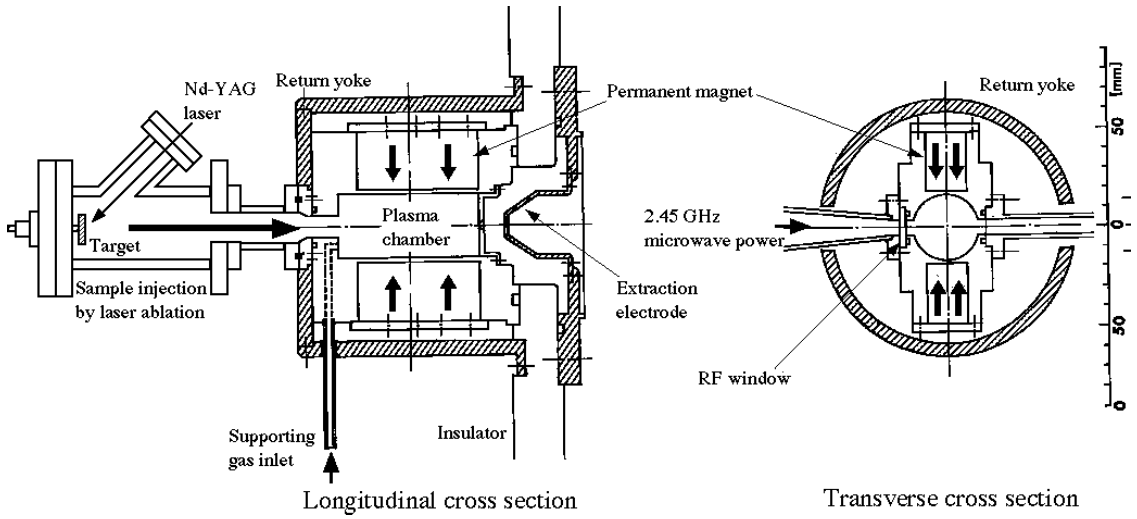

Figure 1. Cross-sectional view of the laser coupling with a compact 2.45 GHz ECR ion source.

Table 1 Main characteristics of the compact 2.45 GHz ECR ion source [2].

Extraction voltage	1-10	[kV]
Beam current density	> 10	[mA/cm^2]
Beam aperture	ϕ 2-3	[mm]
Normalized beam emittance	~ 0.6 π	[mm mrad]
ECR zone	ϕ 19×36	[mm^3]
Plasma chamber	ϕ 32×72	[mm^3]
Outer size of main body	ϕ130×132	[mm^3]
2.45GHz microwave power	< 1.3	[kW]

It is possible to inject the sample materials into the ECR zone from the upstream side on the central beam axis. A laser ablation apparatus [1] is connected with the ECR ion source directly at the upstream side. A compact Nd:YAG pulsed laser at 1064 nm wavelength with the pulse width of 8 ns and the maximum energy of 50 mJ is employed to evaporate the sample materials as a means of introducing solid samples into the ECR plasma. At present, the optical simulation for the drift line is performed to estimate the trapping efficiency of the laser produced particles in the ECR plasma.

The laser coupling with the ECR ion source will be used for the element-analysis experiments and the production of multi-charged fullerene beams.

Acknowledgments

The compact 2.45 GHz ECR ion source was installed in overall cooperation with Dr. E. Tojyo (KEK). This work is supported in part by the Grand-in-Aid for Scientific Research (Encouragement of Young Scientists (B) - No.14750039) of the Ministry of Education, Science, Sports and Culture.

References

[1] K. Sasa, UTTAC71 (2003) 11.

[2] E. Tojyo, et al., Genshikaku Kenkyu, Vol.37, No.3 (1993) 45.

1.3 Development of the polarized target system for measurement of $\vec{D}(\vec{d},p)T$ reaction

M.Iio[1], I. Daito[2], Y. Tagishi, N. Horikawa[3], T. Hasegawa[1], T. Iwata[4],
Y. Yamaguchi, T. Shinba, N. Yoshimaru, N. Okumura, Y. Tajima, S. Ishii,
T. Kobayashi[5], T. Inagaki[6], N. Doshita[6], K. Kondo[6]

The nuclear fusion process has been expected to be one of the better methods to be able to overcome the subjects on future insufficient energy sources. ^{3}He + D nuclear fusion reaction is considered because of a less neutron production rate in the reaction process, which minimizes the irradiation damages to the wall of the reactors. However, the neutrons might be generated from the D + D collision process in the high temperature plasma of ^{3}He + D mixture. Then, the use of a polarized nuclear fusion reaction has been considered to be one of the methods to solve this problem[1].

According to the references, the ^{3}He + D nuclear reaction proceeds mainly via the ^{5}Li($3/2^+$) compound nuclear state, and then the reaction cross section in both ^{3}He and D being polarized might be enhanced to be about 1.5 times larger than the one of the unpolarized reaction case. Additionally, the D + D reaction process with both polarized might be much suppressed in the low energy region where the reactions may proceed mainly in S-waves and be forbidden according to the Pauli-principle. Therefore, the D + D fusion reaction rates would be expected to be enhanced or suppressed if deuterons could be polarized in the plasma. This is only the theoretical predictions and is not verified realistically yet by any experiments until now[2, 3, 4].

Thereby, we are now going to measure the possible enhanced spin depend cross sections for the $\vec{D}(\vec{d},p)T$ nuclear fusion reaction at 20 MeV now by using a polarized deuteron beam of Tandem Accelerator Center, University of Tsukuba (UTTAC)[5] and a polarized deuterium target developed mainly at Nagoya University based upon the so-called dynamic nuclear polarization (DNP) method.

As shown in Fig.1, the present polarized deuterium target system consists of a ^{3}He-^{4}He dilution cryostat, a 2.5 T superconducting magnet, a 70 GHz μ-wave irradiation system for DNP method and a NMR system monitoring the target polarization. The CD_2 target is set on the top of μ-wave guide tube and inserted in the mixing chamber (MC) made from glass epoxy so as to be positioned at the center of the superconducting magnet. The MC with 1 mm thick inner space is filled with liquid ^{3}He and ^{4}He mixture and able to cool down to the lowest as 250 mK, which temperature is kept to be less than 300 mK for the 1 nA deuteron beam incidence during the experiment and is consistent with the previously tested and obtained cooling power of 2 mW at 300 mK.

The magnetic field of 2.5 T with the homogeneity of 10^{-4} in the central part of 5 mmϕ is prepared by a superconducting Helmholtz magnet with 5 mm gap, which is enough space for the detection of the

[1]Faculty of Engineering, Miyazaki University, 889-2192 Miyazaki, Japan
[2]Research Center for Nuclear Physics, Osaka University, 567-0047 Osaka, Japan
[3]College of Engineering Chubu University, 487-8501 Kasugai, Japan
[4]Department of Physics, Faculty of Science, Yamagata University, 990-8560 Yamagata, Japan
[5]Department of Physics, Tokyo Institute of Technology, 152-8550 Tokyo, Japan
[6]Department of Physics, School of Science, Nagoya University, 464-8602 Nagoya, Japan

scattered particles by counter telescopes of solid state detectors.

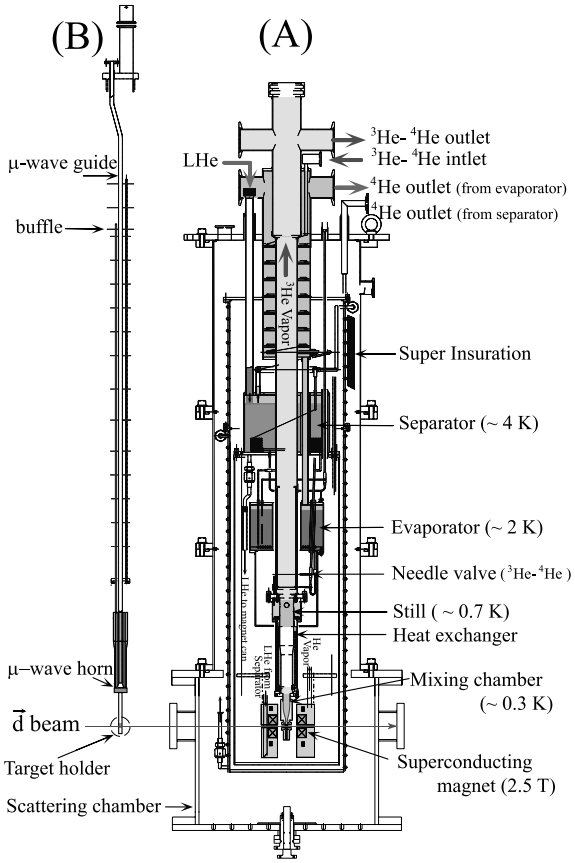

Fig. 1. Side views of polarized target system. (A) Longitudinal sections of ^{3}He-^{4}He dilution cryostat and 2.5 T small superconducting magnet set in the scattering chamber. The deuteron beam comes from the left. (B) Central insert of μ-wave guide, coaxial cable for NMR signal detection and polarized target holder. This part is inserted to the center of the cryostat(A).

The polarized target is warmed up by the beam energy loss, which might affect to decrease the target polarization. The beam energy loss in the target is considered to be larger in the lower energy experiments. We select the thin solid CD_2 foil as a target, in which about $\sim$5 keV/μm of the stopping power is estimated for the 20 MeV incident deuterons. The solid CD_2 foil with 30$\sim$50 μm thickness was developed from high pressurized powders under high temperature. As described before, the DNP method[6] is employed in order to get higher target polarization. Then, it is necessary to make a modification of paramagnetic centers in the target material. The TEMPO (2,2,6,6,-Tetra-Methyl-Piperidine-1-Oxil) was chosen to be doped in the CD_2 by diffusing method, the optimal density of which was 3×10^{19} spins/cm^3 [7].

The 30$\sim$50 μm thick CD_2 foil was installed in the polarized target system and tested several times in almost the same experimental conditions with the actual measurement. The typical operation parameters to polarize the target were as following: temperature of mixing chamber; 0.8 K, magnetic field; 2.5 T, μ-wave frequency; 70.03 GHz and the doped density of unpaired electrons; 2.5×10^{19} spins/cm^3. A typical enhanced NMR signal is shown in Fig. 2, from which the target polarization is estimated to be 10 %.

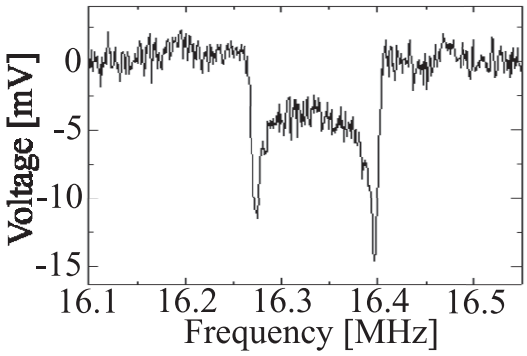

Fig. 2. Typical enhanced NMR signal averaged by 1000 times sweeps, from which the target polarization can be estimated to be 10 %.

Fig. 3 shows the typical energy and particle-identified spectra measured by the counter telescope systems at 20 MeV incident deuteron beam, the upper and lower ones of which show the energy spectrum of deuterons from $D(d,d)D$ scatterings and the protons from $D(d,p)T$ reactions, respectively. The scattered deuterons and the reaction protons can be identified clearly within 350 KeV (FWHM) energy resolutions for deuterons, which might be caused mainly from the target thickness of the CD_2 foil.

The asymmetries of the deuterons yields from $D(d,d)D$ elastic scattering were obtained with an statistical uncertainty less than 0.1 % from Fig. 3. Then, the target polarization was estimated to be about 10 %, which was however not so stable during the test experiment because of the cooling temperature as in higher than 1 K mainly due to the unstable operation of mixing chamber.

References

[1] R.M. Kulsrud et al., Phys. Rev. Lett. 49 (1982) 1248-1251.

[2] H.M. Hofmann and D.Fick, Phys. Rev. Lett. 52 (1984) 2038.

[3] J.S. Zhang, K.F. Liu, and G.W Shuy, Phys. Rev. Lett 57 (1986) 1410; 55 (1985) 1649.

[4] J.S. Zhang et al., Phys. Rev. C 60 (1999) 054614.

[5] Y. Tagishi, J. Sanada, Nucl. Inst. and Meth. 164 (1979) 411.

[6] W.de.Boer, CERN, yellow report 74-11 (1974).

[7] N. Takabayashial, Genshikaku-kenkyu. Vol.43 (1997) 1-43.

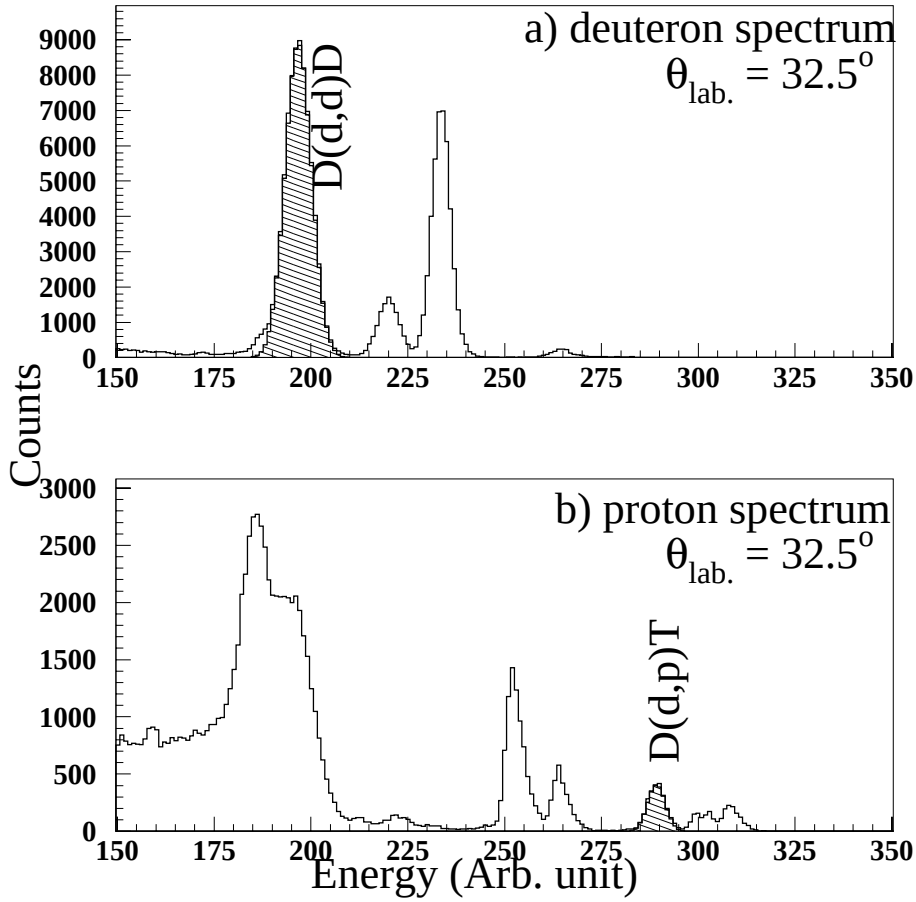

Fig. 3. Typical energy spectra after particle identifications of deuterons (a) and protons (b) obtained by a left-hand side counter telescope at 32.5 degree lab. angle. Hatched peaks in (a) and (b) are identified as $\vec{D}(d,d)D$ elastic scattering and $\vec{D}(d,p)T$ reaction, respectively, from kinematical analyses.

2.1 ^{nat}Sn(d,p) reaction in search for Coulomb stripping of deuteron

M.Iijima, Y.Aoki, N.Okumura, H.Ishiguro, S.Igarashi, T.Ishikawa, M.Yamaguchi and Y.Tagishi

In the 1930s Lawrence and coworkers [1] measured deuteron induced γ ray activity and found that the energy dependence of (d,p) reaction yield was significantly weaker than that of Gamow's theoretical value at around $E_d = 2$ MeV. Oppenheimer and Phillips [2] explained that this weak energy dependence is due to the Coulomb break-up effect arising from small binding energy of deuteron. Later in the 1990s Bencze and Chandler [3] reported this effect was small and negligible.

We thought this problem is not resolved yet and started an experiment to elucidate the Coulomb stripping. In the experiment our aim is to measure energy dependence of the ratio of proton yield from ^{118}Sn(d,p)^{119}Sn(g.s.) reaction to that of elastic deuteron. The target was ^{nat}Sn of 756 μ g/cm^2 thick. Detectors were two E-ΔE counters, each of which was comprised of two identical SSD's with 28 $\times$ 28 mm^2 active areas. Solid angles of the detectors were 39 and 60 msr. We used 7.5 MeV deuteron beam from the Pelletron at UTTAC. Beam current on the target was of the order of 1 nA.

Fig.1. shows the spectrum of deuterons and protons from the d + ^{nat}Sn system observed at 150°. The peaks were assigned from the knowledges of kinematic relationship of (d,p) reaction, isotopic abundance and angular momentum conservation. Fig.2. shows the experimental and the theoretical differential cross sections for ^{118}Sn(d,p)^{119}Sn(g.s.) reaction. Error bars in the figure are from counting statistics. The theoretical values are calculated with DWUCK4 [4] and the optical potential employed is due to Perey and Perey [5].The theoretical differential cross sections thus obtained are multiplied by the factor of 2.0 to fit 130° $\sim$ 150° points. The theoretical and the experimental values do not agree well at 70° and 110° CM angles.

In the next experiment we are planning to use enriched ^{118}Sn target and initial deuteron beam of 5 $\sim$ 7 MeV to measure the energy dependence of the differential cross sections.

References

[1] O.E.Lawrence, E.McMillan and R.L.Thornton, Phys. Rev. **48**,493(1935)

[2] J.R.Oppenheimer and M.Phillips, Phys. Rev. **48**,500(1935)

[3] G.Bencze and C.Chandler, Phys. Rev. **C53**,880(1996)

[4] P.D.Kunz, computer program DWUCK4, private communications

[5] C.M.Perey and F.G.Perey, Phys. Rev. **132**,755(1963)

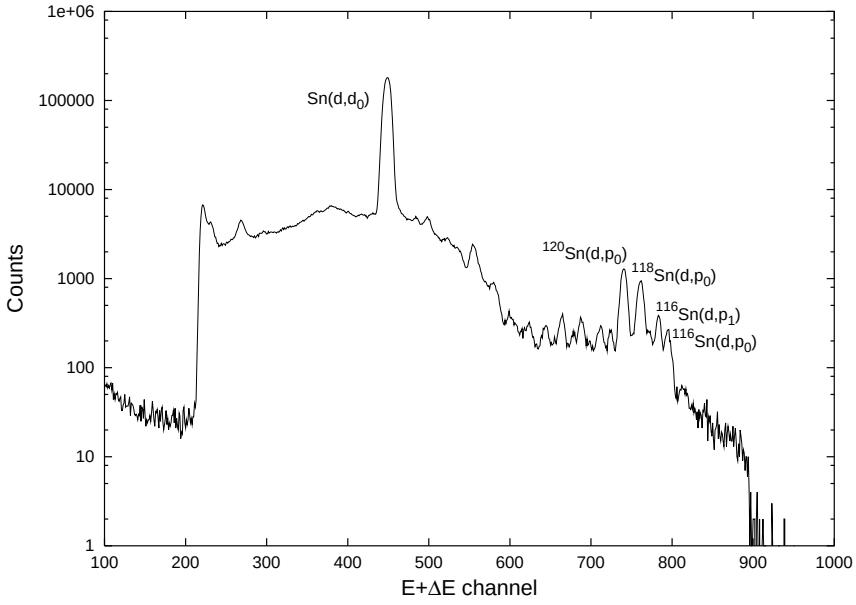

Fig. 1. Energy spectrum of deuterons and protons obtained with 7.5 MeV deuteron beam and ^{nat}Sn target; taken at $\theta_{lab} = 150^{\circ}$.

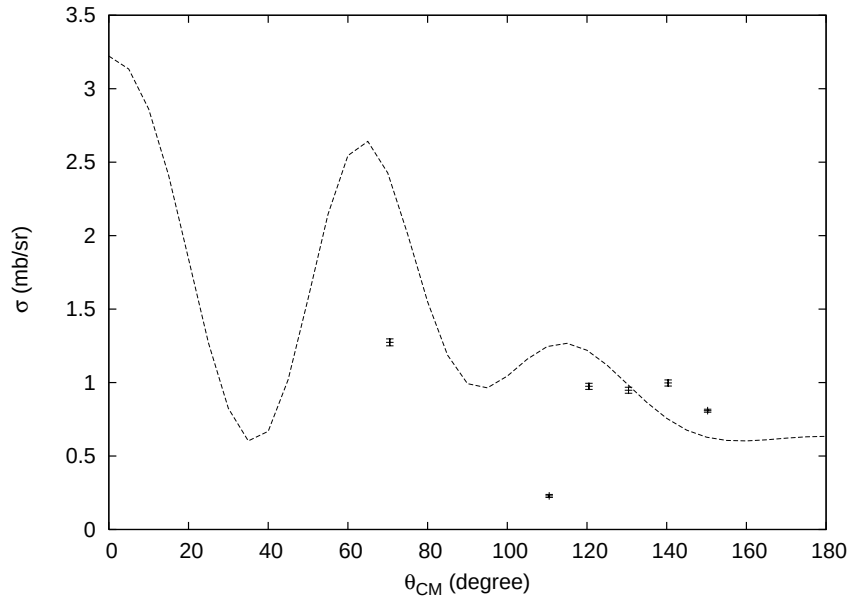

Fig. 2. Comparison of experimental and DWBA calculation for ^{118}Sn(d,p) reaction. See text for more details.

2.2 Differential cross sections and vector analyzing powers in proton elastic scattering from ^{28}Si around neutron threshold energy

N. Okumura, H. Ishiguro, T. Ishikawa, M. Iijima, S. Igarashi and Y. Aoki

Differential cross sections ($d\sigma/d\Omega$) and vector analyzing powers (A_y) of proton elastic scattering from ^{nat}Si were measured around threshold energy of (p,n) reaction. The target was a SiO_2 glass, where the thickness of ^{nat}Si was 0.97 mg/cm^2. Two pairs of E-ΔE counter telescope were used and particle identification was made on CRT two dimensional display.

Figures 1 and 2 show the $d\sigma/d\Omega$ and A_y angular distributions thus obtained, respectively.

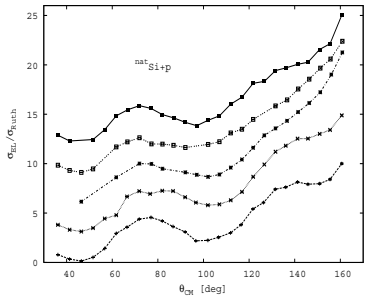

Fig. 1. Energy dependence of differential cross sections. Curves correspond from lower to upper to proton laboratory energy of 15.600, 15.650, 15.750, 15.800 and 15.850 MeV, respectively. Ordinate is the ratio to Rutherford cross sections. Except for the lowest curve, all the curves are shifted by 3 unit.

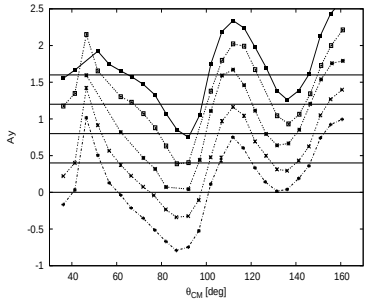

Fig. 2. Energy dependence of A_y. Except for the lowest curve, all the curves are shifted by 0.4 unit. see also the comments of fig 1.

As can be seen from these figures, $d\sigma/d\Omega$ and A_y at backward angles at 15.750 MeV behaves somewhat differently from that of the other energy. It seems that the nuclear attraction is stronger at 15.750 MeV than the rest of the data.

The experiment is intended to extract partial wave delay time in this reaction. As was reported in ref. 1, backward differential cross sections are generally larger than that expected by the global optical potential parameters. Total reaction cross sections calculated by using the usual optical potential parameters fall in the range of 800-900 mb, while that of Okumura is about 600-650 mb.

Combining the experimental data measured thus far, extended optical model analysis is underway to

extract energy dependence of the phase shift.

References

[1] R.De.Leo, G. D’Erasmo, A. Pantaleo, G. Pasquariello, G. Viesti, M. Pignanelli and H. V. Geramb Phys. Rev. C **21**, 646 (1979).

2.3 Measuring energy dependence of proton total reaction cross section around neutron threshold energy

K. Ishiguro, S. Igarashi, M.Iijima, N. Okumura and Y. Aoki

After measuring energy dependence of total reaction cross section σ_R of p+^{nat}Si system 1], we planned to measure that of p+^{12}C system at around $E_p = 19.6$ MeV. Minor improvement of the experimental setup was made, which consist of 1) replacing a rotary slit just upstream of a switching magnet to a one with four independently controllable jaws and 2) moving a beam defining slit of 0.8 mm diameter to about 10 cm upstream of a target. Figs. 1 and 2 show the plan view of the experimental arrangement.

Beam intensity of about 1,000 protons/s on the target was realized as follows, 1) Faint beam was transferred to the beam stop located about 70 cm upstream of the target. 2) The beam stop was removed from the beam line after decreasing the field intensity of the switching magnet slightly. 3) By observing the output of a proportional counter, the filed intensity was gradually recovered carefully. 4) Widths of the slit located upstream of the switching magnet was adjusted to keep the count rate of the proportional counter as desired level. 5) steps 3) and 4) are repeated until maximum beam is transferred to the target. 6) Fine adjustment of the ion optical devices in the beam line was made by referring the count ratio of the proportional counter and an active slit just in front of the proportional counter.

Total reaction cross section is measured by a beam attenuation method, i.e., σ_R is given by the following relation,

$$\sigma_R = \frac{1}{nx}\left\{\frac{I_0 - I}{I_0} - \frac{i_0 - i}{i_0}\right\}.$$

Number density n and thickness x of the target appear in the denominator of the right hand side. I_0 (I) is a number of protons which hit (passed through) the target. I_0 (I) is counted by a pair of proportional counter (plastic scintillator) just in front of (behind) the target. i_0 and i correspond to I_0 and I with no target. Details of the counting system, including active slits and counting logic, are given elsewhere 1].

Typical beam loss in the counting system, defined as $(i_0 - i)/i_0$ was about $1 - 3 \times 10^{-4}$.

Natural carbon foil of 0.1 mm thick was used. Preliminary σ_R at 19.6 MeV was about 700 mb, which is about two times larger than the complied values 2]. The reason of the difference is not pinned down yet.

References

[1] N.Okumura et al., Nucl. Instru and Meth **A 487**, 565(2002).

[2] R.F.Carlson et al., Atomic Data and Nuclear Data Tables. **63**,93(1996).

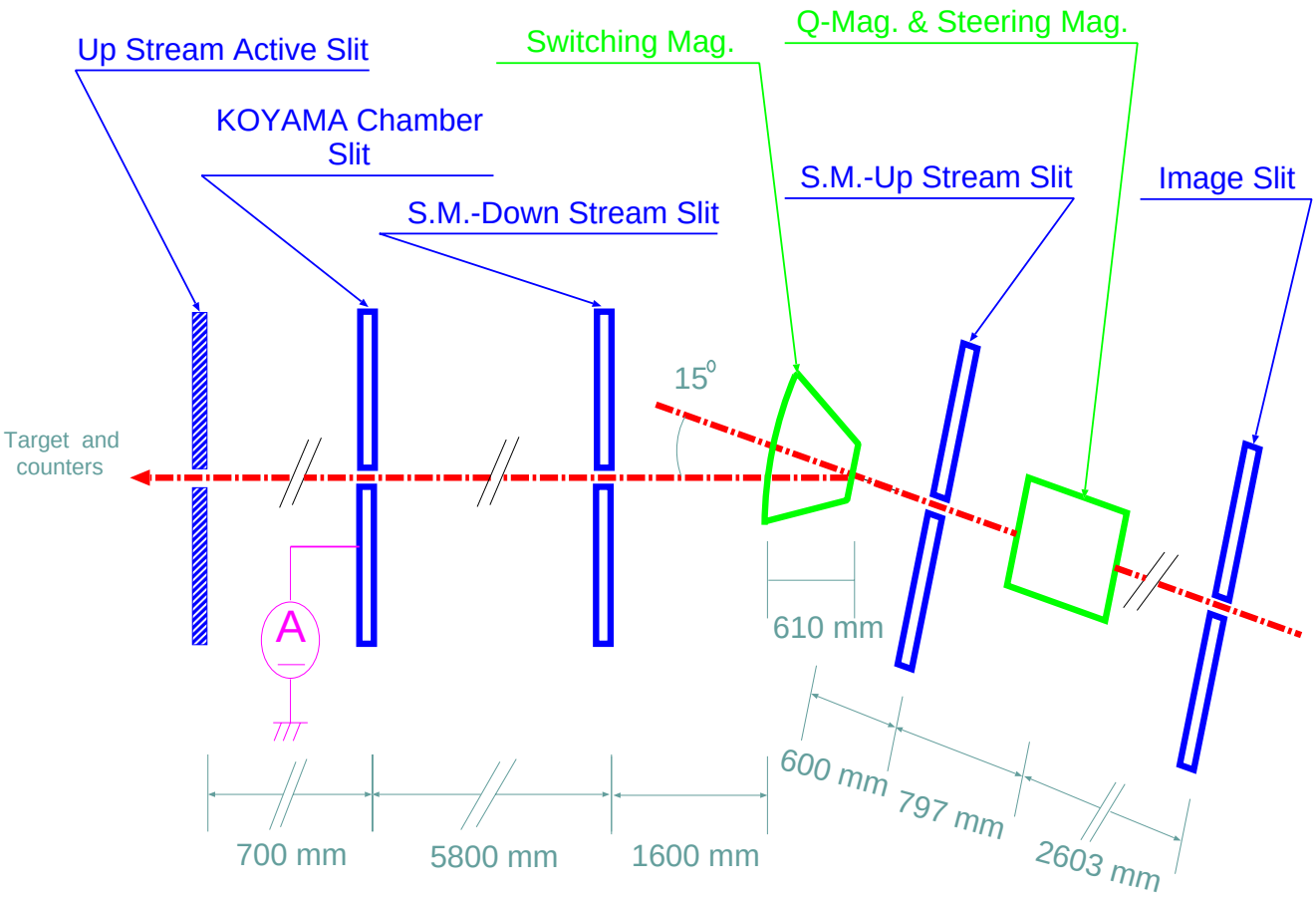

Fig. 1. Plan view of beam transport system

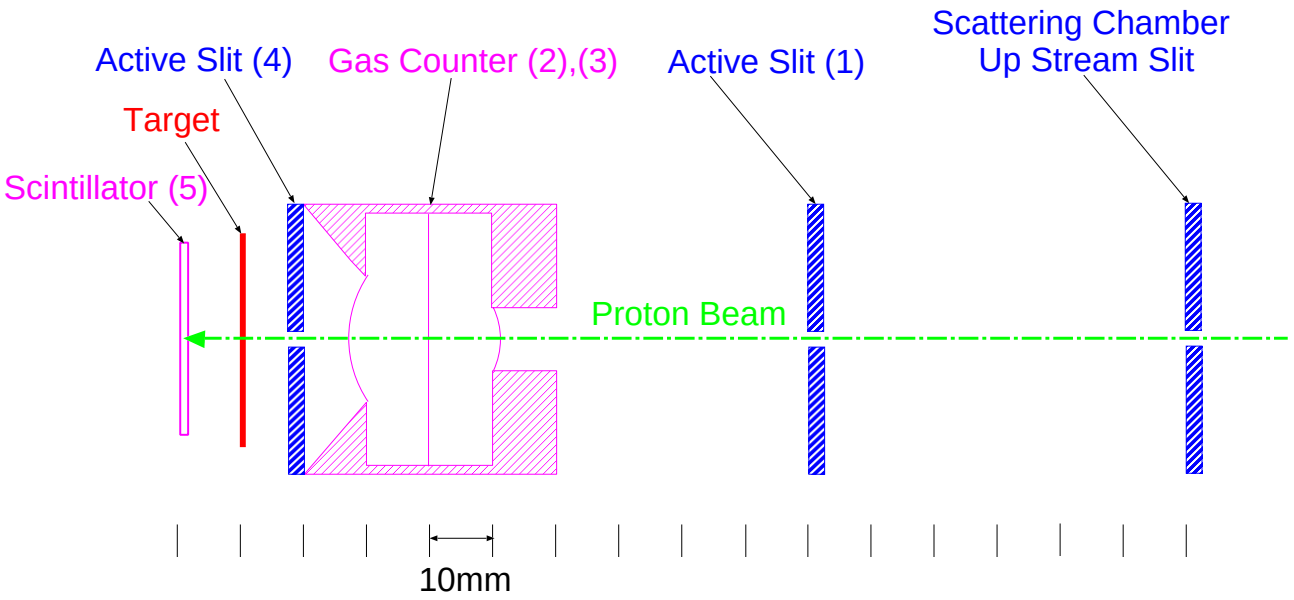

Fig. 2. Counting system of protons

2.4 Analyzing powers for the ^{6}Li(d,p)^{7}Li reaction at incident energy of 90 keV

M.Yamaguchi, N.Yoshimaru and Y.Tagishi

We measured analyzing powers A_y, A_{zz}, A_{xz} and A_{xx-yy} for the reaction $^6\mathrm{Li}(\vec{\mathrm{d}},\mathrm{p})^7\mathrm{Li}$ at the incident energy of 90 keV. At this incident energy the direct reaction component is small enough and the resonant reaction one is dominant. Moreover, at low incident energies the penetrability of the centrifugal barrier limits the orbital angular momenta in the incoming channel to a few, low values. In such case, some of resonance are predominant and the analysis in terms of (l,s,J) reaction matrix elements is especially indicated. In this paper, we treat the experimental data by this analysis. Such measurements and analysis were made for the same reaction at the incident energies of 600 and 960 keV by Glor *et al.*[1]. As they mentioned, their data may include the interference term with the p- and d-wave contribution. Moreover, we think that the direct reaction component can not be negligible in their case. We measured these analyzing powers at a lower energy to simplify the analysis and clear the mechanism of this reaction.

The experiment was performed using the Lamb shift type polarization ion source[2] at UTTAC. The polarization of the deuteron beam was measured by the quench-ratio method[3] just before and after each run. The typical value of the beam intensity was about 100 nA and that of the beam polarization was about 0.7. The uncertainty of the polarization is about 0.02. Fig. 1 shows the placement of the detectors and the target. The target is a layer of lithium carbonate $\mathrm{LiCO_3}$ having the thickness of about 10 μg/cm^2 on an aluminum backing having the thickness of about 15 μm. The enrichment of $^6\mathrm{LiCO_3}$ is 95 %. The beam was introduced to the lithium carbonate layer and was intercepted by the aluminum backing, which plays the role of Faraday cup. A slit with a diameter of 5 mm was placed at the distance of 150 mm upstream from the target. The energy loss in the layer of lithium carbonate is about 8 keV. A meshed sheet of SUS supplied with a voltage of -300 V was placed in front of the target to suppress the secondary emission electron from the target. Because the reaction cross-section is very small, we placed twelve Si-SSD's around the target at every 15° scattering angles from 0° to 165° and measured at twelve angles, simultaneously. Each detector was placed at the distances of 140 mm from the target and has the solid angle of 10 msr. On the each Si-SSD placed in the range of scattering angle from 90° to 165°, a mylar sheet having the thickness of 9 μm was put in order to block elastic deuterons.

Fig. 2 shows the circuit including the detectors. Each Si-SSD is written as a condenser. Each pair of condensers are divided by a resister. The energy of the detected particle is proportional to the sum of two currents I_A and I_B. The active detector is identified by using the value $I_A/(I_A+I_B)$ or $I_B/(I_A+I_B)$. Fig. 4 shows the following block diagram, which mainly consists of NIM modules. The currents I_A and I_B is transformed into the proportionable voltages V_A and V_B by pre-amplifiers, respectively. The spin state of the polarized beam is controlled by *FAst Spin State Interchange Control System* (FASSICS). The information of the spin state is represent by two binary digits, which are included into the main signals V_A and V_B, respectively, as bias voltages. We newly build *a multi-dimensional data taking system* in order to proceed this experiments smoothly. This consists of a PC, two PCI-type ADC-board PCI-3163's (Interface Co.) and some small computer programs. Fig. 3 shows a two dimensional spectrum. The spectrum has

four spectrum-regions and each region corresponds to a spin state of the incident beam.

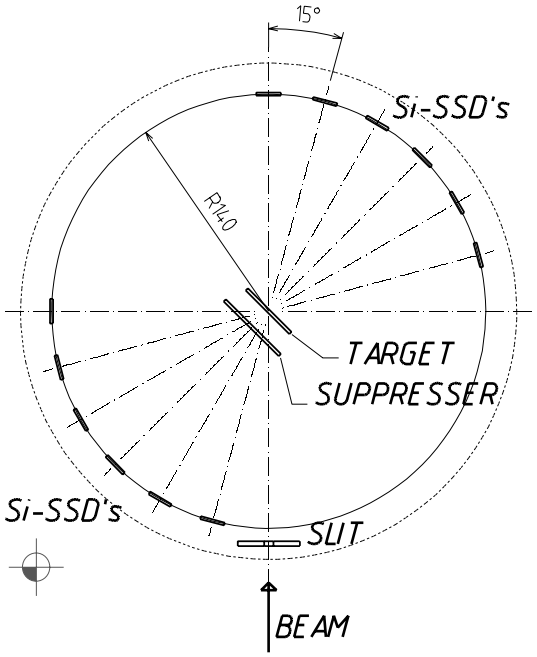

Fig. 1. Scattering chamber and the lay-out of the detectors. Dimension are given in units of mm.

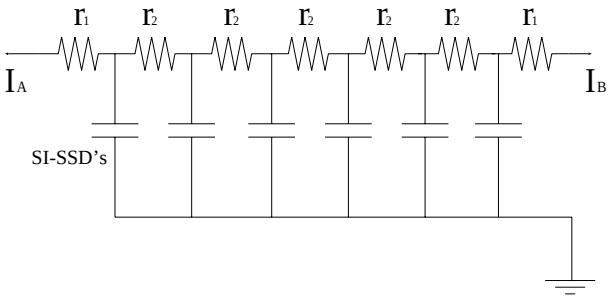

Fig. 2. The circuit including the detectors. Each Si-SSD is written as a condenser. Each pair of condensers are divide by a resister. The energy of the detected particle is proportional to the sum of two currents I_A and I_B. $r_1 = 1$ kΩ, $r_2 = 1.5$ kΩ.

The incident energy dependence of the direct reaction component was estimated by Czerski *et al.*[4]. They calculated the angular distributions of the cross section for this reaction at four energies from 145 to 875 keV by using *distorted wave Born approximation* (DWBA) analysis. They assumed that the resonance component has some isotropic angular distribution and that there is no significant interference effects between the direct and resonance amplitudes. Consequently, their results well explain those experimental data. According to their results, the direct component becomes smaller when the incident energy becomes lower. The component is about 50%, 30% and 13% at the incident energy of 900, 600 and 90 keV, respectively.

In the following sentences we suppose the direct reaction component is negligible. The expansion of the analysing powers in terms of Legendre polynomials

$$\sigma_0^N(\theta)A_j(\theta) = \sum_{L=m} a_j(L)P_{L,m}(\cos\theta), \tag{1}$$

where

$$m = \begin{cases} 0, & \text{for} \quad j = zz \\ 1, & \text{for} \quad j = y \quad \text{and} \quad xz \\ 2, & \text{for} \quad j = xx - yy \end{cases} \tag{2}$$

results in the expansion coefficients $a_j(L)$ given in table 1. Fig. 5 shows the measured analyzing powers and the results of the analysis in terms of (l,s,J) reaction matrix elements. The solid lines and the dashed lines represent the fitting results and the result supposing that the reaction goes only through a resonant process (l,s,J^π,l',s') = $(0,2,2^+,1,2)$, respectively. The dashed lines almost explain the experimental data. This means that the main path of the reaction is $(0,2,2^+,1,2)$. In the case of the coefficients for

vector analyzing power, the coefficient $a_y(1)$ has large non-zero value. This means that the reaction have the interference term of the resonance.[5] In the case of the coefficients for tensor analyzing powers, The coefficients $a_j(1)$ and $a_j(2)$ have nonzero-values. Figs. 6 show the energy dependences of these coefficients $a_j(1)$ and $a_j(2)$, respectively. These data at the incident energy of 600 and 960 keV are those of Glor *et al.*[1] If a resonance excited predominantly by s-wave deuterons, the components of the analyzing power shows a characteristic angular dependence. As long as the resonant element alone is considered, only the coefficient $a_j(2)$ for the tensor analyzing power can be nonzero and are subject to the relation[5]

$$a_{zz}(2) = 2a_{xz}(2) = 2a_{xx-yy}(2). \tag{3}$$

The comparison of the terms of relation 3 is shown in Fig. 6. The error-bars of our data are larger than those of the data at the incident energies of 600 and 900 keV, however, as mentioned above, the contribution of the p- and d-wave and the contribution of the direct reaction are smaller or negligible in the case of our data. Although the coefficients are subject to the relation (3) at the incident energy of 90 keV, as shown in Fig 6, the coefficients $a_{zz}(1)$ and $a_{xz}(1)$ has non-zero values. This means that some other resonant element is concerned.

Table 1. Legendre polynomial coefficients $a_j(L)$ for the analyzing powers.

L	$a_y(L)$	$a_{zz}(L)$	$a_{xz}(L)$	$a_{xx-yy}(L)$
0		0.051 ± 0.021		
1	-0.127 ± 0.021	0.133 ± 0.033	0.113 ± 0.064	
2	-0.013 ± 0.018	0.508 ± 0.041	0.283 ± 0.052	0.317 ± 0.050
3	0.008 ± 0.014	-0.091 ± 0.049	-0.022 ± 0.042	-0.016 ± 0.030
4	-0.002 ± 0.011	0.000 ± 0.053	-0.000 ± 0.032	-0.006 ± 0.020
5	0.002 ± 0.010		-0.001 ± 0.030	0.006 ± 0.013
6				-0.001 ± 0.009

References

[1] M.Glor, H.P.Naegele, G.Morgan, R.Neff, H.Rudin and F.Seiler, Nucl. Phys. A286 (1977) 31-41

[2] Y.Tagishi and J.Sanada, Nucl. Instr. and Meth. 164 (1979) 411.

[3] Gerald.G.Ohlsen, J.L.McKibben, G.P.Lawrence, P.W.Keaton, Jr., and D.D.Armstrong, Phys. Rev. Lett. 27 (1971) 599.

[4] K.Czerski, H.Bucka, P.Heide and T.Makubire, Phys. Rev. Lett. B 307 (1993) 20-24

[5] F.Seiler, Nucl. Phys. A187 (1972) 379

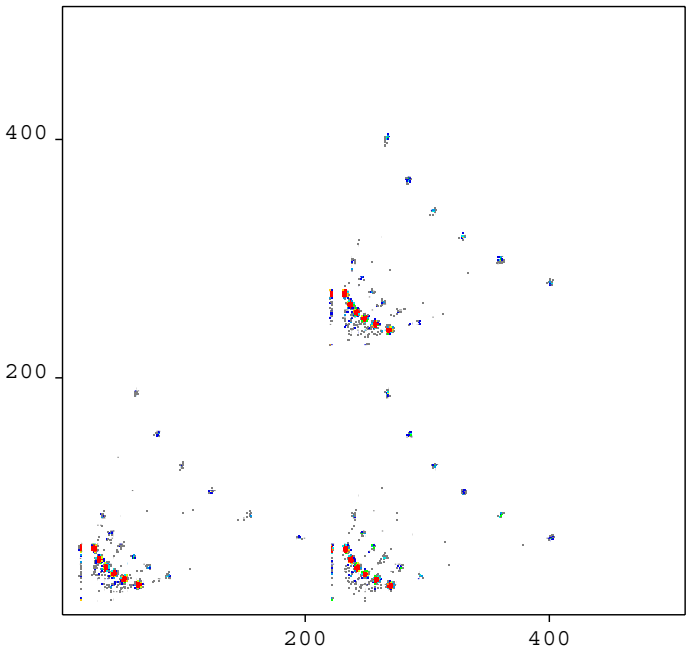

Fig. 3. A two dimensional spectrum.The spectrum has four spectrum-regions and each region corresponds to a spin state of the incident beam.

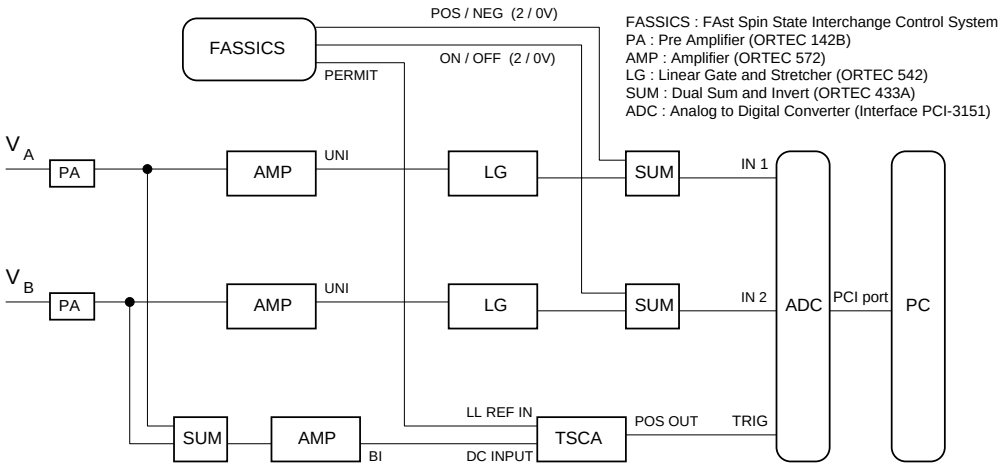

Fig. 4. Block diagram.

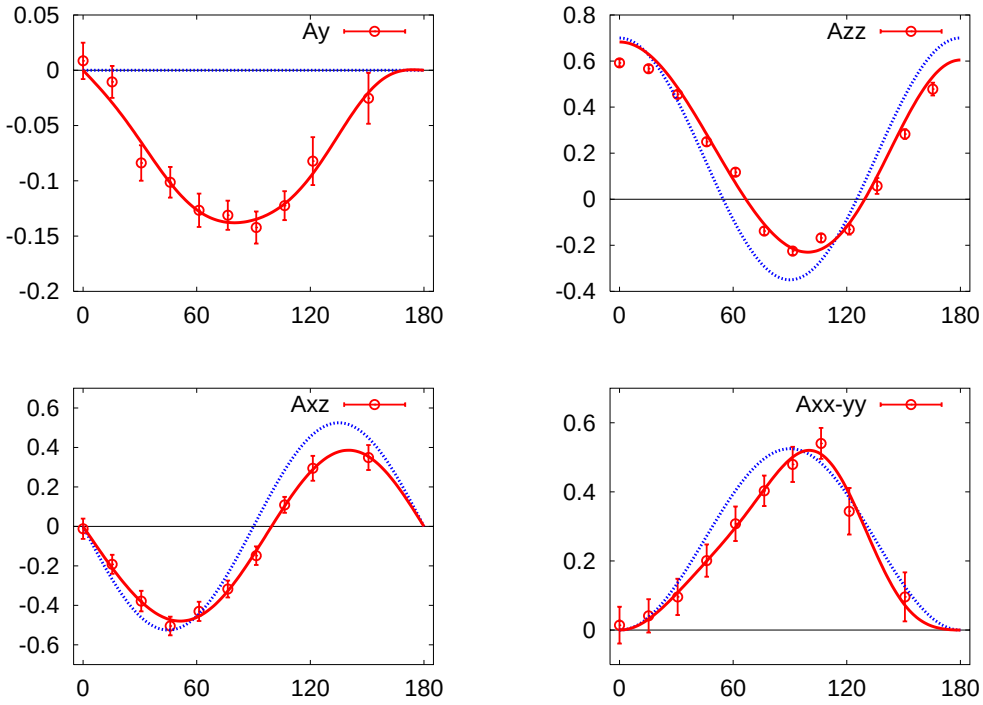

Fig. 5. Results of the measurement of the analyzing powers. Solid lines represents the fitting results. Dashed lines are the result supposing that the reaction goes only through a resonant process $(l, s, J^{\pi}, l', s') = (0, 2, 2^{+}, 1, 2)$.

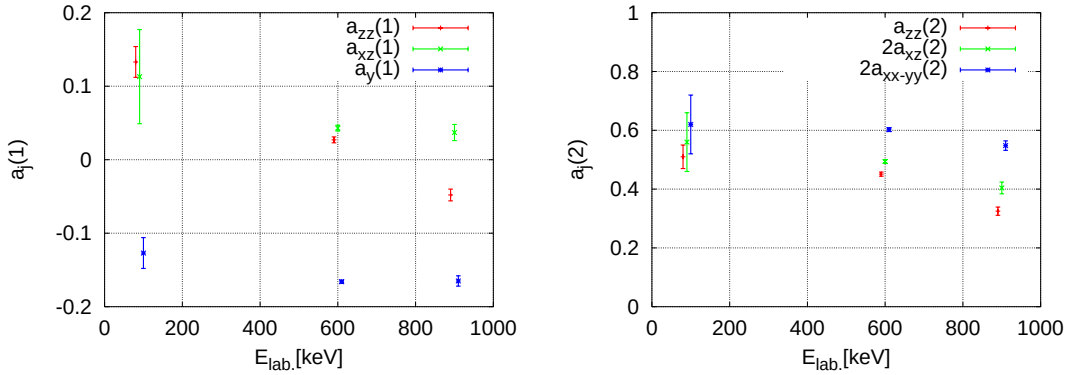

Fig. 6. The left and right figures show the coefficients for the vector and tensor analyzing power, respectively. These data at the incident energy of 600 and 960 keV are those of Glor *et al.*[1]

2.5 Proton-induced reaction for heavy elements

T.Hayakawa[1], T.Shizuma[1], T.Komatsubara, K.Miyakawa

The solar system abundance ratio is a record of stellar nucleosynthesis before the solar system formation. About 99% of elements heavier than the iron group were synthesized by two neutron capture reaction chains, s- and r-processes. However there are rare neutron-deficient stable isotopes that can be produced neither s- nor r-processes. They are called to be "p-nuclei". Their origin has been discussed with possible nuclear reactions and astrophysical sites for a long time. The proposed reactions are the β-decay after the rapid proton capture reactions in novae and X-ray burst in neutron stars[1], photodisintegration reactions in supernova explosions (γ-process)[2], proton-induced reactions by cosmic rays[3], neutrino-induced reactions in supernova explosions[4]. A measurement of a cross section of a (γ,n) reaction using the real photon has been carried out in viewpoint of the γ-process[5]. The calculated results of the γ-process with type II supernova explosions have success to represent partly the solar system abundance of the p-nuclei[2, 5]. The calculated results indicated that the Mo and Ru isotopes may have the different origin from other p-nuclei[2]. Proton capture reactions in low energy region have an important role for the proton capture process[6]. However no cross sections of the proton capture reactions in a region heavier than Sn isotopes except a Ce isotope has been measured.

We here carried out a measurement of a decay γ-ray followed by β-decay of Eu isotopes produced by the p+^{nat}Sm reaction in order to evaluate the proton capture cross section of the Sm isotopes. Natural Sm targets have been irradiated by the proton beam with a energy of 5 MeV. The proton was provided by the tandem accelerator in University of Tsukuba. Fig. 1 shows a nuclear chart and nucleosynthesis flow by the proton-induced reactions in an Sm $\sim$ Gd region. The natural Sm sample consists of seven stable isotopes, ^{144,147,148,149,150,152,154}Sm. Many unstable Eu isotopes were produced by the reaction in the present experiment. Almost Eu isotopes have life-lives in order of 1 $\sim$ 100 days except a few isotopes. We can measure both the γ-ray transition energies and the half-lives. The target was irradiated for about 1 day. After the irradiation, the γ-rays emitted from the activated samples were measured by a HPGe detector. Total efficiency of the HPGe detectors is about 40% relative to $3'' \times 3''$ NaI detector and their energy resolution is about 2.8 keV at 1.3 MeV γ-ray. The efficiency is calibrated with standard sources of ^{152}Eu and ^{133}Ba. The γ-rays from the samples were measured with a lead-shielded low-background environment. We observed the γ-rays from the unstable Eu isotopes. We will measure the changed current of the proton beam with high accuracy and the intensities of the decay γ-rays to evaluate the total cross sections of the proton-induced reactions.

References

[1] H. Schatz et al., Phys. Rev. Lett., **86**, 3471(2001).

[2] M. Rayet et al, Astron. Astrophys. **298**, 517(1995).

[3] J. Audouze, Astron. Astrophys. **8**, 436(1970).

[1]Japan Atomic Energy Research Institute, Advanced Photon Research Center, Kyoto, Kizu, Umebidai 8-1

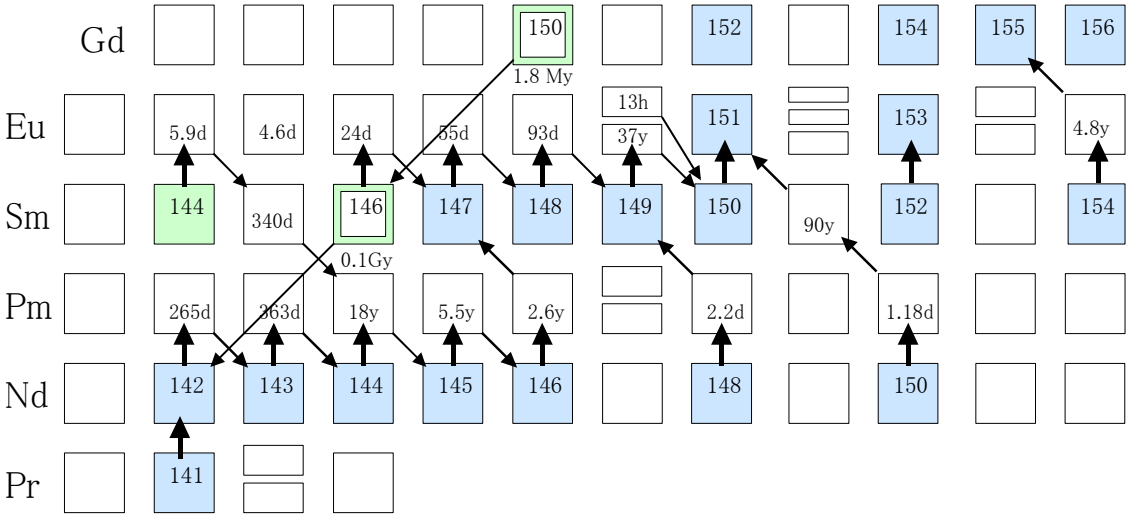

Fig. 1. Nuclear chart and proton-induced reactions around Sm isotopes.

[4] R.D. Hoffman et al., Astrophys. J. **460**, 478(1996).

[5] H. Utsunomiya et al., Phys. Rev. C **67**, 015807 (2003).

[6] Gy. Gryüky et al., Phys. Rev. C **68**, 055803(2003).

3.1 Electron emission induced by fast atom clusters

H. Kudo, T. Suzuki, M. Nagata, T. Shimada, K. Shima, K. Sasa, S. Ishii, Y. Saitoh[1], S. Yamamoto[1], K. Narumi[1], H. Naramoto[1], and T. Kaneko[2]

An accelerated cluster ion induces correlated atomic impacts when it is incident on a solid target. This causes radiation effects different from those induced by impact of a single ion. Actually, fast cluster ions in the MeV/atom velocity range give rise to nonlinear radiation effects on solid targets with respect to the number of atoms in the cluster *n*. These radiation effects by fast atom clusters have been summarized in recent reviews [1, 2].

The aim of the UTTAC–JAERI(TIARA) collaboration for study of cluster beam interactions with surfaces is to investigate the cluster effects by energy analysis of the cluster-induced electrons at low energies. The collaborating work based on the three accelerators at UTTAC and TIARA would provide knowledge about the electronic processes in the cluster impact on solid surfaces. Such a basic approach will also be of fundamental importance for future material processing by fast-cluster impact.

In this fiscal year, the experimental data have been obtained mainly at TIARA, using a new 180° spectroscopy system developed at UTTAC using the cluster beams from the UTTAC Tandetron. The beams of 0.50 MeV/atom, i.e., 41.7 keV/u, C_n^+ ($n = 1$, 4, 8) were obtained from the 3 MV tandem accelerator at JAERI-Takasaki. They were incident on the samples of highly-oriented pyrolytic graphite (HOPG) with a cleaved (0001) surface, and chemically cleaned Si. The surface of the Si sample was cut $\sim$3° off from the (100) surface so that the ions suffer no channeling effect under incidence in the normal direction of the surface. The secondary electrons were measured at 180° with respect to the beam direction, using a 45° parallel-plate electrostatic spectrometer of the double-deflection type, as illustrated in Fig. 1. The 180° measurement is advantageous for the purpose of avoiding errors associated with misalignment of the spectrometer direction. Once the spectrometer is accurately placed at 180°, its entrance axis always

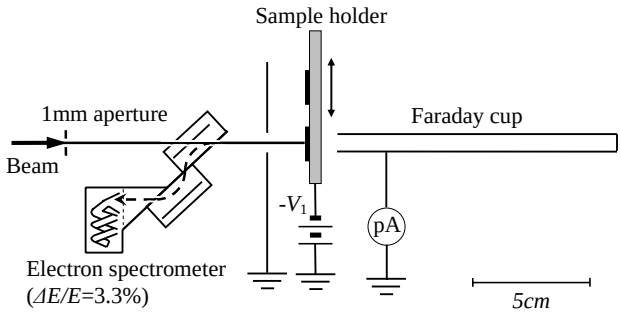

Figure 1: Schematic diagram illustrating the measurements of cluster-induced electrons. Note that $V_1 =$ 60 V throughout the experiments.

passes through the irradiated spot on the surface of the sample. This is not necessarily anticipated at

[1]JAERI, Takasaki
[2]Okayama University of Science

other detection angles. In some cases, the misalignment is caused by different beam-transport conditions for different cluster beams, which effectively changes the counting efficiency, and therefore, disturbs the measurements of *n*–dependence of the electron spectra.

The solid targets were negatively biased i.e., $V_1 = 60$ V, to obtain high transmission of the electrons in the spectrometer, especially at energies lower than 50 eV. In this case, the origin of the energy spectra is shifted to the higher energy side by $\sim eV_1$, where e is the electronic charge. It follows that the energy spectrum of the electrons emitted from the target is separated effectively from the background signals due to the stray electrons at $\sim$0 energy, as seen in Fig. 2. In this case, the real origin of the energy axis is assigned to be 52 eV which is the threshold energy for appearance of the electron signals of interest. Furthermore, to enhance the counting efficiency, +200 V was applied to the entrance of the electron multiplier for pre-acceleration of the electrons. In the present measurements, the relative energy resolution of the spectrometer is given by $\Delta E/(E + eV_1) = 3\%$, for example, $\Delta E = 2.1$ eV at $E = 10$ eV.

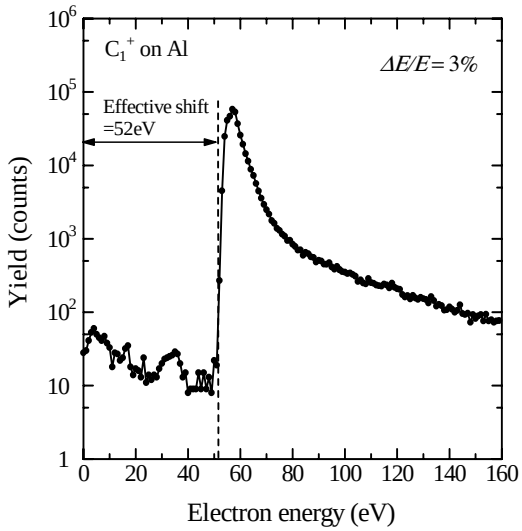

Figure 2: Energy spectra of electrons emitted from Al bombarded by 0.50 MeV C_1^+ for 60 V acceleration ($V_1 = 60$ V). The real zero energy is assigned to be 52 eV, the threshold energy for counting the signals of interest. The relative energy resolution of the spectrometer is $\sim$3%.

The cluster beam current was adjusted in the range 3–10 pA, depending on the ion species, and stabilized typically within $\pm$4%, Also, it was often monitored by the Faraday cup, shown in Fig. 1, which can be used with moving the sample holder out of the beam path. Since the beam current of the clusters was unable to correspond directly with the measured target current, the plate voltage of the spectrometer was applied stepwise typically per 1 sec. This allows to obtain the electron spectra normalized to the same number of the incident atoms, as are necessary for the present study.

The beam dose required for accumulating the spectrum was in the range 5×10^9 to 2×10^{10} projectiles/cm^2. The experiments were carried out at room temperature under a pressure of $\sim 6 \times 10^{-6}$ Pa. Under the present vacuum conditions, possible existence of contaminant atoms on the surfaces is anticipated. This should slightly change the transmission of outgoing electrons across the surface, but should not affect the *n* dependence of the electron energy spectra, which is of primary interest in the present studies.

The energy spectra of electrons presented here are raw data, i.e., the yield in the vertical axis is

the number of electron signals counted. Accordingly, the spectra include no correction for the energy acceptance of the spectrometer, nor for the energy dependence of the efficiency of the electron multiplier. This is of minor importance because the measured electron yields for different experimental conditions are compared always at the same electron energy. Furthermore, the energy axes of the spectra represent the real values, as noted earlier.

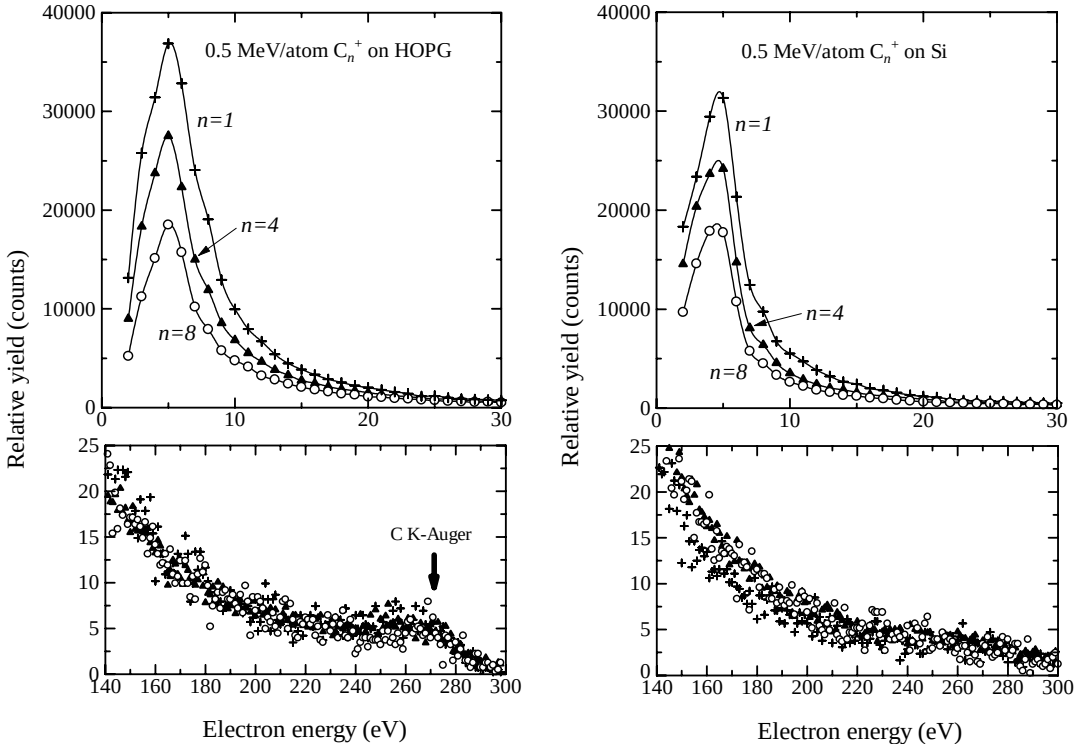

Figure 3: Energy spectra of electrons emitted from HOPG (left) and Si (right) bombarded by 0.50 MeV/atom C_n^+ ($n = 1, 4, 8$). The yields are shown for the same number of the incident C atoms.

Figure 3 shows the energy spectra of electrons emitted from HOPG and Si, bombarded by 0.50 MeV/atom C_n^+ ($n = 1, 4, 8$). The yields for the two targets are shown for the same number of the incident C atoms for comparison of the spectra per projectile atom. The carbon K-shell Auger peak originating from the HOPG target can be seen at the expected energy of 260–270 eV, demonstrating the validity of the rescaled energy axis. Also, the absence of the carbon K-shell Auger peak for Si target assures reasonable surface conditions. It should be noted that in this case the K-shell ionization cross section is 8×10^{-18} cm^2, and is mainly due to the molecular-orbital promotion of a carbon K–shell electron [3], in contrast to the production process of low-energy electrons of interest resulting mainly from the direct ionization of outer-shell and velence electrons in the target. Also, the Auger electrons emitted from the projectile carbon atoms in the direction of 180° should have an energy of ∼130 eV, however, the correspoding peak was hardly recongnized in the spectra.

In Fig. 3, the yield at low energies is appreciably reduced with increasing n. Details of such nonlinear character can be seen in Fig. 4, where the ratios of the spectra for C_n^+ ($n = 4, 8$) to C_1^+ are shown. The ratios take minimum values near the zero energy, for example, ∼0.50 for large clusters, increase with increasing the electron energy, and become ∼1 at 100–200 eV. The estimated minimum values are indicated by the

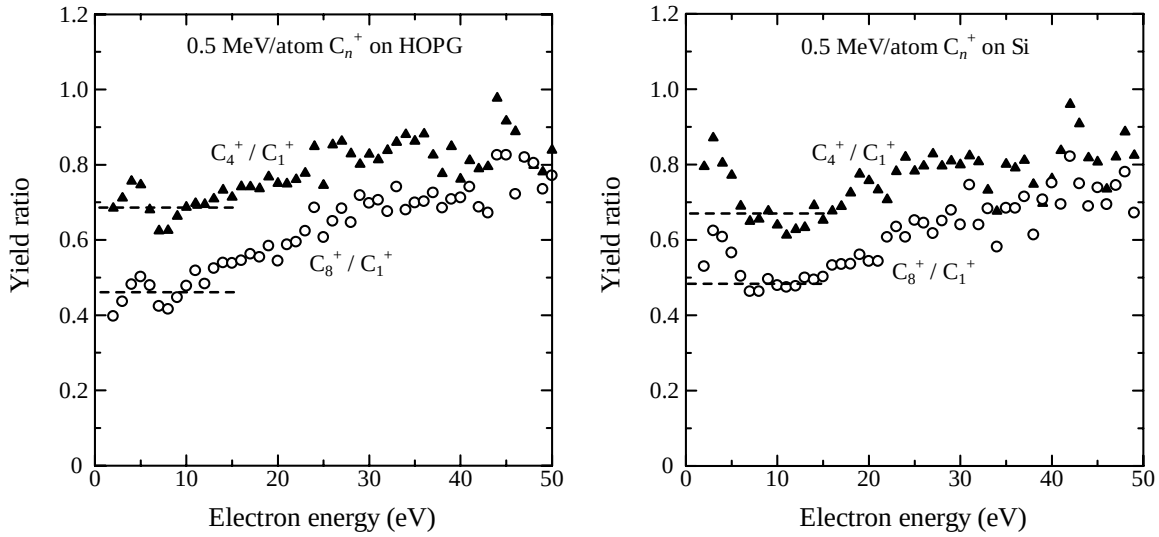

Figure 4: Ratios of spectra for HOPG (left) and Si (right) bombarded by 0.50 MeV/atom C_n^+ ($n = 1, 4, 8$). The dashed lines show the estimated minimum values of the ratios.

dashed lines in Fig. 4. Such pronounced reduction of the electron yield can be hardly explained in terms of the stopping power, for which the predicted cluster effect is as small as less than 5% [7].

The yield ratios at zero electron energy R_0, shown by dashed lines in Fig. 4 are effectively independent of the target material. This indicates that R_0 stems from the charge states of the ions near the surface since the charge states of ions in solid is only weakly dependent on the target material [5]. The electrons of near-zero energy should be produced by distant collisions with the clusters so that we may apply the concept of the effective point charge to the electron emission [6]. Actually, the interaction of an n–atom cluster with the target electrons is written in terms of the effective charge Q_n. From the charge dependence of the Rutherford cross section, R_0 is given by

$$R_0 = (Q_n/Q_1)^2 \,, \tag{1}$$

where Q_1 for the C_1^+ impact can be assumed to be 1.0 near the surface since the input charge state should remain almost unchanged near the surface, considering that the equilibrium charge of 0.5 MeV/atom C is 1.4, [5, 7] which is close to the input charge state. From the experimental data, the values of Q determined are $Q_4 = 0.83 \pm 0.03$ and $Q_8 = 0.69 \pm 0.03$. Such reduction of the effective charges is consistent roughly with the observations of charge states of transmitted cluster fractions by Brunelle et al. This also implies reduction of charging effect when atom clusters are incident on insulators. Further studies with heavier atom clusters are now under way.

References

[1] D. Jacquet, Y. Le Beyec, Nucl. Instrum. Methods B 193 (2002) 227.

[2] E. Parilis, Nucl. Instrum. Methods B 193 (2002) 240.

[3] R. C. Der, R. J. Fortner, T. M. Kavanagh, J. M. Khan, Phys. Rev. A 4 (1971) 556.

[4] A. Brunelle, S. Della-Negra, J. Depauw, D. Jaquet, Y. Le Beyec, and M. Pautrat, Phys. Rev. A 59 (1999) 4456.

[5] K. Shima, T. Mikumo, H. Tawara, At. Data Nucl. Data Tables 34 (1986) 357.

[6] N. Stolterfoht, R. D. DuBois, R. D. Rivarola, *Electron Emission in Heavy Ion–Atom Collisions* (Springer, Berlin, Heidelberg, 1997).

[7] T. Kaneko, Phys. Rev. A66 (2002) 052901.

3.2 Resonant coherent excitation of C^{5+} observed with loss electron yield from a Si crystal

M. Nagata, T. Suzuki, T. Shimada, and H. Kudo

An axially channeled ion moving along an equally spaced row of atoms experiences a periodic electronic field of frequency v/d, where v is the ion velocity and d is the atomic spacing. A fast ion can then be excited resonantly when the frequency matches the excitation energy of the bound electron I, i.e., $I = Nhv/d$, where h is the Planck constant and $N = 1, 2, 3, \cdots$ [1]. This phenomenon, resonant coherent excitation (RCE), occurs also for planar channeling. Details of RCE have been described, for example, in a review by Krause and Datz [2]. RCE has so far been observed mainly by charge-state analysis of channeled ions passed through thin, self-supported crystals. RCE also affects the photon emission, or the convoy electron emission. It should be noted that RCE has been observed under surface channeling conditions.

Recently, Kudo and coworkers have demonstrated that the loss electron yield resulting from the ionized electrons from the projectile C ions reflects the charge states of the ions moving along a channeling or random (nonchanneling) direction [3]. Under RCE conditions, the loss electron yield might be increased by the easier ionization from an excited state than from the ground state. This is actually a two-step loss process in contrast to the normal (non-resonant) loss process [4]. From a viewpoint of ion-induced electron spectroscopy, it is of essential interest to investigate the influence of RCE on the production of loss electron yield from a bulk target since, unless it is negligibly small, it must be taken into account when crystalline targets are used.

The 3.02 and 3.30 MeV/u C^{5+} and C^{6+} beams obtained from the tandem accelerator at the University of Tsukuba were incident on a chemically cleaned Si(100) surface at room temperature under a pressure of $\sim 1\times10^{-6}$ Pa. For Si$\langle 100\rangle$, the RCE condition for $N = 2$ (2nd harmonics) from the ground state to the first excited state ($n = 1$ to 2) of C^{5+} is satisfied at 3.02 MeV/u, while the 3.30 MeV/u energy was chosen to obtain the off-RCE data for comparison with the 3.02 MeV/u data. The beams were collimated by double slits to an angular divergence of less than 0.015° which is much less than the channeling critical angle of Si$\langle 100\rangle$, $\sim 0.16^\circ$. The $\langle 100\rangle$ perpendicular to the Si surface was chosen to observe RCE. The energy spectra of the ion-induced electrons were measured at 180° with respect to the beam direction over a solid angle of $\sim 2\times10^{-3}$ sr, adopting the experimental setup similar to the previous studies. The relative energy resolution ($\Delta E/E$) of the spectrometer was $\sim$5%, which is sufficient for the present analysis of the loss electron yield. Further technical details of the 180° electron spectroscopy combined with the ion channeling technique have been discussed in a recent literature [5].

Figure 1 shows energy spectra of the emitted electrons induced by 3.02 and 3.30 MeV/u C^{5+} and C^{6+} under Si$\langle 100\rangle$, (110), and random incidence conditions. The spectra are normalized to the same number of the incident ions. The peaks near 1.5 keV is due to Si K-shell Auger electrons. Note that the yield in the vertical axis is the number of electron signals counted. Accordingly, the spectra include no correction of the energy acceptance of the spectrometer, nor for the energy dependence of the counting efficiency of the electron multiplier. However, this does not affect the discussion below since the electron spectra are

compared essentially at the same electron energy. In Fig. 1, E_{L} indicates the loss-peak energy which is the

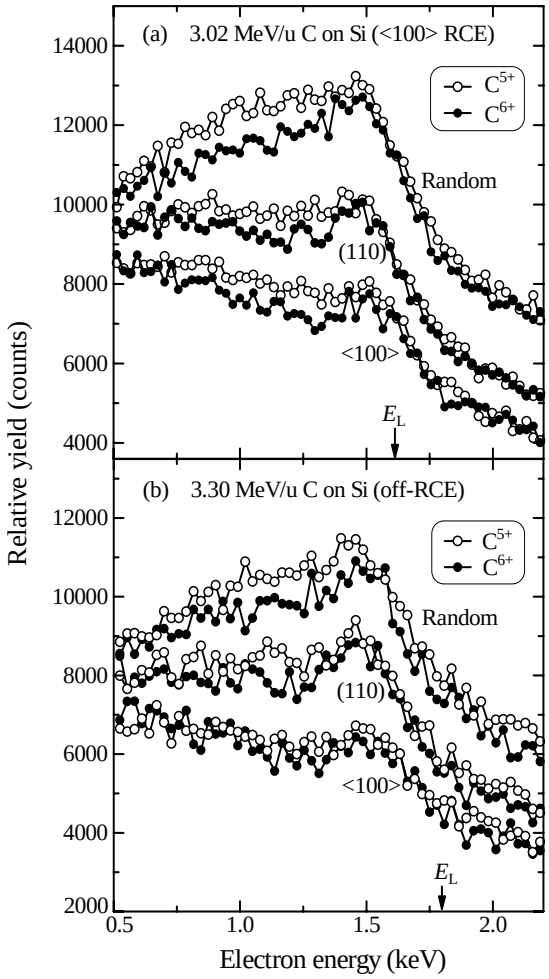

Figure 1: Energy spectra of electrons emitted from Si bombarded by (a) 3.02 and (b) 3.30 MeV/u C^{5+} and C^{6+} under $\langle 100 \rangle$ axial, (110) planar, and random incidence conditions. The yields are normalized to the same number of the incident ions. E_{L} indicates the loss-peak energy. The relative energy resolution of the spectrometer is $\sim$5%.

kinetic energy of the electron moving at the same velocity as of the ion. The ionized electrons from the ion contribute to the backward electron yield at energies lower than $\sim E_{\mathrm{L}}$. We see that the electron yields for $\langle 100 \rangle$ and (110) are reduced, compared with the random case, because of the effective shadowing of the crystal atoms. It is recognizable that for (110) and random cases the C^{5+} yield below E_{L} is higher than for C^{6+}, irrespective of the two ion energies. This is due to the collision-induced loss electrons anticipated not for C^{6+}, but for C^{5+}. For $\langle 100 \rangle$, in contrast, the loss electron yield can be seen for the 3.02 MeV/u ions, while it is hardly seen for the 3.30 MeV/u ions. For a better statistics, we have integrated the electron yield in the range 0.8–1.4 keV, $Y_{\mathrm{int}}(C^{5,6+})$, and the normalized loss yield L has been defined by

$$L = [Y_{\mathrm{int}}(C^{5+}) - Y_{\mathrm{int}}(C^{6+})]/Y_{\mathrm{int}}(C^{6+}) \,. \tag{1}$$

L is the ratio of the loss yield to the binary-encounter yield. The latter is the dominant energy-transfer process to the target electrons, as is typical for keV electron yield induced by MeV/u ions. Therefore, L is

Table 1: Values of the normalized loss yield L obtained for the incident energy of 3.02 MeV/u ($\langle 100 \rangle$ RCE) and 3.30 MeV/u (off-RCE).

Orientation	3.02 MeV/u	3.30 MeV/u
$\langle 100 \rangle$ axis	0.075 ± 0.003	0.033 ± 0.002
(110) plane	0.055 ± 0.003	0.064 ± 0.003
random	0.069 ± 0.003	0.071 ± 0.003

a measure of production efficiency for the loss electron yield. The values of L obtained are summarized in Table 1, where the estimated uncertainty in the values arises mainly from the instability of the incident beam.

In Table 1, we see that under the RCE condition (3.02 MeV/u) the values of L for $\langle 100 \rangle$ is enhanced by a factor of 2.3 relative to the off-RCE case, while neither (110) nor random incidence causes such enhancement. It is notable that the off-RCE data is consistent with the previous study of loss electrons also under off-RCE conditions [3], which concludes that the main charge states of 2.5 and 3.5 MeV/u C ions are C^{5+} and C^{6+} for Si$\langle 100 \rangle$ and random cases, respectively. Indeed, the value of 0.075 for $\langle 100 \rangle$ is roughly the same as 0.069 and 0.071 for the random cases, indicating that most of the C^{5+} are ionized by RCE.

Since E_{L} is the most probable energy of the produced loss electrons, the typical loss yield for $\langle 100 \rangle$ at an energy of ε =1.25 keV in Fig. 1(a) comes roughly from the depth of $(E_{\mathrm{L}} - \varepsilon)/S_{\mathrm{e}}$, where S_{e} is the electron stopping power. Using the value of $S_{\mathrm{e}} = 1.6$ eV, the depth, i.e., the escape length is 244 Å. This implies that the observed RCE results typically from $244/5.43 \simeq 45$ glancing collisions with Si atoms.

According to the observation of C^{5+} RCE by charge state analysis by the Oak Ridge group, the Stark split of the RCE spectra is relatively small, which is consistent with the present observation of the RCE enhancement at the calculated resonance energy without considering the Stark effect.

The loss electron analysis is sensitive to the charge states of ions *in* a crystal. This is contrast to the case of charge state analysis of ions passing through a thin crystal, or reflected from a crystal surface. Accordingly, the present study would provide a unique observation technique of RCE. Further experiments are planned to obtain more refined data.

References

[1] V. V. Okorokov, Zh. Ehksp. Theor. Fiz. Pis. Red. 2 (1965) 175 [JETF Lett. 2 (1965) 111].

[2] H. F. Krause, S. Datz, Adv. At. Mol. Opt. Phys. 37 (1996) 139.

[3] H. Kudo, K. Takeda, T. Suguri, W. Iwazaki, C. Sakurai, I. Arano, S. Numazawa, S. Seki, Nucl. Instrum. and Methods B207 (2003) 283.

[4] N. Stolterfoht, R. D. DuBois, R. D. Rivarola, *Electron Emission in Heavy Ion–Atom Collisions* (Springer, Berlin, Heidelberg, 1997), Sect. 6.4.

[5] H. Kudo, *Ion-Induced Electron Emission from Crystalline Solids* (Springer Tracts in Modern Physics Vol. 175, Springer, Berlin, Heidelberg, 2002), Chap. 5.

3.3 Solid target thickness where energetic ions attain charge equilibrium

K.Shima and K.Sasa

The knowledge on the charge equilibrium thickness, T_{eq}, where projectile charge states attain equilibrium in matter is important in the fields of accelerator or nuclear instrument technology. Actually, in the tandem accelerator energy region, there has been little way to estimate the T_{eq} values [1, 2]. It is because reported data of charge distributions of ions observed at charge nonequilibrium region are limited, in addition to the fact that the estimation of T_{eq} from collision process, is not an easy task. In order to serve as a milestone for the systematic understanding of T_{eq} in matter, T_{eq} values have been investigated for the collision of various ions of Z_1 (projectile atomic number) on carbon foils because existing data of T_{eq} are mostly reported for carbon foils. Our method of approaching the object is on one hand to measure the T_{eq} values by ourselves, and on the other hand to accumulate the data by others.

Our data taking for ionic charge distributions in charge nonequilibrium to equilibrium region has been done by using a magnetic spectrograph, ESP-90. Ion species is Z_1=1 to 53, and ion energy region is mostly from 0.5 to a few MeV/u.

A conventional way of expressing the T_{eq} values has been to choose the coordinates of T_{eq} versus ionic energy in units of MeV/u. [1, 2]. At present, as a result of accumulating much more data, the adoption of these coordinates proved to be of no use since data points scatter at random. In Fig.1, the T_{eq} values of compiled data at present are plotted as a function of Z_1 for the group of ions with 1, 2 and 6 MeV/u. Some T_{eq} values in the figure are interpolated ones because they were not taken at exact values of 1, 2 or 6 MeV/u. Fig.1 clearly indicates some structure between T_{eq} versus Z_1, which is caused by the variation of ionic shell where the electron of the most probable charge state in equilibrium is included.

Fig.1. Charge equilibrium thickness T_{eq} of various ions with atomic number Z_1 passing through a carbon foil at projectile energies of 1, 2 and 6 MeV/u.

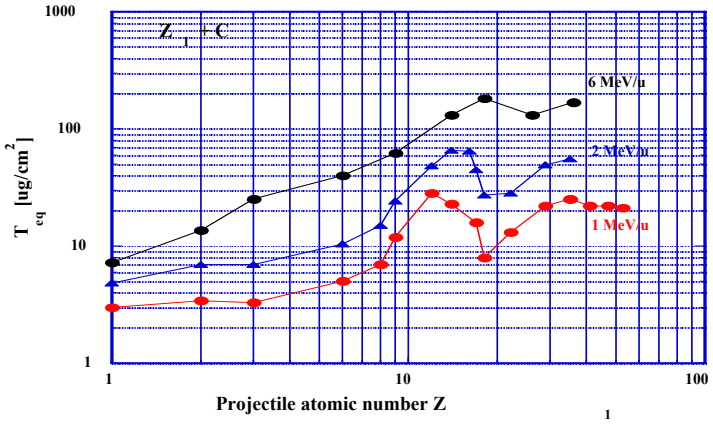

References

[1] V.P.Zaikov, E.A.Kral'kina, N.F.Vorobjev, I.S.Dmitriev, V.S.Nikolaev and Ya.A.Teplova, Nucl. Instrum. Methods B5 (1984) 10.

[2] E.Baron, IEEE Trans. NS-26 (1979) 2411.

3.4 Structural characterization of thin films by RBS technique

H. Yanagihara, A. Hatanaka, J. Sawahata, E. Kita, K. Akimoto and H. Kudo

Rutherford backscattering spectrometry (RBS) technique is a powerful and common method to characterize thin film structures. An RBS gives the chemical composition as a function of depth in the sample and either density or thickness of the analyzed thin film. The other advantages of this technique are: (a) non-distractive , (b) high-sensitive, (c) rapid. Combining with other complementary structure-analysis techniques such as AFM, STM, SEM, XRD, XAFS and so on, we used RBS experiment to determine precise structures of various thin films; metal , oxide, nitride, silicide, and nano-particle films prepared by different kinds of growth techniques.

An experimental setups are as follows. 1.5 MeV accelerated ^{4}He ions with a tandem accelerator placed at the TAC were chosen for regular RBS experiments. The geometry of incident angle(α), exit angle(β) and scattering angle(θ) are 30, 0 and 150 degrees, respectively. We used a solid-state detector placed at 70 *mm* from the sample surface. The RBS data were analyzed by a commercial simulation program (SIMNRA ver. 5.0[1]) which works on Windows based PCs. This program has functions of both the RBS data fitting and the spectrum simulation with graphical interfaces.

As an example, an RBS data of a chromium dioxide(CrO_2) thin film is shown in Figure 1. The epitaxial CrO_2 films were grown on rutile(TiO_2) substrates by using a chemical vapor deposition(CVD) method[2]. The thickness of CrO_2 is estimated as $\sim$ 400 Åby assuming the bulk density. Our CVD system is not equipped a growth-rate control system such as thickness monitor or flow-meter. Therefore some characterization technique of the film thickness without destruction is necessary. For this purpose, the RBS is very suitable and essential for our experiments. Other than CrO_2, we examined the similar analysis for Fe_3O_4, TiN, and Ga*R*N (*R* denotes rare-earth metals) thin films to find their thickness and/or chemical composition.

In summary, employing the RBS equipment placed at the TAC, we have performed the structural characterization of various thin films. An useful RBS program made the spectrum analysis easier and quantitatively helped to determine either the film thickness and/or the composition.

References

[1] http://www.rzg.mpg.de/∼mam .

[2] S. Ishibashi, T. Namikawa, and M. Satou, Jpn. J. Apl. Phys., **17**, 249(1978).

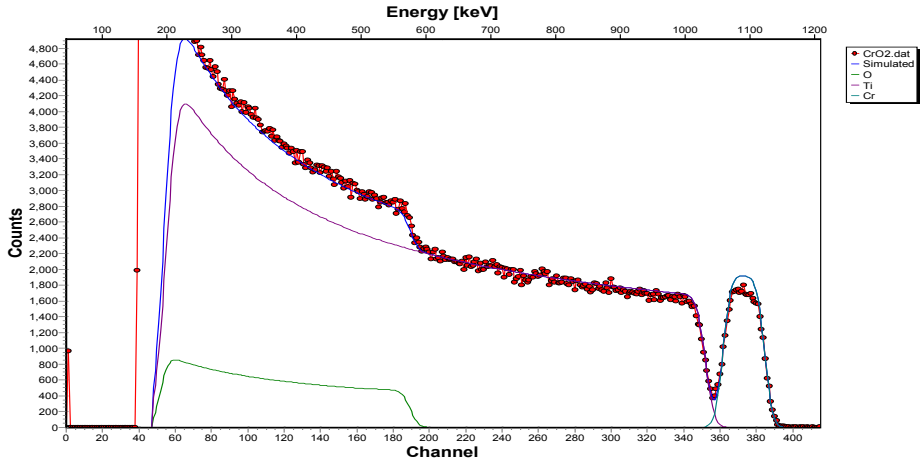

Fig. 1. RBS spectrum of CrO_2(001) epitaxial film. The simulation curves for total profile as well as each element are displayed.

3.5 Molecular beam epitaxy of Si-based ternary alloy semiconductor $Ba_{1-x}Sr_xSi_2$ on Si(111) substrates

T.Suemasu, Y.Inomata, Y.Izawa and F.Hasegawa

Semiconducting iron disilicide (β-$FeSi_2$) consists of abundant Si and Fe, and it has been attracting considerable attention as a promising material for Si-based optoelectronic devices. From the viewpoint of device application, it is desirable to exploit the so-called band-gap-engineering technique in β-$FeSi_2$ as in III-V and II-VI compound semiconductors; that is, the modification of the band gap of β-$FeSi_2$ by replacing some Si atoms with isoelectric C or Ge atoms [1-3]. However, it has been difficult to incorporate notable amounts of C or Ge in β-$FeSi_2$. It is therefore necessary to find another semiconducting silicide which is more suitable for forming ternary or quaternary alloys. We think that orthorhombic barium disilicide ($BaSi_2$) is a good candidate for such a material.

The band gap of $BaSi_2$ is reported to be 1.1−1.3 eV [4-6]. Very recently, we have realized the epitaxial growth of $BaSi_2$ films on Si(111) substrates by MBE (MBE; codeposition of Ba and Si on a heated substrate) using an RDE-grown $BaSi_2$ layer as a template [7]. As far as $BaSi_2$-based ternary alloys are concerned, there has been only one report on the growth of $BaSrSi_2$ polycrystalline bulk to our knowledge [8]. The formation of $Ba_{1-x}Sr_xSi_2$ bulk with Sr molar fractions up to approximately 70 % was reported. The paper was however focused on the phase transition of $Ba_{1-x}Sr_xSi_2$ under high pressure and high temperature conditions, and thus, there were no descriptions on its electrical and optical properties. To use $Ba_{1-x}Sr_xSi_2$ in real devices, it is necessary to form high-quality $Ba_{1-x}Sr_xSi_2$ films and investigate its electrical and optical properties. However, there has been no report on the formation of $Ba_{1-x}Sr_xSi_2$ films.

The purpose of this study is to form $Ba_{1-x}Sr_xSi_2$ epitaxial films on Si(111) by MBE and investigate whether a certain kind of lattice contract takes place by adding Sr into $BaSi_2$.

MBE growth was performed as follows: First, the deposition rate of Ba was fixed at 1.0 nm/min; then a 20-nm-thick $BaSi_2$ epitaxial film was grown at 500ºC for 20 min by RDE, and this film was used as a template to control the crystal orientation of $BaSi_2$ over layers. Next, Ba, Sr and Si were coevaporated on the $BaSi_2$ template at 600ºC. The deposition rates of Ba and Si were fixed at 1.0 and 0.66 nm/min, respectively, so that the stoichiometry of $BaSi_2$ was satisfied. The deposition rate of Sr was changed from 0 to 2.5 nm/min, and we prepared six samples with different deposited Sr-to-Ba ratios (Sr/Ba ratios) varying from 0 to 2.5. The temperatures of Ba and Sr K-cells were set at 440ºC and 275−365ºC, respectively. The total thickness including the template layer was about 80 nm. We chose 600ºC as the growth temperature because this temperature was found to be optimum for the epitaxial growth of $BaSi_2$ by MBE [7]. The Sr molar fraction x against Ba in $Ba_{1-x}Sr_xSi_2$ was evaluated by Rutherford backscattering spectroscopy (RBS) measurements using C^+ ions accelerated at 1.82 MeV. The crystal quality of $Ba_{1-x}Sr_xSi_2$ and its *a*-axis lattice constant were characterized by X-ray diffraction (XRD) measurements using Cu *K* α radiation, and the surface morphology was observed by atomic force microscopy (AFM).

Figure 1 shows the RBS random spectra for samples grown with different deposited Sr/Ba ratios. As seen in Fig.1, with increasing deposited Sr/Ba ratio, the peak corresponding to Sr became clear. These

spectra obtained experimentally were reproduced by simulation and the Sr molar fraction to Ba in $Ba_{1-x}Sr_xSi_2$ was then derived. There was no difference in Si content between the grown $Ba_{1-x}Sr_xSi_2$ layers with different x values. The root mean square (RMS) roughness of the grown films was evaluated by AFM. They are summarized in Table 1. Surface roughness gradually decreased with increasing x. The reason for this improvement is not clear at present, but is thought as follows: The amount of deposited Ba was insufficient because of Ba desorption from the Si(111) surface due to its large vapor pressure even when Ba and Si were supplied in stoichiometric proportion. With increasing x, the Sr deposition rate increased and then the deposited Ba plus Sr ratio to Si could lead to a real stoichiometric condition. Next, the Sr molar fraction x of $Ba_{1-x}Sr_xSi_2$ was discussed. It was found that x increased up to 0.49 with increasing deposited Sr/Ba ratio to 2.5. The x value of 0.49 is smaller than that obtained in $Ba_{1-x}Sr_xSi_2$ bulk, where about 70 % of Ba was replaced by Sr.[21] It might be possible to incorporate more Sr atoms in the Ba site of $BaSi_2$ by further increasing the deposited Sr/Ba ratio and by lowering the growth temperature.

To investigate the crystalline quality of the grown layers, θ-2θ XRD measurements were performed, as shown in Fig. 2. The diffraction peaks of Si(222), $BaSi_2$(400) and $BaSi_2$(600) planes are clearly observed for the samples with $x<0.08$. On the other hand, the diffraction peaks of $BaSi_2$(400) and $BaSi_2$(600) planes split into two peaks for the samples with $x\geq0.27$. Since the peak positions of the low-angle diffraction peaks seen around 41° and 65° for these samples did not change at all with x, as indicated by dotted lines, it can be said that they correspond to $BaSi_2$(400) and $BaSi_2$(600) planes, respectively. All the samples contained a 20-nm-thick [100]-oriented $BaSi_2$ template layer, and thus, the origin of these low-angle diffraction peaks is thought to be the $BaSi_2$ template layer. In contrast, the high-angle diffraction peaks shifted clearly to a high-angle-region with increasing x, indicating that the spacing between [100]-oriented planes of the film decreases. The atomic radius of Sr is smaller than that of Ba, and thus, when some Ba atoms in the $BaSi_2$ lattice structure are replaced by Sr atoms, this kind of lattice contract will take place. The high-angle diffraction peaks are therefore thought to be those of $Ba_{1-x}Sr_xSi_2$(400) and $Ba_{1-x}Sr_xSi_2$(600) planes. On the basis of these results and the fact that there is no indication of the formation of any secondary phases from the XRD measurements, it can be said that [100]-oriented $Ba_{1-x}Sr_xSi_2$ films were grown epitaxially on Si(111). For the sample with x=0.08, the diffraction peaks of $BaSi_2$ and $Ba_{1-x}Sr_xSi_2$ overlap due to the small incorporation of Sr, and thus, a small peak shift rather than two-peak splitting was observed.

Next, to investigate the lattice contract caused by Sr incorporation into $BaSi_2$, the *a*-axis lattice constant of $Ba_{1-x}Sr_xSi_2$ was evaluated from the XRD peak positions of $BaSi_2$(400) and $BaSi_2$(600) diffraction patterns. Figure 3 shows the Sr molar fraction versus *a*-axis lattice constant plots for $Ba_{1-x}Sr_xSi_2$ obtained in this study (+) and in a previous study (●) [8]. To reduce the measurement error, *a*-axis lattice constants determined from $Ba_{1-x}Sr_xSi_2$(400) and $Ba_{1-x}Sr_xSi_2$(600) peak positions were first plotted against cotθ after canceling zero offset error by adjusting the measured peak position of Si with the theoretical one. The peak positions were determined by Gaussian fitting. The lattice constant *a* of $Ba_{1-x}Sr_xSi_2$ was then extrapolated from the intersection of the straight line passing through the above two points at $\cot\theta=0$. As shown in Fig. 3, the lattice constant *a* of $Ba_{1-x}Sr_xSi_2$ linearly decreased with increasing x as $a=0.891-0.041x$ (nm), showing that it follows Vegard's law. The *a*-axis lattice constant of the sample with

x=0.49 is about 2 % smaller than that of strain-free $BaSi_2$ bulk. However, the gradient of the straight line obtained in this study is slightly different from that reported in the $Ba_{1-x}Sr_xSi_2$ bulk. This is probably because the measured *a*-axis lattice constants of thin films derived from XRD peak positions were scattered due to the residual strain in the $Ba_{1-x}Sr_xSi_2$ layers, and thus, this strain effect should be corrected using elastic constants of $BaSi_2$. Unfortunately, those values have not been well studied in $BaSi_2$. As far as the electrical properties of $Ba_{1-x}Sr_xSi_2$ films are concerned, it was found from Hall measurements that $Ba_{1-x}Sr_xSi_2$ is a semiconductor. The details of these measurements will be reported elsewhere.

In summary, we have grown [100]-oriented $Ba_{1-x}Sr_xSi_2$ epitaxial films on Si(111) substrates by MBE at 600 °C using a [100]-oriented $BaSi_2$ epitaxial template formed by RDE. RBS measurements revealed that the Sr molar fraction x of the grown $Ba_{1-x}Sr_xSi_2$ films was found to be vary from 0 to 0.49 by changing the deposited Sr/Ba ratio from 0 to 2.5. The *a*-axis lattice constant of $Ba_{1-x}Sr_xSi_2$ showed a linear dependence of the Sr molar fraction x, and the lattice constant *a* of $Ba_{0.51}Sr_{0.49}Si_2$ was about 2 % smaller than that of strain-free $BaSi_2$ bulk.

We would like to thank Professor H. Kudo and Assistant Professor H. Yanagihara for their help with RBS measurements performed at the Tandem Accelerator Center of the University of Tsukuba.

References

[1] H. Chen, P. Han, X. D. Huang, L. Q. Hu, Y. Shi and Y. D. Zheng: Appl. Phys. Lett. **69** (1996) 1912.

[2] A. Zenkevich, P. I. Gaiduk, H. P. Gunnlaugsson and G. Weyer: Appl. Phys. Lett. **81** (2002) 904.

[3] X. Li, D. Nie and C.Dong: Nucl. Instrum. Methods Phys. Res. B **194** (2002) 47.

[4] J.Evers and A. Weiss: Mater. Res. Bull. **9** (1974) 549.

[5] T. Nakamura, T. Suemasu, K. Takakura and F. Hasegawa: Appl. Phys. Lett. **81** (2002) 1032.

[6] K. Ojima, M. Yoshimura and K. Ueda: Jpn. J. Appl. Phys. **41** (2002) 4965.

[7] Y. Inomata, T. Nakamura, T. Suemasu and F. Hasegawa: Jpn. J. Appl. Phys. **43** (2004) L 478.

[8] J. Evers: J. Solid State Chem. **32** (1980) 77.

Table I. Deposited Sr/Ba ratio, Sr molar fraction x evaluated by RBS and thickness of a $Ba_{1-x}Sr_xSi_2$ film.

Sample	Deposited Sr/Ba ratio	Sr molar fraction x	RMS (nm)
A	0	0	7.6
B	0.1	0.03	4.0
C	0.5	0.08	5.8
D	0.8	0.27	2.5
E	1.3	0.41	3.2
F	2.5	0.49	2.2

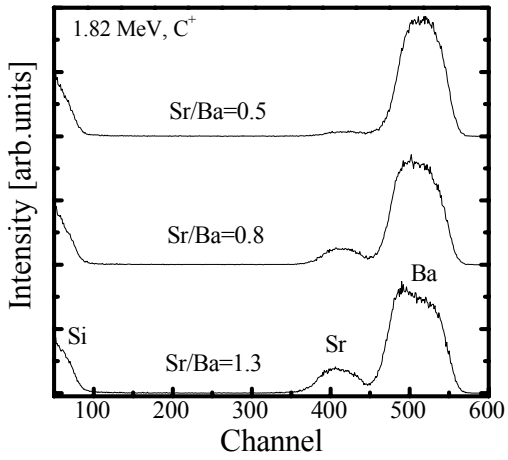

Fig.1 RBS random spectra of $Ba_{1-x}Sr_xSi_2$ films grown with different deposited Sr/Ba ratios.

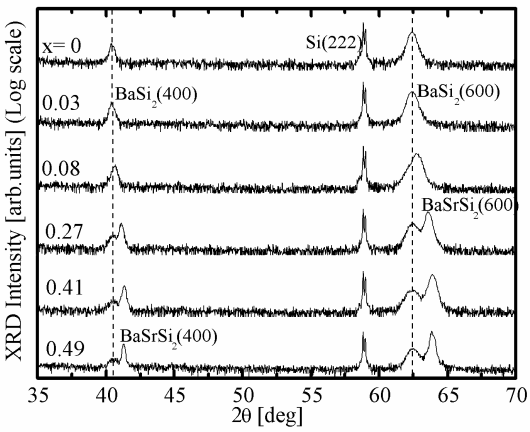

Fig.2 θ-2θ XRD patterns of $Ba_{1-x}Sr_xSi_2$ films with different x values.

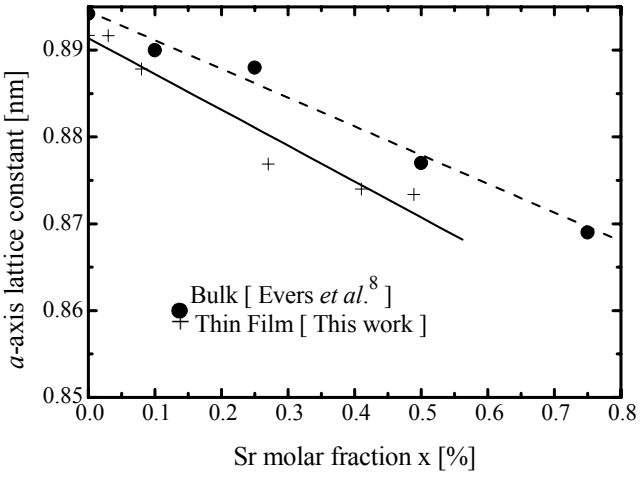

Fig.3 Sr molar fraction x dependence of *a*-axis lattice constants of $Ba_{1-x}Sr_xSi_2$ thin films (+) grown in this work and bulk (●) grown by Evers (ref. 8). The bars show the range of measurement error.

3.6 Swift heavy ions for nano-fabrication of titanium dioxide

Koichi Awazu[*1], Yoshihiro Nagasawa,[2] Yoshimichi Ohki,[2] and Tetsuro Komatsubara

Abstract

We have developed a nano-micro structure fabrication method in rutile TiO_2 single crystal by use of swift heavy-ion irradiation. The area where ions heavier than Cl ion accelerated with MeV-order high energy were irradiated was well etched by hydrofluoric acid, by comparison etching was not observed in the pristine TiO_2 single crystal. Noticed that the irradiated area could be etched to a depth at which the electronic stopping power of the ion decayed to a value of 6.2keV/nm. We also found that the value of the electronic stopping power was increased, eventually decreased against depth in TiO_2 single crystal with, e.g. 84.5MeV Ca ion. Using such a beam, inside of TiO_2 single crystal was selectively etched with 20% hydrofluoric acid, while the top surface of TiO_2 single crystal subjected to irradiation was not etched. Roughness of the new surface created in the single crystal was within 7nm with the atomic forth microscopy measurement.

Introduction

Photonic crystal structures for controlling electromagnetic waves in two or three dimensions are applied for outstanding optical devices. One of the most conventional methods to obtain micro-structures must be the reactive ion etching (RIE), however, roughness and ripple pattern on the side wall of micro-structures, RIE-lag, and etch stop have been frequently observed. Besides the "main stream" of photonic crystals' researches based on semiconductors, photonic crystals based on TiO_2 have also been reported.[1] Micro fabrication techniques for the material have not been established indeed, but this material offers many advantages. Reflection loss due to connection between photonic crystals and silica based optical waveguides would be reduced because refractive index values of (2.4($\perp$c axis) and 2.7(//)) in a rutile TiO_2 single crystal are close to in silica, rather than in semiconductors. Furthermore, optical transmission loss of TiO_2 is ten times lower than in silicon in the vicinity of 1.5μm as mentioned previously.[2] Since TiO_2 remains high list as a material for the photonic crystals, it is desired to fabricate a nano-structure with nano-order flatness and precision. In the present work, we examined to fabricate the micro-structure with nano-flatness on both bottoms and side walls in rutile single crystal by swift heavy ions. Furthermore, as an unexpected phenomenon, three dimensional structure was created in rutile TiO_2 single crystal.

---

1 CAN-FOR, National Institute of Advanced Industrial Science and Technology, Tsukuba Central 4 305-8562 Japan

2 Department of Electrical Engineering and Bioscience, Waseda University, 3-4-1 Ohkubo, Shinjuku-ku, Tokyo 169-8555, Japan

*Corresponding author: k.awazu@aist.go.jp, voice +81-29-861-5650, fax +81-29-861-2919

Experimental

The samples used in the present experiment are (100) rutile TiO_2 single crystal (purity > 99.99%, density: 4.25g/cm^3) synthesized by the Verneuil flame-fusion method. Ion irradiation using the 12MV tandem accelerator at Tandem Accelerator Center, University of Tsukuba (UTTAC) was performed at room temperature. [3] Structural change induced by ion irradiation was investigated by X-ray diffraction (XRD) measurements with a Rigaku FR-MDG apparatus. A scanning electron microscope (SEM, Hitachi S-2500CX) and a high-resolution electron microscope (HREM, Hitachi H-9000NAR) were also employed to observe sample surfaces. Chemical etching was performed with 20% hydrofluoric acid, hereafter 20% HF, at room temperature.

Results

Figure 1 shows an SEM image of rutile TiO_2 (100) single crystal surface subjected to 45MeV Cu ion irradiation at an accumulated dose of 3.0×10^{13}cm^{-2} through a 1μm thick gold stencil mask with a 1μm diameter dot pattern. The irradiated rutile (100) single crystal was then immersed in 20% HF for 40min. Cylindrical patters with diameter of 1μm with 2μm height were created on TiO_2 single crystal. Figure 2 shows XRD spectra of the (100) rutile irradiated by the 84.5-MeV Cu ions. The spectrum (i) is for the non-irradiated sample. Two peaks at 39.2^o and 84.3^o, to be assigned to the (200) and (400) planes, are seen. Curves (ii), (iii), (iv), and (v) are the spectra obtained in the samples after irradiation to respective doses of 1.0×10^{12}, 3.0×10^{12}, 7.0×10^{12}, and 5.0×10^{13} cm^{-2}. The two XRD peaks become smaller by the ion irradiation. Besides them, new peaks appear at 38.3^o and 82.5^o in spectrum (iii). They become smaller and move to smaller angles as the irradiation dose increases, and finally disappear in spectrum (v).

Figure 3 shows electronic stopping power S_e calculated by SRIM 98 code as a function of the depth from the sample surface. Values of etched depth were plotted with closed circles in Fig. 3. The point at $S_e = 0$ was close to the depth where the ion was stopped. At first glance, the etched depth was shallower than the depth at $S_e =0$. For instance, the etched depth and the depth at $S_e =0$ for 120MeV I ion were 6.5μm and 11μm, respectively. The first order feature was that the values of S_e at the etched depth presented with closed circles were always located around the solid line of 6.2keV/nm irrespective of incident ions or acceleration energies. In other words, a threshold electronic stopping power of 6.2keV/nm was apparently necessary to commence etching.

Furthermore, another surprising result was obtained. Namely, after the crystals were irradiated by the Ca ions with various energies to a dose of 8.0×10^{13} cm^{-2}, they were cut perpendicularly to the surface and immersed in the HF solution. Figures 4 show typical cross-sectional SEM images taken for the sample irradiated by the 72.3, 82.0 and 84.5MeV ions. The position of the irradiated top surface and the direction of ions are indicated by arrows. The top surface was not etched, while an inside gap or a vacant hollow was created by etching about 4 μm below the surface in case of 72.3MeV Ca ions. Similar inside gaps were always observed if the energy of Ca ions was higher than 72.3 MeV, and the position of the gap

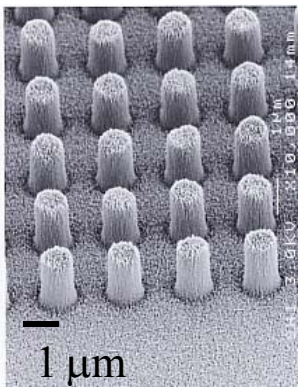

Figure 1. A SEM image of the TiO_2 surface etched by 20 % hydrofluoric acid for 40min. The sample was irradiated with 45MeV Cu ion irradiation to a dose of 3.0×10^{13} cm^{-2} through a 1μm thick gold mask with pattern of 1μm diameter.

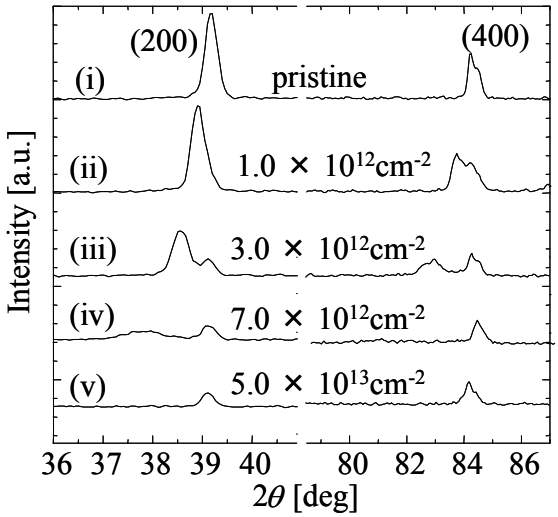

Figure 2. XRD spectra of the as-received sample (i), after the 84.5MeV Cu ion irradiation to a dose of $1.0\times10^{12}cm^{-2}$ (ii), $3.0\times10^{12}cm^{-2}$ (iii), $7.0\times10^{12}cm^{-2}$ (iv), and $5.0\times10^{13}cm^{-2}$ (v). The peaks at $39.2^{o}$and 84.3^{o} are due to the (200) and (400) planes of the rutile phase, respectively.

became deeper as the energy increased. For example, when the energy was 82.0 MeV, the gap was seen at depths between 5.4 to 7.7 μm from the top surface. Figure 3 shows the electronic stopping power S_e as a function of the depth. The dotted portion of each curve shows the depths where the hollow etching was made. Similar hollow etching was also observed in rutile irradiated by Cl ions with energies of 77.0 MeV and higher to a dose of 1.0×10^{15} cm^{-2}. It was also successful to demonstrate "micro-tunnel" in the middle of TiO_2 single crystal (Figure 5). An AFM observation of the bottom of the air gap depicted in Fig. 4 was shown in Figure 6. Roughness was estimated within 2.5 nm.

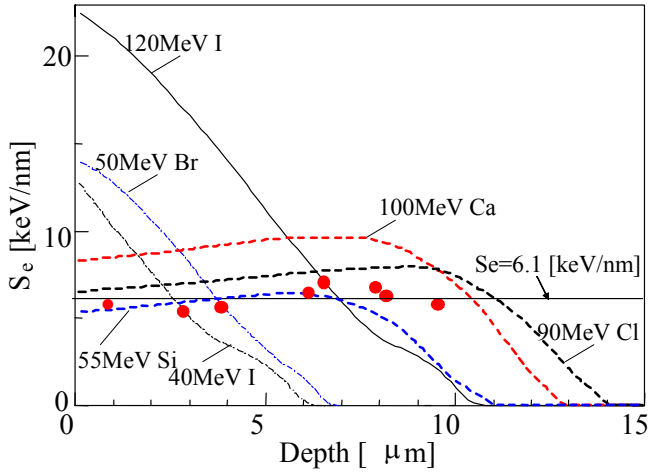

Figure 3. The electronic stopping power against depth calculated by SRIM98. Closed circles were experimental results of etched depth.

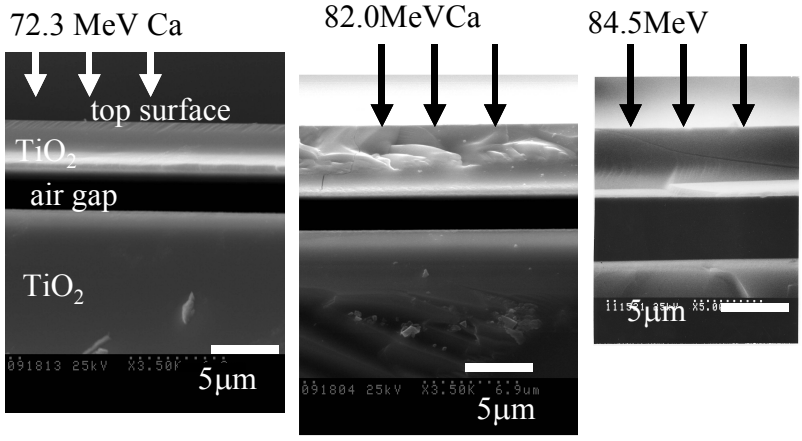

Figures 4. SEM images of the cross section of the sample etched following the (a) 72.3, (b) 82.0, and (c) 84.5MeV Ca ion irradiation to a dose of 3.0×10^{14} cm^{-2}. The ions were irradiated from the top of the image.

Discussion

In XRD spectra shown in Fig.2, the 84.5-MeV Cu ion irradiation decreased the intensities of the peaks assigned to the original rutile crystal structure and induced the two peaks at the lower angular side. According to the Bragg law, a peak shift toward the lower angular side indicated the increase in a lattice constant. Actually, the expansion was observed as the upheaval by ion irradiation. Since TiO_2 crystal in rutile phase has the largest density among TiO_2 polymorphs, it seems that the expansion is due to a structural change induced by the ion irradiation. Decrease in intensities of both peaks at 39.2^o and 84.3^o means the degradation of a crystal structure, i.e. the formation of amorphous phase. From these

considerations, it was found that the ion irradiation induces the amorphous phase and the expansion of lattice in a rutile TiO_2 single crystal. The original peak intensity decreased when the ions were irradiated to a dose of 4.0×10^{12} cm^{-2} (ii), but the intensity hardly changed with further irradiation (see in (iii) and (iv)). It does not imply the remaining of the crystal structure that the original

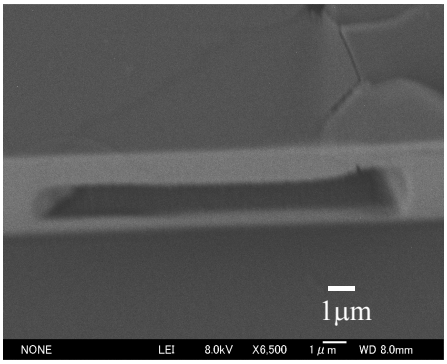

Figure 5. "Micro-tunnel" created by 84.5MeV Ca ion irradiation followed by etching.

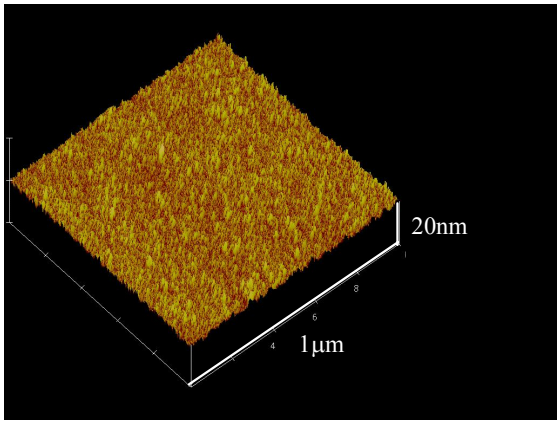

Figure 6. An AFM image of a TiO_2 surface subjected to 72.3MeV Ca ion irradiation at an accumulated dose of 8×10^{13} cm^{-2} through 1μm thick gold mask. Then, chemical etching with 20% hydrofluoric acid was performed for the irradiated sample.

peaks were still existed after irradiation, because x-ray intensity from Cu K_α was reduced by half through 50μm TiO_2 which is deeper than the ion penetration depth. In other words, the undamaged layer below the damaged layer could be detected by XRD measurement.

Conclusion

We have investigated the structural change in rutile TiO_2 single crystal induced by swift heavy-ion irradiation. It has been clarified that a rutile TiO_2 single crystal is not etched by hydrofluoric acid, however, the amorphous region and the stressed lattice region generated by the irradiation of swift heavy ions can be etched by hydrofluoric acid. When the ion whose value of electronic stopping power was decreased with depth of rutile TiO_2 single crystal and the depth that could be etched was limited to the point where the values of electronic stopping power was decayed to 6.2 keV/nm. It was also found that when the ion whose the maximum value of electronic stopping power was located at inside of TiO_2, inside could be selectively etched keeping the surface rutile phase and we can obtain the hollow structure. Energy deposited around the path of the ion showed that there was a threshold whether surface etching can be observed or not. Since the surface and aspect shape of rutile TiO_2 single crystals after etching was very flat in the order of nanometer, it was successful to fabricate 3-dimensional nano-structure by use of this etching technique.

This methods also makes it possible to fabricate rutile TiO_2 plates thinner than a few micron with nano order flatness, which has been difficult by the conventional methods. Our method will be available for the processing of solar cells, photonic catalysts, or photonic crystals, which require nano-fabrication technique.

Acknowledgement

This work was financially supported by the Budget for Nuclear Research of the Ministry of Education, Culture, Sports, Science and Technology, based on the screening and counseling by the Atomic Energy Commission and partly supported by a Grant-in-Aid for Scientific Research from the Ministry of Education, Culture, Sports, Science and Technology (12450132).

Refereces

[1] M. Lanata, M. Cherchi, A. Zappettini, S. M. Pietralunga, and M. Martinelli, Opt. Mat. 17, 11 (2001).

[2] S.Yamazaki, N.Hata, T.Yoshida, H.Oheda, A.Matsuda, H.Okushi, K.Tanaka, J.Physique, 42, C4-297 (1981).

[3] K. Awazu, S. Ishii, K. Shima, S. Roorda, and J. L. Brebner, Phys. Rev. B 62, 3689 (2000).

3.7 Absorption of silicon atoms on gold clusters

M.Kubo, T.X.Li and I.Arai

Recently, a novel metal-silicon cluster,i.e.,a close packed silicon cage surrounding a tungstencluster, has been found in the study of the reactions of tungsten clusters with silane[1]. Such a cluster should be an innovative building block for nanofabrication in the future. So far, both experimental observations[2,3,4,5,6,7,8,9] and theoretical calculations[10,11,12] have been done mainly for a single metal-encapsulated silicon cage cluster. However, few experimantal observations[13,14,15] and no theoretical calculations are available for such a "metal cluster-encapsulated silicon cage" as observed in the recent study. Therefore, we have not understood even a fundamental process underlying the formation of such a novel metal-silicon cluster at all. We have carried out a molecular dynamics simulation for the reactions of metal clusters with silicon atoms instead of silane as a preliminary study for the reactions of metal clusters with silane in order to get an insight into the underlying fundamental process. The calculations were carried out for gold clusters Au_n (n=3 to 14) and tungsten clusters W_n (n=3 to 14).

In the molecular dynamics simulation, we follow the Verlet method[16] to integrate the equations of motion for a many particles system. The fundermental time step for the integration is 2 fs. The system is observed for a time period of 800 ps which is long enough for the system to reach a certain stable state at last. In general, the effective potential should play a crucial role for the evolution of the whole system in problem. In this connection, we refer to the *ab initio* calculations. A Gupta potential [17,18] is used for Au-Au interaction, a Morse potential[19] for W-W interaction, and Lennard-Jones potential[20] for other interactions. Acctually,

(1) Gupta potential $\quad V_G = \sum \left[\varepsilon_0 \sum_{i \neq j} e^{-p\left(\frac{r_{ij}}{r_{0n}}-1\right)} - \sqrt{\xi^2 \sum_{i \neq j} e^{-2q\left(\frac{r_{ij}}{r_{0n}}-1\right)}} \right],$

(2) Morse potential $\quad V_M = D\left[e^{-2\lambda(r-r_0)} - 2e^{-\lambda(r-r_0)}\right],$
and

(3) Lennard-Jones potential $\quad V_{LJ} = 4\varepsilon\left[\left(\frac{\sigma}{r}\right)^{12} - \left(\frac{\sigma}{r}\right)^{6}\right],$

where ε, σ, ε_0, ξ, p, q, D, λ are parameters which are different in materials.

At first, the reaction in which a gold cluster absorbs silicon atoms is simulated. The cluster size is 3 to 14. Both binding energies of absorbed silicon atoms and geometrical structures of resulting systems are examined. Figure 1 is the result. The figure takes a gold cluster size for horizontal axis, binding energy of a silicon atom which is absorbed by a gold cluster for vertical axis. From this figure, we find that the binding energy increases with an increase of cluster size for the cluster size up to 6, while it is almost constant for the cluster size is greater than 6. For comparison, the reaction in which a tungsten cluster absorbs silicon atoms is simulated. The cluster size is 3 to 14. Figure 2 is the result. The figure takes a tungsten cluster size for horizontal axis, binding energy of a silicon atom which is absorbed by a

gold cluster for vertical axis. We find that the binding energy is almost constant for all the cluster size examined.

Figure 3 shows the geometrical structure of resulting system when a gold cluster of the size 6 absorbs a silicon atom. It is shown that the silicon atom enters into the gold cluster and attains its large binding energy surrounded by gold atoms. When the cluster size is changed from 3 to 14, it is found that the number of surrounding gold atoms increases with an increase of cluster size up to 6 and becomes almost constant for the cluster size greater than 6. Figure 4 shows the geometrical structure of resulting system when a tungsten cluster of the size 6 absorbs a silicon atom. It is shown that the silicon atom attaches to a peripheral site of the tungsten cluster. In this case, the number of tungsten atoms attached to the silicon atom is almost constant under the change of cluster size from 3 to 14.

The simulation for gold cluster suggests the existence of substantially new material which has not been expected previously, i.e., a two-components hybrid cluster with a Si-Au core-shell structure, and shows a drastic change in contrast to the case of tungsten cluster in which a W-Si core-shell structure is favoured. We conclude that inter-molecular potentials make such a big difference between a gold-silicon hybrid cluster and a tungsten-silicon hybrid cluster.

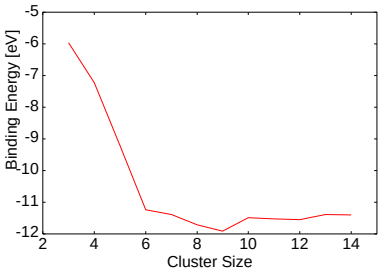

Fig. 1. Relation of a gold cluster size and binding energy of a silicon atom

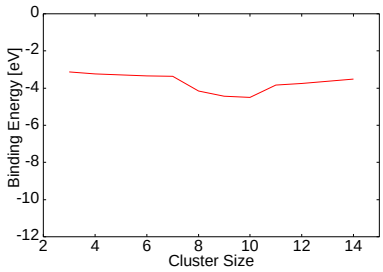

Fig. 2. Relation of a tungsten cluster size and binding energy of a silicon atom

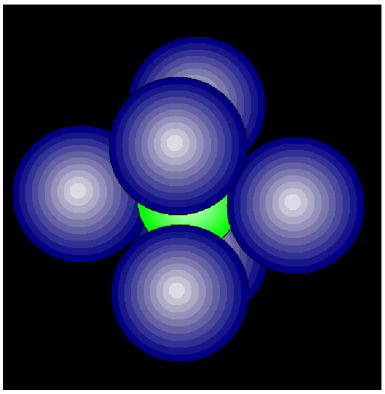

Fig. 3. Final state of $Au_6 - Si$ reaction

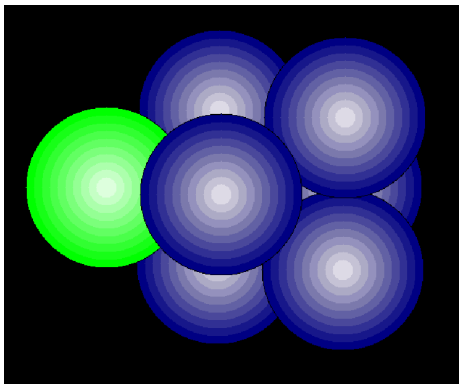

Fig. 4. Final state of $W_6 - Si$ reaction

References

[1] A.Negishi, N.Kariya, K.Sugawara, I.Arai, H.Hiura, and T.Kanayama, Chem. Phys. Lett. **388**(2004)463.

[2] H.Hiura, T.Miyazaki, T.Kanayama, Phys. Rev. Lett. **86**(2001)1733.

[3] T.Kanayama, Jpn. J. Appl. Phys. **33**(1994)L1792.

[4] T.Kanayama, H.Murakami, J. Vac. Sci. Tech. **B15**(1997)2882.

[5] T.Miyazaki, H.Hiura, T.Kanayama, Phys. Rev. **B66**(2002)121403(R).

[6] S.M.Beck, J, Chem. Phys. **87**(1987)4233;
S.M.Beck, J, Chem. Phys. **90**(1989)4233.

[7] M.Sanekata, T.Koya, S.Nagao, Y.Negishi, A.Nakajima, K.kaya, Trans. Matter. Res. Soc. Jpn. **25**(2000)1003.

[8] M.Ohara, K. Kouyasu, A.Nakajima, K.Kaya, Chem. Phys. Lett. **371**(2003)490.

[9] M.Ohara, K.Miyajima, A.Pramann, A.Nakajima, K.Kaya, J.Phys. Chem. **A106**(2002)3702.

[10] V.Kumar, Y.Kawazoe, Phys. Rev. Lett. **87**(2001)045503.

[11] S.N.Khanna, B.K.Rao, P.Jena, Phys. Rev. Lett. **89**(2002)016803.

[12] J.Lu, S.Nagase, Phys. Rev. Lett. **90**(2003)115506.

[13] C.S. Ye, S.Afzaal, S.A.Lee, Y.G.Buun, B.S.Freiser, J. Am. Chem. Soc. **116**(1994)8806.

[14] Y.G.Byun, B.S.Freiser, J. Am. Chem. Soc. **118**(1996)3681.

[15] Y.G.Byun, S.A.Lee, S.Z.Kan, B.S.Freiser, J. Am. Chem. Soc. **100**(1996)14281.

[16] L.Verlet, Phy. Rev. **159**(1967)98. R.P. Gupta, Phys. Rev. **B23**(1981)6265.

[17] F.Cleri and V.Rsato, Phys. Rev. **B48**(1993) 22.

[18] R.P.Gupta, Phys. Rev. **B23**(1981)6265.

[19] P.M. Morse, Phys. Rev. **34**(1929)57.

[20] H.H*ä*kkinen, M.Moseler, and U.Landman, Phys. Rev. Lett **89**(2002)033401-1.

3.8 Charge- and velocity- dependence of charge transfer reaction between HCI and C_{60}

Y. Takanashi, M. Kubo, H. Sasaki[1] and I. Arai

A highly charged ion(HCI), when it comes near a material surface, removes the electrons bound on the surface via an over-the-barrier ionization in presence of its deep Coulomb potential[1]. At the same time, a huge energy is released at around the local site. We have used a C_{60} as a target and observed a charge transfer reaction between a HCI and C_{60}. Such an observation is expected to play a crucial role for understanding the whole ionization process on a material surface caused by an HCI in connection to the corresponding ionization process of a single atom caused by an HCI. In the present study, the observation has been done under changing the charge state of HCI and its velocity systematically.

The experimental setup is as follows. The C_{60} target is prepared by an effusive source with a temperature of 400°C. The HCI beam produced by SHIVA, i.e., an ECR ion source at Tandem Accelerator Center, is led to the interaction region between the extraction electrodes, where the beam crosses the C_{60} molecules, followed by the Time-of-Flight (TOF) mass spectrometer. Actually, the HCI beams of Ar^{q+} (q=4-12, E=5q-15q [keV]) and Xe^{q+} (q=6-30, E=6q-15q [keV]) are used. The secondary ions produced by HCI-C_{60} collision are extracted to the TOF mass spectrometer and analyzed along with their mass-to-charge ratios. Figure 1 shows a typical TOF spectrum of collision products when 60 keV Xe^{12+} beam is applied. The horizontal axis is a TOF and proportional to a square root of mass-to-charge ratio. In the figure, the prominent peaks assigned to the charge states of C_{60} as C_{60}^{+}, C_{60}^{2+}, … , and C_{60}^{6+} are observed.

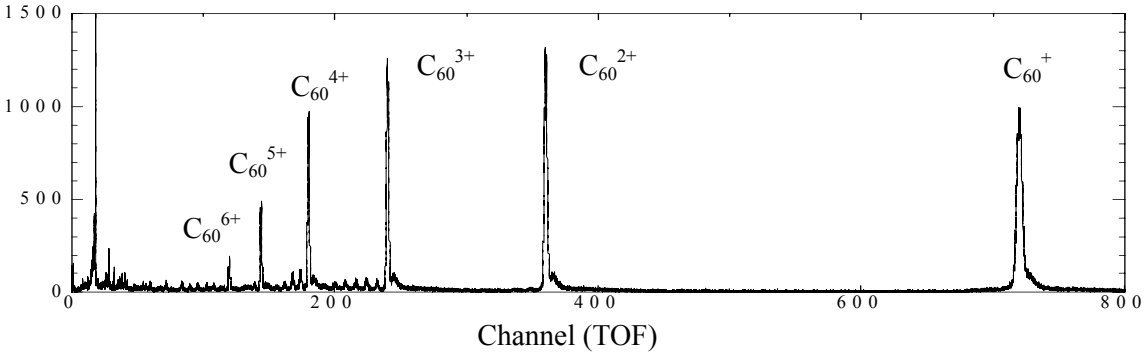

Figure 1. Typical TOF spectrum of collision products for 60 keV Xe^{12+}

The yield Y(n) of each C_{60}^{n+}(n=1-6) ion is obtained by integrating the corresponding peak approximated by a Gaussian distribution function. We define the mean charge Q of C_{60} as follows;

$$Q = \frac{\sum n^2 Y(n)}{\sum n Y(n)}$$

Figure 2 shows the correlation between Q and the charge of projectile HCI as well as the calculations with

use of the classical over-the-barrier (COB) model[2]. It is found that Q seems to become higher approaching the COB model calculations as the charge of projectile HCI becomes higher. As for the correlation between Q and the velocity of projectile HCI, it is found that Q seems to become higher approaching the COB model calculations as the velocity of projectile HCI becomes slower. The similar tendency concerned with the velocity of projectile HCI is also observed in the charge transfer reactions between a metal surface and a HCI [3]. This fact implies a certain similarity between C_{60} and a bulk surface.

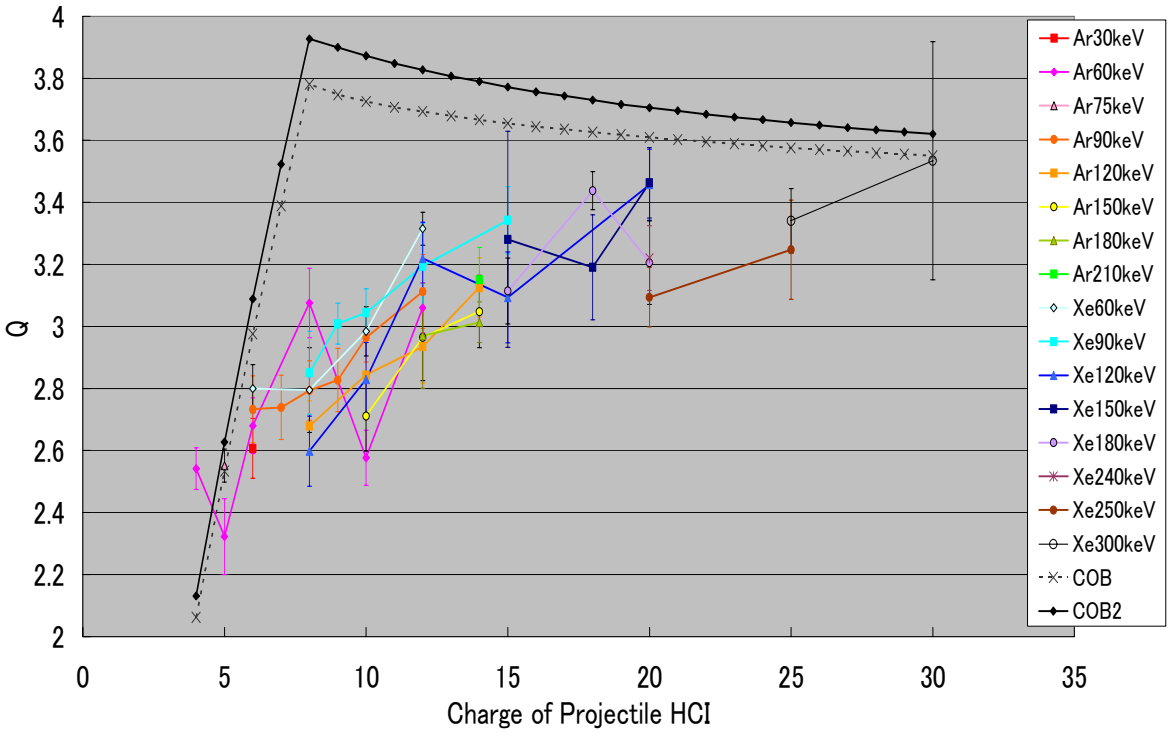

Figure 2. Correlation between Q and the charge of projectile HCI

References

[1] R. Morgenstern et al., *in Proceedings of XXI International Conference on the Physics of Electronic and Atomic Collisions*, Sendai, Japan, 1999, AIP Conf. Proc. No.500, edited by Y. Itikawa et al. (AIP, New York, 2000).

[2] A. Baray et al., Nucl. Inst. and Meth. B98(1995)184.

[3] Q. Yan et al., Phys. Rev. A**54**(1996)641.

3.9 Mössbauer study on Fe nitride fine particles with high coercive force

K. Shibata, A. Hatanaka, E. Kita, H. Yanagihara and Y. Sasaki[1]

Iron nitrides have been studied as nobel magnetic materials for a few decades. A series of stable iron nitrides have been reported such as Fe_4N, Fe_3N and Fe_2N, which show various physical properties.[1] Fe_4N has a cubic perovskite crystal structure and has high Curie temperature of 480 °C with almost the same order of magnetization as α-Fe.[2] A hexagonal structure is realized from Fe_3N and Fe_2N and their Curie temperature changes from 294 °C to near liquid He temperature.[3] A superior mechanical characteristic is seen in this hexagonal iron nitride and has used as materials with excellent lubrication and ablation resistance. Additionally, meta-stable $Fe_{16}N_2$ has a body centered tetragonal structure[4] and was reported to have larger magnetic moment than that of α-Fe.[5] Many have been researched to confirm this giant magnetization.[6]

Many magnetic applications have been attempted by using iron nitrides which have been expected to be more chemically stable compared with metallic materials, for example, head materials which require high saturation magnetization. Stable ferromagnetic metals have been studied in order to develop high density magnetic recording media. Fe_4N metallic fine particles, which were fabricated by nitriding α-Fe fine particle with Ammonia-Hydrogen reaction technique, achieved significant improvement of stability.[7]

Recently, fine particles of $Fe_{16}N_2$ were synthesized from needle shaped α-Fe fine particles utilized for magnetic recording.[8] The magnetization showed slightly smaller amplitude of 170 emu/g than that of bulk $Fe_{16}N_2$. Following the work, spherical ultra fine $Fe_{16}N_2$ particles were produced by nitriding γ-Fe_2O_3 and they showed saturation magnetization of 200 emu/g which is higher than that of the former work. Additionally, high coercive force greater than 2000 Oe was reported on the fine particles.[9] This characteristic that high coercive force is realized in a spherical ferromagnet is quite suitable for the high density recording media.[10]

From the point of nobel particulate recording media, we synthesized $Fe_{16}N_2$ fine particles with Ammonia-Hydrogen reaction technique and studied magnetic properties. In order to understand the magnetic and chemical structure of particles, Mössbauer study was carried out.

The nitridation was carried out similar way described in the literature.[8] A starting material was Fe oxide particles with the diameter of about 20 nm. Prior to the nitriding, the particles was heated in an hydrogen atmosphere to reduce the oxides into metallic. Several tenths gram of oxides particles was set into a small quartz boat and was heated up to 500 °C for 1 to 3 hours. In this process, Fe oxides changed into metallic Fe. Nitridation was carried out by heating particles to a reacting temperature (T_R) in the mixed atmosphere of argon and NH_3 gases. The reacting temperature were varied between 160 and 200 °C. Reaction period was changed between 20 hours and 115 hours. Magnetic measurements was carried out by using a vibrating sample magnetometer(VSM). MH curves were recorded at room temperature and 4.2 K in a maximum magnetic field of 15 kOe. Mössbauer study was carried out at room temperature and 4.2 K. Data were calibrated with natural α-Fe and were analyzed with a least squares fitting program.[11] From the fitting, hyper-fine field(H_{hf}), isomer shift(I.S.) and quadruple splitting(Q.S.) were obtained for

[1]Hitachi Maxell

Table 1. Reaction condition of FeN fine particles. Reaction time was fixed at 40 hours.

Sample	Reacting temperature T_R (°C)	Reacting gas (Ar/NH_3, sccm)	Ms(emu/g)	Hc(Oe)
S21	175	50/50	122.0	1604
S22	178	50/40	107.3	678
S23	174	50/40	106.3	2146
S24	168	50/50	119.4	1846

each sub-spectrum.

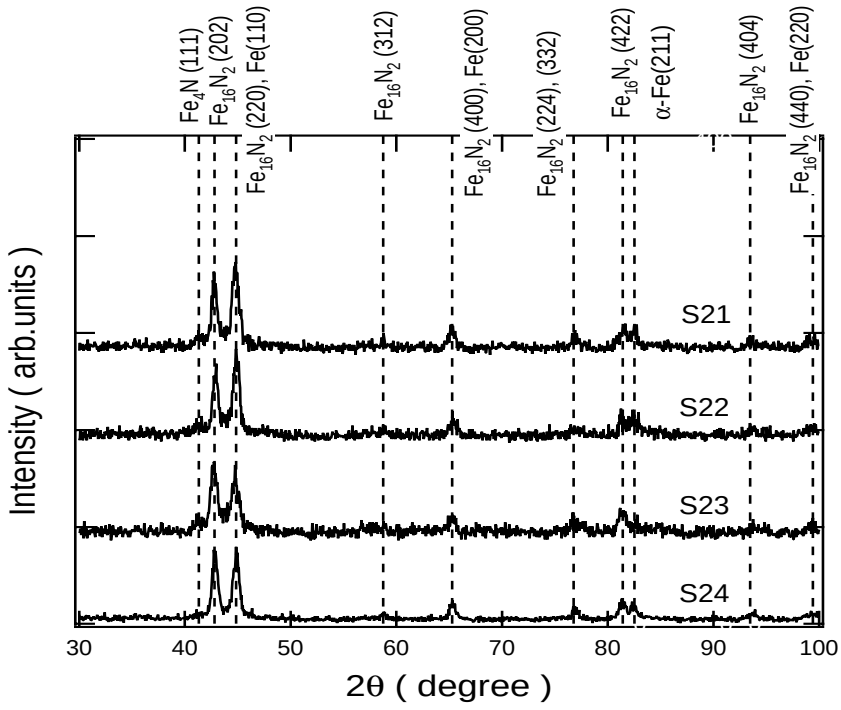

Fig. 1. X-ray diffraction patterns of Fe nitride particles, S21 to S24.

Figure 1 shows typical X-ray diffraction patterns of Fe nitride particles whose reaction condition is summarized in Table 1. Here, reaction time was fixed at 40 hours. Observed diffraction peaks originated mainly from $Fe_{16}N_2$ and slightly from Fe_4N and α-Fe. Especially, in the sample 23, trace of α-Fe was not observed, however small trace from Fe_4N was detected. Other samples showed peaks due to α-Fe even the reaction condition differs very little from the sample 23. It is concluded that the reaction condition is quite sensitive to the composition of products and their magnetic properties.

Magnetic characteristics are also listed in the table. The magnetization was around 110 emu/g which is half of that for α-Fe. It is noted that the magnetization already decreased in 120 emu/g for fine particles after the hydrogen reduction process. The reason is that the magnetization was measured after the exposure of the sample into air and surface of fine particles was oxidized. In contrast, coercive force was widely varied from 800 Oe to 2100 Oe. The highest coercive force of 2100 Oe was obtained in the sample 23. The

amplitude was significantly enhanced by nitriding from the value of 660 Oe for un-nitriding Fe particles.

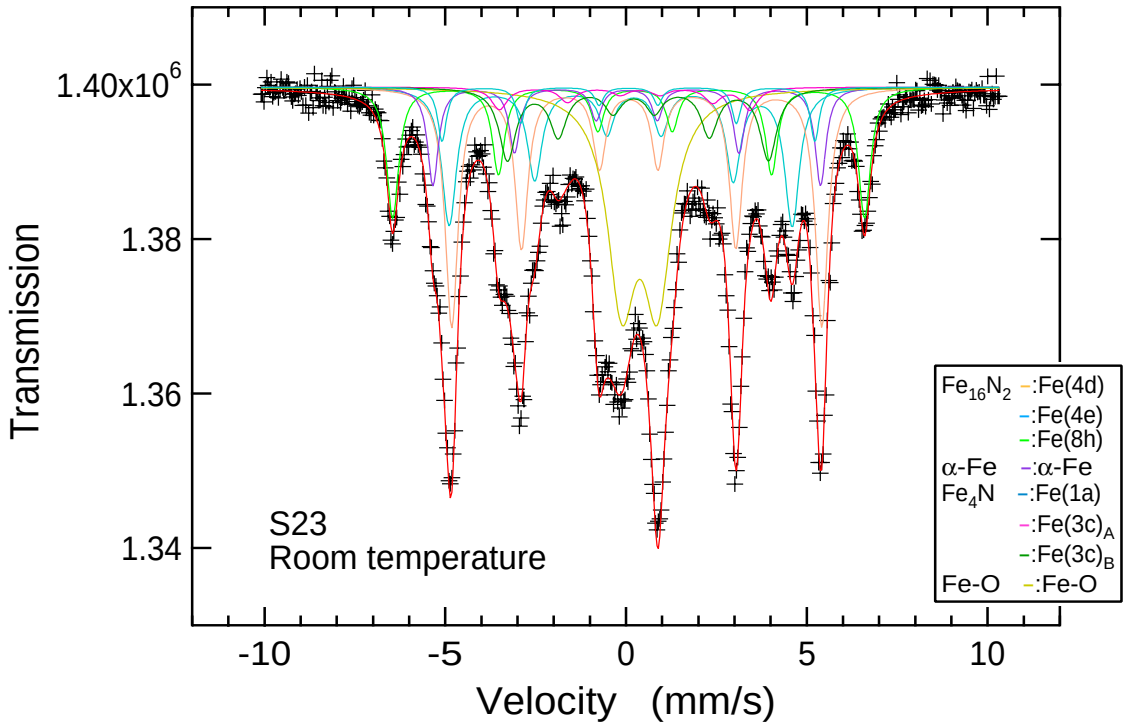

Fig. 2. Mössbauer spectrum of Fe nitride particles, S23, recorded at room temperature.

Table 2. Mössbauer fitting parameters for the sample S23 at room temperature.

Component	Sites	H_{hf} (kOe)	I.S. (mm/s)	Q.S. (mm/s)	Area (%)
$Fe_{16}N_2$	Fe(4d)	294	0.04	-0.37	16
	Fe(4e)	318	0.18	0.22	24.1
	Fe(8h)	405	0.16	-0.18	12.5
Fe_4N	Fe(3c)B	224	0.27	0.12	9.6
	Fe(3c)A	215	0.18	-0.43	2.8
	Fe(1a)	320	0.07	0	3.8
α-Fe		333	0.02	0	8.5
Doublet					22.7

Mössbauer spectra for the sample 23 were recorded at room temperature and 4.2 K (see Figs. 2 and 3). Fitted parameters were listed in Table 2 for room temperature and Table 3 for low temperature. The sub-spectrum with greater hyper-fine field(400 kOe) than that of α-Fe(330 kOe) is clearly seen in the room temperature spectrum. This sub-spectrum is assigned to the Fe(8h) site of $Fe_{16}N_2$. From the low temperature experiment, it is found that about 50 % of Fe atoms belongs to $Fe_{16}N_2$, and 20 % forms in Fe_4N. Surface Fe atoms were evaluated to be 25 % and mainly form magnetically ordered oxides with H_{hf} of 485 kOe and IS of +0,72 mm /s at 4.2 K. These large hyper fine field and isomer shift suggest that the Fe atoms are in divalent. Relatively large distribution in H_{hf} was observed in this sub-spectrum and it implies that the atoms are located at the surface region of the particle with low symmetry. It is noted that this sub-

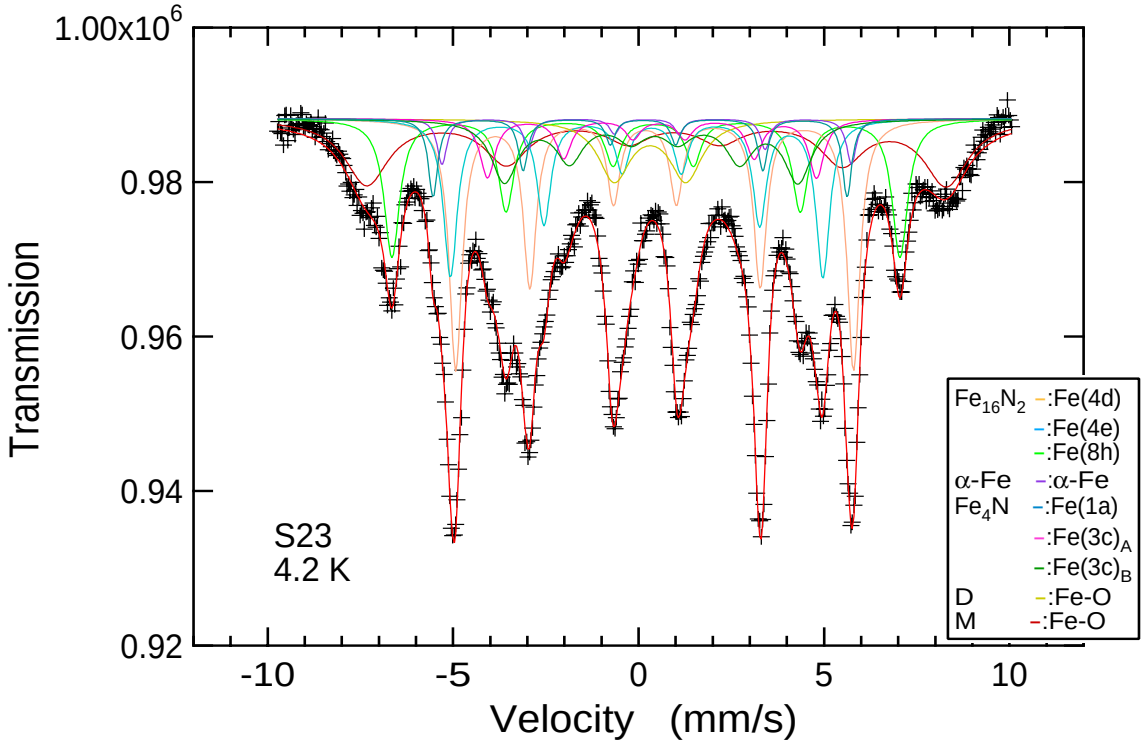

Fig. 3. Mössbauer spectrum of Fe nitride particles, S23, recorded at 4.2 K.

spectrum was not observed in a room temperature spectrum and a non-magnetic doublet appeared. There was no clear change in the temperature dependence of magnetization, therefore the phase with H_{hf} of 485 kOe is concluded to be antiferromagnetic where the transition temperature lies below room temperature.

The reduction of magnetization in an ultra fine Fe particle is usually discussed with the surface oxidization. In the present case, 50 % of reduction was observed, however Fe atoms belonging to the surface region is estimated as 25 %. Assuming that Fe atoms in the $Fe_{16}N_2$ and Fe_4N phases have bulk α-Fe and Fe_4N magnetization (210 and 180 emu/g, respectively), about 150 emu/g of magnetization is expected in the sample 23. This discrepancy might be originated in the imperfect crystal structure in both $Fe_{16}N_2$ and Fe_4N phases. The sample preparation for the magnetic and Mössbauer measurements were carried out in

Table 3. Mössbauer fitting parameters for the sample S23 at 4.2 K.

Component	Sites	H_{hf} (kOe)	I.S. (mm/s)	Q.S. (mm/s)	Area (%)
$Fe_{16}N_2$	Fe(4d)	312	0.15	-0.41	14.3
	Fe(4e)	333	0.3	0.26	21.3
	Fe(8h)	425	0.3	-0.2	14.3
Fe_4N	Fe(3c)B	245	0.39	-0.09	11
	Fe(3c)A	275	0.46	0	5.9
	Fe(1a)	346	0.08	-0.08	4.9
α-Fe		342	0.2	0	2.9
Oxide		485	0.72	-0.48	18.9
Doublet					6.5

air, then oxidization must proceed after the nitriding reaction. The large magnetization about 200 emu/g has been reported in the fine particle sample under the careful handling after the reaction.[9] Next step for this research must be the dealing the samples without exposing to air.

The enhancement of coercive force observed in the nitride fine particle is considered to be due to the formation of the $Fe_{16}N_2$ phase. The crystal structure of this phase is body centered tetragonal (bct) and is distorted from the cubic symmetry. Deformation from cubic symmetry must produce the 2nd order magnetic anisotropy along the elongated axis, which is necessary for the spherical fine particles to have high coercive force. High coercive force is realized in an ordered phase (L_{10}) of face centered tetragonal (fct) materials such as FePt and CoPt, which are leading candidates for the future high density recording media. In this sense, $Fe_{16}N_2$ will be one of them after improving the oxidization resistance.

References

[1] for example see E. Kita and A.Tasaki, Sorid State Physics(Kotai Butsuri), **19**, 721(1984)(in Japanese).

[2] G. Guiland and H. Creveaux, Compt. Rend., **222**, 1170(1946).

[3] N. DeCristofaro and R. Kaplow, Metall. Trans. **8A**, 425(1977).

[4] K. H. Jack, Proc. Roy. Soc. London, **A208**, 216(1948).

[5] T. K. Kim and M. Takahashi, Appl. Phys. Lett., **20**, 492(1972).

[6] for example see J. M. D. Coey, J. Appl. Phys., **76**, 6632(1994).

[7] K.Tagawa, E.Kita and A.Tasaki, Jpn. J. Appl. Phys., **21**, 1596(1982).

[8] A. Nagatomi et al., J. Jpn. Soc. Powder and Powder Metal., **46**, 151(1999) (in Japanese).

[9] T. Hattori, N. Kamiya and Y. Kato, J. Magn. Soc. Jpn., **25**, 927(2001)(in Japanese).

[10] for example see A. Moser *et al*., J. Phys. **D35**, R157(2002).

[11] MossWinn for windows Ver 3.0

3.10 Anelasticity study of nanocrystalline FCC metals

H. Tanimoto, N. Yagi and H. Mizubayashi

1. INTRODUCTION

Polycrystalline materials with an ultrafine crystallite size less than 100 nm are called as nanocrystalline (n-) materials, and have a unique structure in which the ultrafine crystallites are connected by grain boundaries (GBs). When the ultrafine particles are mechanically consolidated, the highly disordered GBs may be formed to accommodate the neighboring ultrafine crystallites. After these considerations, it is expected that the n-material possesses a new property which is different from that of the (p-) crystalline and amorphous solids or the ultrafine particles [1]. In this paper, we report that fully-dense n-Au shows a quite large anelastic strain in the quasi-static measurements above 200 K, and the unique stress dependence of the steady-state creep reflecting the characteristic GB properties in n-Au.

2. EXPERIMENTAL PROCEDURE

The gas-deposition (GD) method was originally developed to draw metallic thin line patterns on a substrate as interconnects [2]. The GD apparatus used for the high-density n-metal preparation is composed of an evaporation chamber, a deposition chamber, a transfer pipe connecting these chambers and a helium circulation system with purification columns [3]. Ultra-fine Au particles formed by a gas condensation process in the evaporation chamber were sucked by the transfer pipe and transferred onto a cooled glass substrate in the deposition chamber. The purity of the helium gas was kept as high as 99.9999 % in order to obtain contamination-free and fully-dense specimens. By controlling the position of the substrate, ribbon like specimens of 23 mm long, 1 mm wide and 20 ~ 500 μm thick were prepared. We shall refer the 23 x 1 mm^2 surface side as the specimen flat surface, hereafter. After the deposition, the specimens were carefully removed from the glass substrate, where no bending and breaking of the specimens were found.

The mean grain size (d) was measured from the STM surface topography and the peak broadening in X-ray diffraction (XRD) peaks. The XRD patterns were measured in a θ-2θ scan mode with Cu-Kα radiation, where the measurements were performed at two different geometrical set-ups, i.e. the scattering vector was normal ($q_{\perp}$ set-up) and parallel ($q_{//}$ set-up) to the specimen flat surface.

The resonant frequency (f) and internal friction (Q^{-1}) measurements were performed by the flexural vibrating reed method at $f \sim 200$ Hz and the strain amplitude of $\sim 10^{-6}$. The stress relaxation measurement was carried out by using the specially tuned Instron-type tensile testing apparatus [3]. Tensile creep test apparatuses designed for a thin ribbon specimen and a compressive creep test apparatus for thick specimens were home-made, where the creep strains under a constant load were measured using an capacitance displacement sensor [4].

3. RESULTS AND CONCLUSION

Quite strong reflections from the (111) planes were observed in the XRD spectrum measured at the $q_{\perp}$ set-up, while various reflections were detected with comparable strengths at the $q_{//}$ set-up. These XRD pat-

terns indicate that almost all the crystallites in n-Au aligned their <111> crystallographic direction being normal to the specimen flat surface. The values of $d_{\perp}$ estimated from the (111), (200) and (220) reflection peaks is about 38, 25 and 20 nm, respectively. The STM surface image of n-Au showed dome-like swells with the mean diameter of about 25 nm and no pores and cracks are observed. The density (ρ) of the n-Au specimens was 19.4 ± 0.2 g/cm^3, and it shows good agreement with ρ_0 = 19.32 g/cm^3 of the bulk Au value in literature. Almost no change in ρ of the present n-Au was observed after the annealing at 1100 K [5].

In the tensile test with the strain rate ($d\varepsilon/dt$) of 1.5 x 10^{-4} s^{-1}, the linear elasticity is found up to strain (ε) of 1 % at 77 K, and up to ε of 0.5 % at 293 K, respectively. At around 300K, n-Au specimens show a fracture strain of 1.5-3%, and the yield stress and tensile strength are about 3 times as large as those measured for annealed p-Au specimens. It is not shown here but in the f and Q^{-1} spectra observed for the n-Au specimen at $\varepsilon \sim 10^{-6}$, a broad relaxation peak and small shoulders accompanied by modulus defects are observed at around 95 K ($Q^{-1}_{p,95K}$, hereafter), 20 K and 50 K [6]. Above 200 K, Q^{-1} and f show a rapid increase and a decrease with increasing temperature ($Q^{-1}_{>200K}$, hereafter). Both $Q^{-1}_{p,95K}$ (including their shoulders) and $Q^{-1}_{>200K}$ almost diminished after annealing for the grain growth [5,7]. For the n-Au specimens, after the low-temperature irradiation with the Frenkel-defect concentration (C_{FP}) up to ~ 100 ppm, $Q^{-1}_{p,95K}$ including their shoulders and $Q^{-1}_{>200K}$ were remained almost unchanged, but f showed a large monotonous increase [6,7]. In contrast, for p-Au after irradiation with C_{FP} < 1 ppm, a large decrease in Q^{-1} and a increase in f (dislocation pinning phenomena) were simultaneously observed. These observations indicate that $Q^{-1}_{p,95K}$ and $Q^{-1}_{>200K}$ are not due to dislocations but to some anelastic processes in the GB regions [8]. The tentative TEM observation showed no dislocations in the present n-Au specimens (not shown here). It is noted that the TEM experiment reported dislocations in the crystallites of n-Au [9] but not in n-Ag [10].

The Young's modulus of n-Au was estimated from the vibrating reed measurements at $f \sim$ 200 Hz and $\varepsilon \sim 10^{-6}$ (E_{vib}, hereafter). The temperature dependence of E_{vib} is shown in Fig. 1 together with that of E_{tensil}, which is the Young's modulus observed from the tensile tests at $d\varepsilon/dt \sim 10^{-4}$ s^{-1} and $\varepsilon \sim 10^{-3}$. Below 200K, the temperature dependence of E_{vib} and E_{tensil} is quite similar to that of the Young's modulus reported for p-Au [11,13]. Above 200 K, both of E_{vib} and E_{tensil} showed deviatory decreases from the Young's modulus of p-Au, where the decrease in E_{tensil} was larger than that of E_{vib}. This is due to the anelastic strain ($\varepsilon_{an,>200K}$) which is thermally activated above 200 K and increases nonlinearly with the increase in the applied stress. It is noted that $Q^{-1}_{>200K}$ is indicative of $\varepsilon_{an,>200K}$, and $\varepsilon_{an,>200K}$ is commonly observed in n-fcc metals. On the other hand, as seen in Fig. 1, the modulus observed at 10 K is free from the anelasticity. The Young's

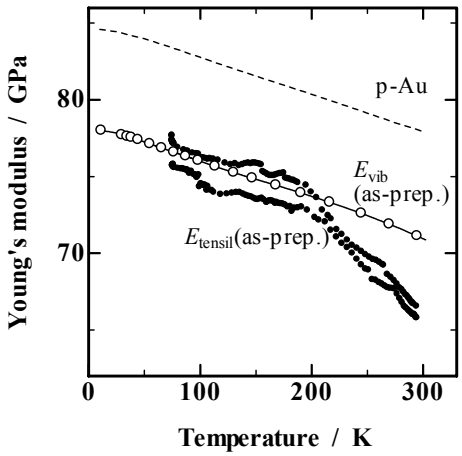

Fig. 1 Temperature dependence of Young's modulus observed for high-density n-Au.

modulus found for the present n-Au specimens at 10 K is almost the same to that of p-Au after taking into account the orientations of constituent crystallites [4, 5]. This fact indicates that the modulus of the GBs is comparable with that of bulk Au.

The decrease in the Young's modulus of n-Au above 200 K is larger at increased strains, and possibly for a long-term test. Figure 2 shows the results of stress-relaxation tests for n-Au, where the stress relaxation was detected above 165 K and its amount increased with increasing temperature [11]. The relaxation time for $\varepsilon_{an,>200K}$ has a wide distribution and the anelastic process associated with the GBs are not of a simple relaxation process. To pursue the anelasticity of n-Au at the higher stresses, we carried out the creep test for 80 ks and the recovery test were sequentially made as a function of the applied stress (σ_{ap}) and temperature. The strain found just after unloading (ε_{80ks}) is composed of an anelastic strain ($\varepsilon_{an,GB}$, where $\varepsilon_{an,GB} \sim \varepsilon_{an,>200K}$) and a plastic creep strain ($\varepsilon_{pc,80ks}$). $\varepsilon_{an,GB}$ showed a saturation after 50 ks at 300 K. Figure 3(a) shows ε_{80ks} as a function of σ_{ap} which were observed at 295, 310 and 320 K. Figures 3 (b) and (c) show $\varepsilon_{an,GB}$ and $\varepsilon_{pc,80ks}$ found near 80 ks as a function of σ_{ap}, respectively. From Fig. 3(b), $\varepsilon_{an,GB}$ increases linearly with increasing σ_{ap} beyond the threshold stress (σ_{anI}) of a few MPa. It is noted that the stress level in the vibrating reed measurements with $\varepsilon \sim 10^{-6}$ was below σ_{anI}. A ratio of $\varepsilon_{an,GB}$ to an elastic strain (ε_{el}) is as large as 1.1 at 320 K and 0.7 at 295 K for the present n-Au specimens, indicating that $\varepsilon_{an,GB}/\varepsilon_{el}$ decreases with decreasing temperature toward 200 K.

$E_{an,GB}$ for the early stage of the stress relaxation study is reported to be 0.2 eV [11] which is much lower than the activation enthalpy of 0.88 eV reported for the GB diffusion in p-Au. Since a simple diffu-

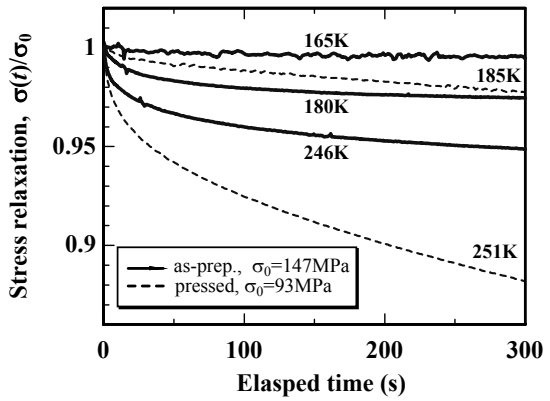

Fig. 2 Stress relaxation curves observed for n-Au in the as-prepared state and after the press.

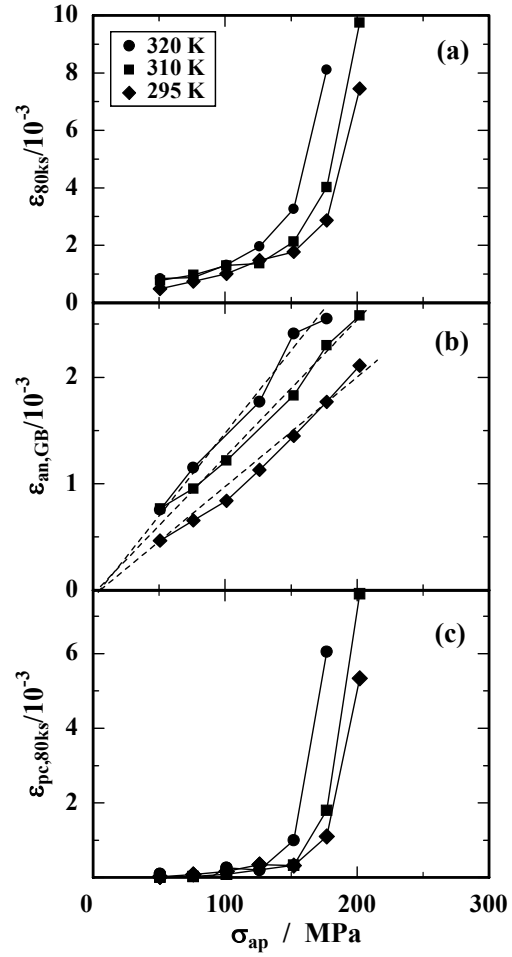

Fig. 3 Total (a), elastic (b) and plastic (c) strains observed for n-Au after removing the constant load for 80 ks.

sion process with an activation enthalpy of 0.2 eV is well stimulated at 200 K, a value of the pre-exponential factor for the atomic motion responsible for $\varepsilon_{an,GB}$ should be very low. Recent molecular dynamics simulation studies for the GB diffusion [12, 13] and the GB migration [14] reported that cooperative motions of many atoms can be excited above a certain temperature, which results in a low activation enthalpy and a low pre-exponential factor. We surmise that such a cooperative atomic motion of many atoms is responsible to $\varepsilon_{an,GB}$ in the present n-Au. The wide distribution of the relaxation time for $\varepsilon_{an,GB}$ may be associated with the scale of the cooperative motions.

Acknowledgements

This work is partly supported by a Grant in Aid for Scientific Research from the Ministry of Education, Culture, Sports, Science and Technology of Japan and High Damping Materials Project of "Research for the Future" of Japan Society for the Promotion of Science.

References

1. H. Gleiter, Prog. Mater. Sci., 33(1989)223-315.
2. S. Katus, E. Fuchita, T. Tanabe and C. Hayashi, Jpn J. Appl. Phys., 23(1984)L910 : E. Fuchita, M. Oda and C. Hayashi, Materia Japan, 44(1995)455 (in Japanese).
3. S. Sakai, H. Tanimoto and H. Mizubayashi, Acta Mater., 47(1999), pp. 211-217.
4. S. Sakai, Thesis, University of Tsukuba, (2001).
5. H. Tanimoto, S. Sakai and H. Mizubayashi, Mater. Trans., 44(2003), pp. 94-103.
6. H. Tanimoto, H. Mizubayashi, H. Fujita and S. Okuda, J. de Phys., 6(1996)C8-199-202..
7. H. Tanimoto, S. Sakai, and H. Mizubayashi, Proc. ICIFUAS-13, submitted.
8. H. Tanimoto, S. Sakai, K. Otsuka, E. Kita and H. Mizubayashi, Proc. ICIFUAS-13, submitted.
9. S. Okuda, J. Alloy Comp., 310(2000)124
10. S. Ichikawa, K. Miyazawa, H. Ichinose and K. Ito, Nanostruc. Mater., 8(1999)1301.
11. S. Sakai, H. Tanimoto, K. Otsuka, T. Yamada, Y. Koda, E. Kita and H. Mizubayashi, Scripta Mater., 45(2001), 1313.
12. M.R. Sørensen, Y. Mishin and A.F. Voter, Phys. Rev. B, 62(2000)3658.
13. P. Keblinski, D. Wolf, S. R. Phillpot and H. Gleiter, Phil. Mag. A, 79(1999)2735.
14. B. Shönfelder, D. Wolf, S. R. Phillpot and M. Furtkamp, Interface Sci., 5(1997)245 : B. Shönfelder, P. Keblinski, D. Wolf and S. R. Phillpot, Mater. Sci. Forum, 294, 9 (1999).

3.11 The science of 3d transition-metal oxide system (2003–2004)

M. Onoda, J. Hasegawa, T. Ikeda, T. Ohki, T. Harigae, S. Miyasaka, T. Mutoh, T. Isobe and K. Takao

The structural and electronic properties of 3d transition-metal oxides and bronzes have been explored by means of x-ray four-circle diffraction and through measurements of magnetic resonance (NMR and EPR), magnetization, and electronic transport, in order to extract characteristic properties in the correlated electron system, electron-phonon-coupling system, quantum spin-fluctuation system, and novel materials. At the Tandem Accelerator Center, Varian continuous-wave and Bruker pulse NMR spectrometers have been used.

In 2003–2004, the following investigations were performed and a part of them have been published elsewhere [1–3]:

- Quantum spin-fluctuation system
  - Geometrical frustrations in $Cd_xZn_{1-x}V_2O_4$ and $LiV_{2-x}M_xO_4$ (M = Al and Ga)
  - Spin-gap states in δ-$M_xV_2O_5$ (M = Ag, Tl, Na, K and Sr)
- Correlated-electron and electron-phonon-coupling systems
  - Metal-insulator transitions in V_6O_{13} and $Cu_xV_4O_{11}$
- A new type of superconductors
  - Superconducting properties of $Na_xCoO_2{\cdot}yH_2O$
  - Geometrical frustrations and electronic properties of Na_xCoO_2 and Li_xVO_2
- Composite crystal system
  - Superspace group approach to $Cu_xV_4O_{11}$
- Secondary ion battery system
  - Li inserition effects in $M_{1+x}V_3O_8$ (M = Li, Na and Ag), $Ag_2V_4O_{11}$, $Cu_xV_4O_{11}$ and V_6O_{13}

This report describes briefly recent progress for the secondary ion battery system.

Secondary ion battery system

$Li_{1+x}V_3O_8$ is one of several vanadium oxide systems that have received considerable attention as an insertion electrode. This system can accommodate around three or ideally four additional Li ions per formula unit (namely $x = 3-4$).

For $Li_{1+x}V_3O_8$ with $x < 2$, there exist three crystallographically independent V sites (V1, V2 and V3). The V1 ions apparently have a pyramidal coordination, while the V2 and V3 ions are surrounded octahedrally. The V_3O_8 framework is comprised of the chains of VO_6 octahedra and those of VO_5 pyramids extending along the monoclinic *b*-axis. These chains are connected by corner-shared oxygens to lead to continuous sheets of V−O polyhedra. The networks for the equivalent V1 and V2 sites are expressed as zigzag chains and that for the V3 site is a one-dimensional chain. Although the linkage for the inequivalent sites complicates matters, the spin networks responsible for magnetic properies are often simplified due to the symmetry of the ground-state wavefunction for each V site. The Li ions are located predominantly in an octahedral Li1 site (occupancy probability = 1.0). The excess *x*Li ions reside in a tetrahedral Li2 site. In the highly lithiated crystal $Li_4V_3O_8$ ($x = 3$), a defect rock-salt structure is formed and all of Li ions are coordinated octahedrally.

Although the crystal structures and electrochemical properties of $Li_{1+x}V_3O_8$ system have been investigated in detail, there is little information on the electronic properties as a function of *x*. This work is

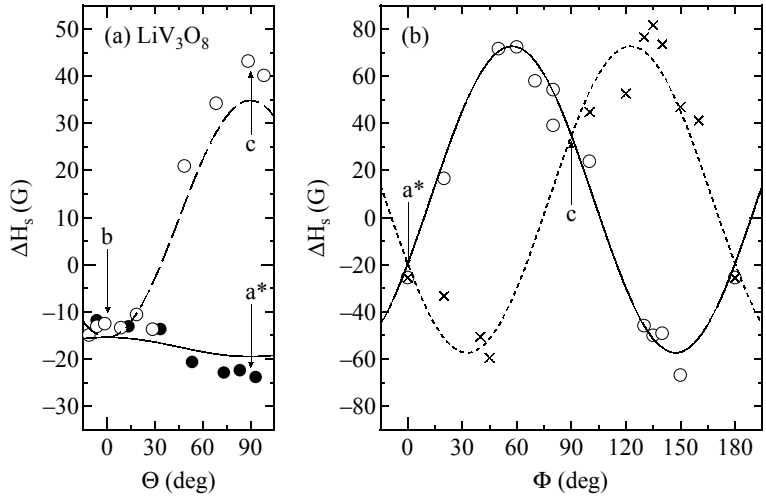

Fig. 1: The angular dependences of the interval ΔH_s between the ^{7}Li quadrupole satellites for $m = \pm\frac{3}{2} \leftrightarrow \pm\frac{1}{2}$ in LiV_3O_8 at 15 MHz: (a) ba^*- and bc-planes; and (b) a^*c-plane. Here, all of the curves are calculated with parameters given in text.

performed in order to clarify the configuration of Li ions in $Li_{1+x}V_3O_8$ for wide compositions through NMR and magic-angle-spinning (MAS) measurements.

The Knight shift of ^{7}Li nuclei for the single crystals of LiV_3O_8 is absent, which indicates that the atoms are completely ionized. The angular dependences of the interval ΔH_s between the ^{7}Li quadrupole satellites for $m = \pm\frac{3}{2} \leftrightarrow \pm\frac{1}{2}$ at 15 MHz are shown in Fig. 1. Generally, the angular dependence of ΔH_s is expressed by

$$\Delta H_s = H_Q(3\cos^2\theta - 1 + \eta\sin^2\theta\cos 2\phi), \tag{1}$$

where H_Q is the quadrupole field, η is the asymmetry parameter of electric field gradient (EFG), and θ and ϕ are the polar and azimuthal angles of the magnetic field with respect to the principal axes of the EFG tensor, respectively. On the basis of the data for ba^*-, bc- and a^*c-planes, the quadrupole field, the asymmetry parameter and the directions of the principal axes are determined as: $H_Q = 36(1)$ G, $\eta = 0.58(5)$, $\angle(Z, a^*) = 57(1)$ deg and $X \parallel b$. The directions of the EFG tensor are consistent with those calculated from the point-charge model for the Li1 site using atomic parameters determined by Onoda and Amemiya [1]. However, this model provides a small value $\eta = 0.06$ as compared with the experimental result.

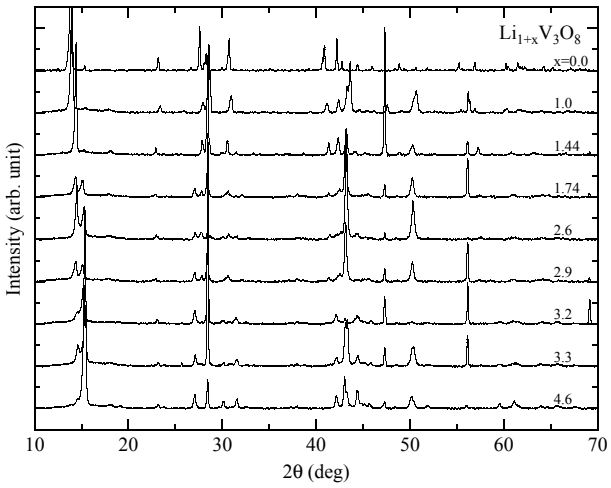

Fig. 2: The composition dependence of the x-ray diffraction patterns with Cu Kα radiation for $Li_{1+x}V_3O_8$ prepared by the solid-state reaction ($x = 0$) and the electrochemical reaction ($x \neq 0$).

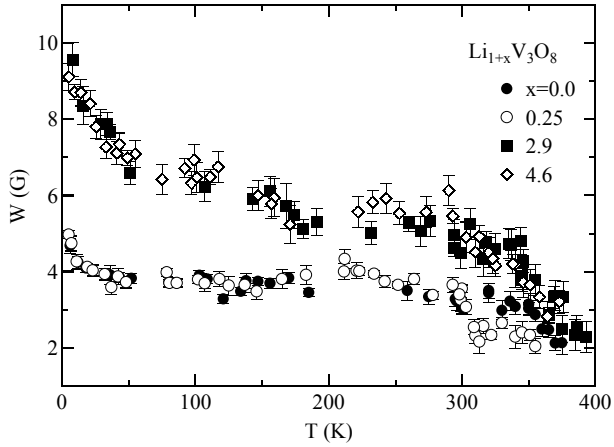

Fig. 3: The temperature dependences of the peak-to-peak linewidths of absorption derivatives for ^{7}Li nuclei in $Li_{1+x}V_3O_8$ at 15 MHz.

Figure 2 indicates the x-ray diffraction patterns with Cu Kα radiation for the specimens prepared by the solid-state reaction ($x = 0$) and the electrochemical reaction ($x \neq 0$). For $Li_{1+x}V_3O_8$, it is known that there exist two kinds of phase corresponding to the small x compound ($0 \leq x < 2$) and the large x one ($x \geq 3$), which are called the L1 and L4 phases, respectively. In this work, the single phase of L1 and that of L4 appear for $x \leq 1.5$ and $x \geq 4.0$, respectively. The specimens with $1.5 < x < 4.0$ have a mixed phase of L1 and L4. The reason why the concentration of $x = 4.6$ given in Fig. 2 is larger than a maximum value for L4 phase is that the excess Li ions are doped in acetylene-black.

For the compounds with $x = 0.25$, 2.9 and 4.6, the Li Knight shifts are absent as in the case of LiV_3O_8. Since the specimen with $x = 2.9$ has the presence ratio of L4/L1 $\simeq 1$ from the intensity ratio of x-ray diffraction patterns, the resonance lines ascribed to the L1 and L4 phases should appear. However, only the single line is observed, which suggests that the Li signal for the L1 phase is masked with that for the L4 phase and/or the local environment around Li ions for the maximum concentration in the L1 phase is similar to that for the L4 phase. The temperature dependences of the peak-to-peak linewidths W of absorption derivatives at 15 MHz are shown in Fig. 3. The data for $x = 0$ and 0.25 are significantly smaller than those for $x = 2.9$ and 4.6. For all of the compounds, a significant decrease of the linewidth with increasing temperature occurs above room temperature, which should be attributed to the motion of Li ions. For $x = 2.9$ and 4.6, a similar behaviour is also observed below 50 K.

The linewidth $\langle W \rangle_{\rm dip}$ due to the dipole interaction is estimated through the relation of

$$\langle W \rangle_{\rm dip} = 2\sqrt{\langle M_2 \rangle_{\rm Li-Li} + \langle M_2 \rangle_{\rm Li-V} + \langle M_2 \rangle_0}, \tag{2}$$

where $\langle M_2 \rangle_0$ is the residual second moment at high temperatures and $\langle M_2 \rangle_{\rm Li-Li(V)}$ is the second moment for Li-Li(V) pairs defined by

$$\langle M_2 \rangle_{\rm Li-Li} = \frac{9}{4}\gamma_{\rm Li}^2 h^2 \sum_k \frac{1}{r_k^6}, \quad \langle M_2 \rangle_{\rm Li-V} = \frac{21}{5}\gamma_{\rm V}^2 h^2 \sum_k \frac{1}{r_k^6}, \tag{3}$$

$\gamma_{\rm Li(V)}$ and h being the gyromagnetic ratio of Li(V) and Plank's constant, respectively. The values for $x = 0$, 0.25, 3 and 4 calculated based on the available lattice constants and atomic parameters are $\langle W \rangle_{\rm dip} = 2.9$, 3.5, 9.9 and 11.7 G, respectively. Therefore, it may be concluded that for $x = 0$ and 0.25, Li ions form rigid lattices below room temperature, while for $x = 2.9$ and 4.6, they are ordered at the lowest temperature.

Above room temperature, the activation energies of the Li motion for $x = 0$, 0.25, 2.9 and 4.6 are estimated with the equation of $W - W_0 \propto \exp(E_{\rm g}/T)$, W_0 being the residual width, as follows: $E_{\rm g} \simeq 5.2$, 6.7, 3.1 and 1.3×10^3 K, respectively. The $E_{\rm g}$ values for the large x are rather smaller than those for the small x. This may be originated from a large Coulomb repulsion between Li ions for the large x.

In summary, the configurations of Li ions in $Li_{1+x}V_3O_8$ for wide nominal compositions of $0 \leq x \leq 4.6$ are clarified through ^{7}Li-NMR. For $x = 0$, the quadrupole interaction parameters for the Li1 site are determined precisely. The motion of Li ions is observed above room temperature for all of the compositions. Below room temperature, Li ions for the small x are almost ordered, while for the large x, the Li ions move in a wide temperature region due to a large Li-Li Coulomb repulsion. The MAS-NMR measurements and the analysis are now in progress.

References

[1] M. Onoda and I. Amemiya: J. Phys.: Condens. Matter **15** (2003) 3079–3093.

[2] U. Manju, S. R. Krishnakumar, S. Ray, S. Raj, M. Onoda, C. Carbone and D. D. Sarma: Proc. Indian Acad. Sci. (Chem. Sci.) **115** (2003) 491–498.

[3] K. Okazaki, H. Wadati, A. Fujimori, M. Onoda, Y. Muraoka and Z. Hiroi: Phys. Rev. B **69** (2004) 165104-1–165104-7.

4.1 Status of Tsukuba AMS system

Y. Nagashima, R. Seki, K. Sasa, T. Takahashi, T. Matsuhiro, K. Sueki

The molecular pilot beam method we have developed is a principal of our AMS system. Applying this method to our traditional big, 12MV acceleration voltage, Pelletron tandem accelerator, we have realized successfully an accelerator mass spectrometry (AMS) without any modifications on the tandem system.

In order to improve the beam intensity from the ion source, a supporting structure for the exit slit of the ion source has been changed from fixed type to adjustable one. The slit can be moved in the plane perpendicular to the beam direction. The beam current emerging from the ion source became about double after the slit position was adjusted properly. The double score of the current helps very much to shorten the measurement time and to improve the statistics of the counts.

As one of the instrumental improvements, in the last year, two beam profile monitors were prepared and has been installed into both an exit of an AMS ion-source and the first focus point of an AMS beam line for ^{36}Cl particle detection. We were expecting that these beam profile monitors help us to find the optimum parameters of the optical elements. But, though the later one works well and is useful to transport the beam properly, the ability of the former one is in sufficient because the location of it is out of focus point.

If the AgCl samples were kept in the air for one day, the Sulfer will be built up on the face of the AgCl sample and consequently the strong Sulfur contamination will disturb to count the ^{36}Cl particles up. In order to keep free from the Sulfur contamination, AgCl samples have been prepared just before the AMS measurement. However, this way limits the number of the samples prepared because of lack of enough time for preparation. So, a vacuum chamber with an oil free evacuation system, DRYTEL Model 1025, has been developed for keeping the samples in the oil free vacuum circumstances. There are no observations of Sulfur increments in the measurements of samples that are preserved in the chamber for 2 weeks. This chamber allows us to prepare samples not only just one day before the measurement but also several days before.

In order to discriminate ^{36}Cl from ^{36}S more clearly on the ΔE - E data map, a new gas counter that consists of two gas ΔE sections, ΔE_1 and ΔE_2, and a SSD E has been developed. By using one ΔE signal as a discrimination gate, Sulfur reduction ratio in ^{36}Cl measurement is improved about 2%. Details are described in the following section.

Up to now, Al- ions produced in the ion source are using for the ^{26}Al AMS. Though the merit of Al- ion lies on no simultaneous creation of Mg- ions and no interferences by the Mg ions, the intensity of Al- is not enough strong for measuring of very rare ^{26}Al sample such as one ^{26}Al element in 10^{13} elements of ^{27}Al. So, in this year, the development of ^{26}Al AMS method using AlO^- molecular ions has been commenced. A few μA of AlO^- current can be produced and it is a few ten times of Al^- current. Fig. 1 shows the outline of the ^{26}Al-AMS system. The method introduced into the system is similar to that of ^{36}Cl AMS. The acceleration voltage is controlled precisely by a slit current feedback system. $^{26}MgO^-$ molecular

ions are created simultaneously with AlO- ions in the ion source in order to produce the slit current with $^{26}Mg^{7+}$ beam. In general, MgO^- molecular ions are abhorred in the case of ^{26}Al AMS because the strong ^{26}Mg yields causes the strong background and consequently disturbed the ^{26}Al measurement. Nevertheless, we try to use them positively as a control current. A 2nd stripper foil plays a role of full stripped $^{26}Al^{13+}$ creation. After passing through the 2nd stripper foil, $^{26}Al^{13+}$ ions are selected and detected as a ^{26}Al element without ^{26}Mg disturbance because of no $^{26}Mg^{13+}$. The abundance of $^{26}Al^{13+}$ is about 10%. The ^{26}Al detection efficiency with AlO^- ions becomes about 4 times better than that of the case with Al^- ions. The sensitivity of ^{26}Al detection is better than 1×10^{15}.

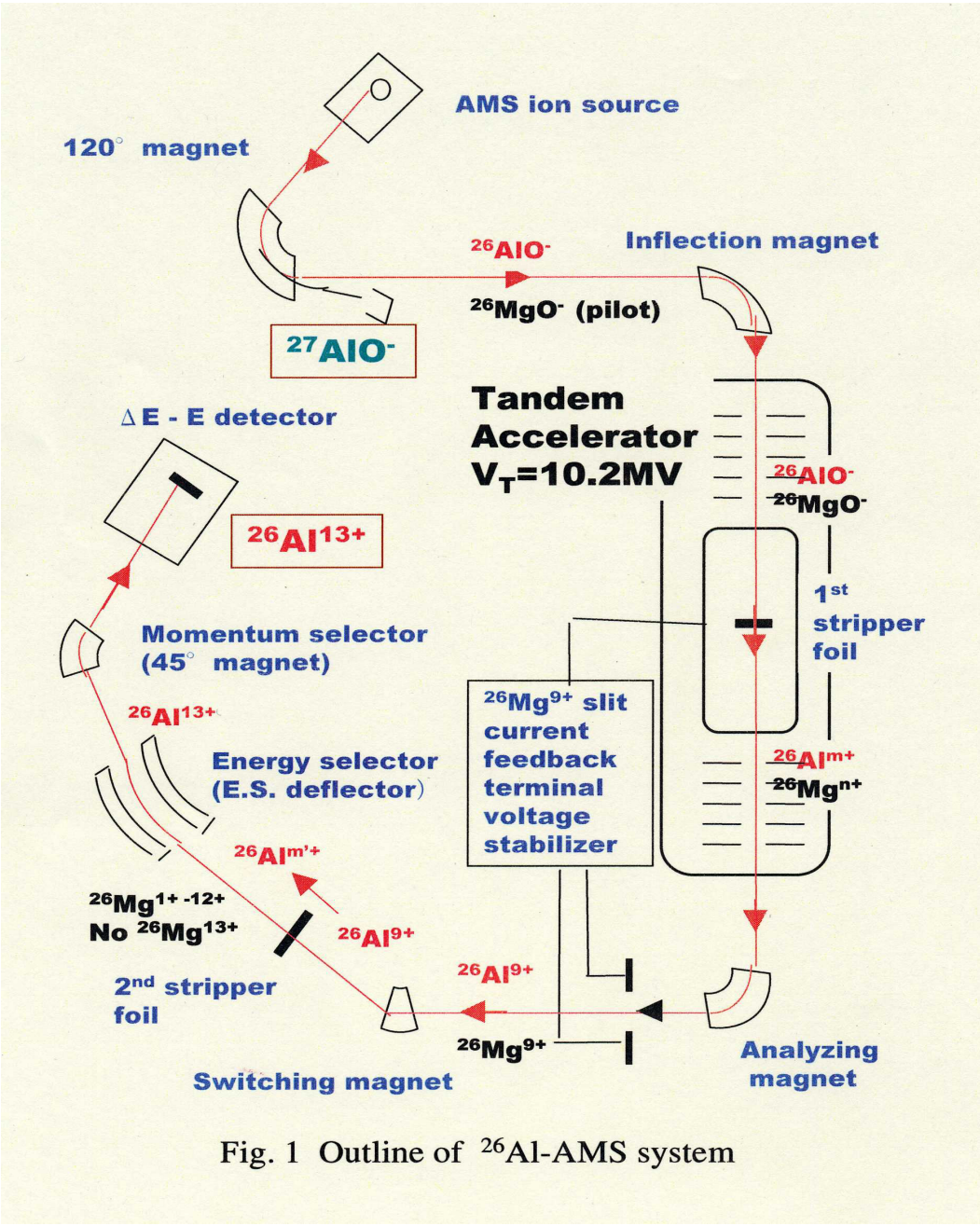

Fig. 1 Outline of ^{26}Al-AMS system

4.2 Development of a multi gas ΔE - SSD E counter telescope for AMS study

He Ming[1], Y. Nagashima, K. Sasa, R. Seki, T. Takahashi, T. Matsuhiro, and K. Sueki

Particle identification is sometimes essentially requested in the AMS measurements. In case of ^{36}Cl AMS, clear identification of a ^{36}Cl particle from a ^{36}S background can improve the sensitivity of the ^{36}Cl detection. Up to now, we are using a gas ΔE - SSD E counter telescope in the ^{36}Cl measurement. Combining with chemical procedures for Sulfur reduction in the stage of sample preparation, the counter telescope can clearly separate the ^{36}Cl particle and the ^{36}S background and detect clearly the ^{36}Cl coming from the sample which has 10^{-13} ratio of ^{36}Cl to Cl. However, in proportion to decreasing of ^{36}Cl content such as 10^{-14} ratio, ^{36}S background becomes relatively strong and ^{36}Cl is buried in the ^{36}S background. In order to improve this condition, a new counter telescope which consist of two gas ΔE sections and an ion implanted SSD with 45mm×45mm active area has been developed. Fig. 1 shows the outline of the counter. A 7.5μm thick poliimido foil, (Kapton, Tore-Dupon Co.), is used as an entrance window. The reasons why we chose the Kapton foil are that 1) Kapton foil is strong to the radiation damage and 2) there is no observation of gas leakage at 100mbar gas, pure iso-butane gas, pressure. After passing through the Kapton foil, a 90MeV ^{36}Cl particle losses it's energy of about 21MeV. This large energy missing causes a lowering of particle identification ability. So, a 3.5μm thick myler foil has been tried to use instead of the Kapton. The small gas leak, however, observed even if at 20mbar gas pressure. It is trying to find out a proper thin and strong foil, but at this moment it is not yet.

Before throwing this in the AMS experiment, optimum operating conditions were examined by using Americium α. One of the results is shown in Fig. 2. The resolution of ΔE output improves with the increase of grid voltage and reaches to the maximum at around 350V. The optimum grid and anode voltage for a 90MeV ^{36}Cl measurement with 40torr gas pressure are 330V and 430V, respectively. The energy losses, $\Delta E/\Delta x$, of ^{36}Cl, ^{36}S, ^{35}Cl and ^{37}Cl particles in the gas ΔE sections are schematically demonstrated in Fig. 3. The SSD measured the residual energy and gas pressure is set as the residual energy difference between ^{36}Cl and ^{36}S becomes maximum.

Fig. 4 demonstrates that how efficient the ΔE signal is when it is used as the gate information. A left figure in Fig. 4 shows the ^{36}Cl yield taken with ΔE_1 gate. A right side one shows the raw data. The difference, though it is not so large, can be seen. A tail of ^{36}S background is comparably suppressed and consequently ^{36}S background yield in the ^{36}Cl yield becomes small.

[1] Present address : China Institute of Atomic Energy

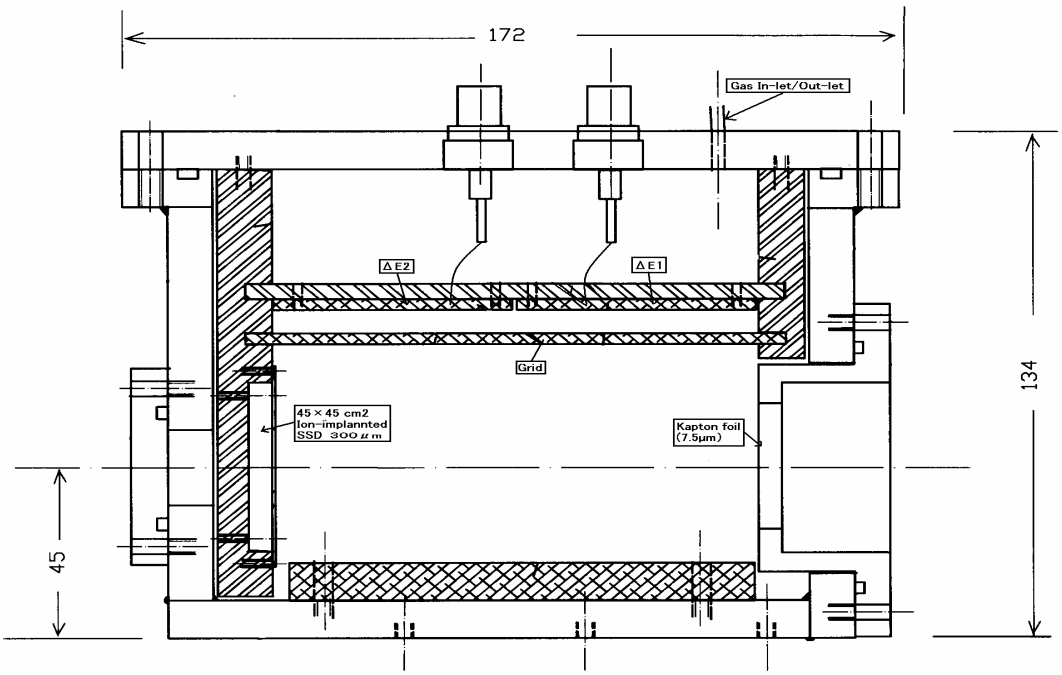

Fig. 1 Cross section of a gas ΔE - SSD E counter telescope. The counter consist of two gas ΔE sections and an ion implanted SSD with 45mm×45mm

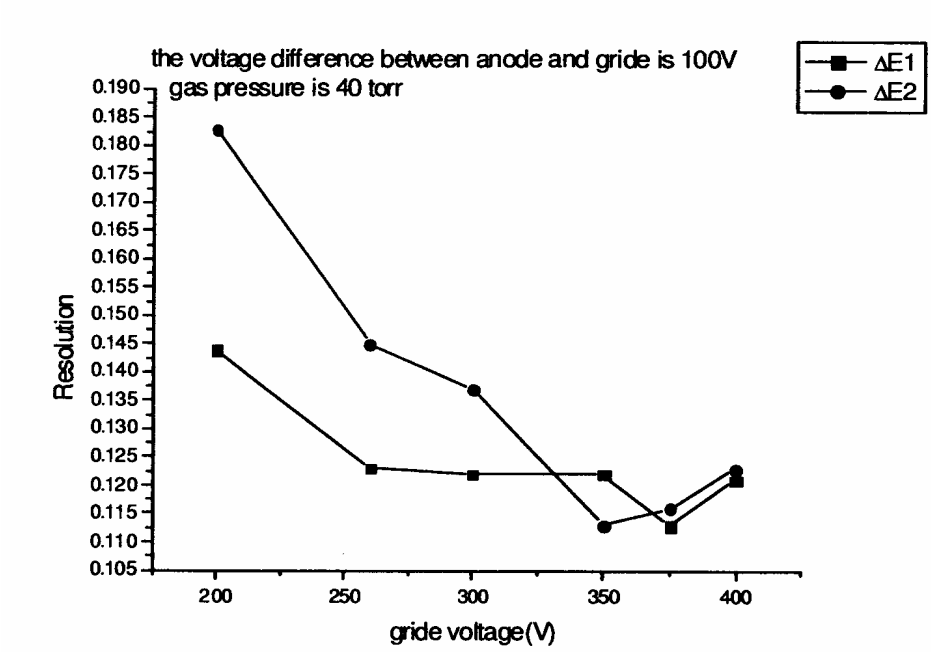

Fig. 2 Grid voltage vs. Energy resolution. The iso-butane gas pressure is 40torr

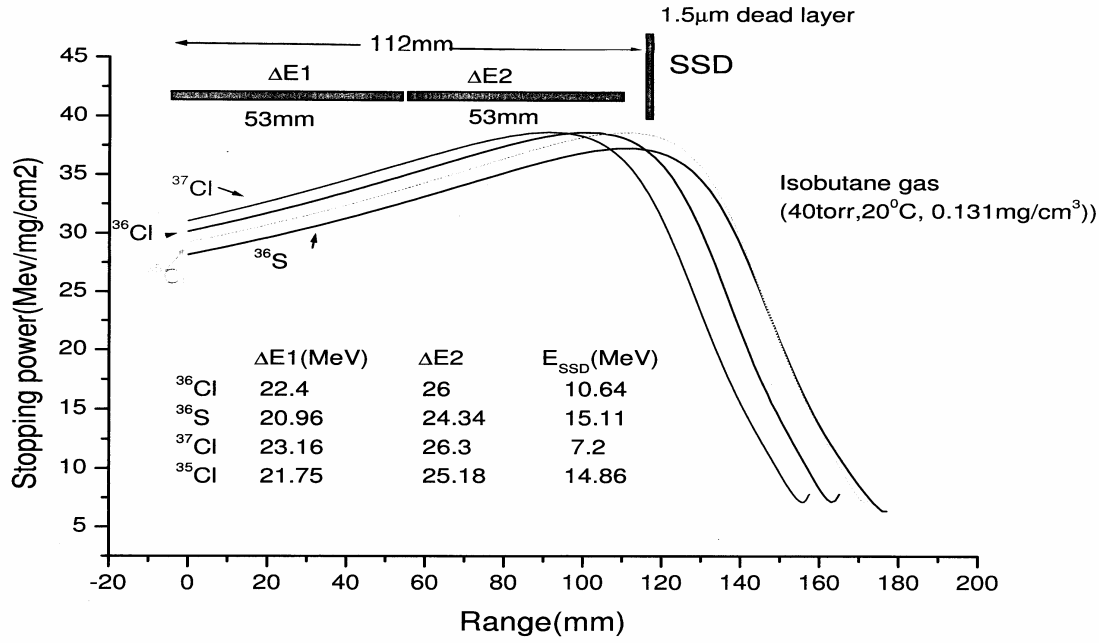

Fig. 3 Particle range vs. stopping power. The ^{36}Cl with 90MeV is assumed. The energy loss in the Kapton foil, about 20MeV, is counted in.

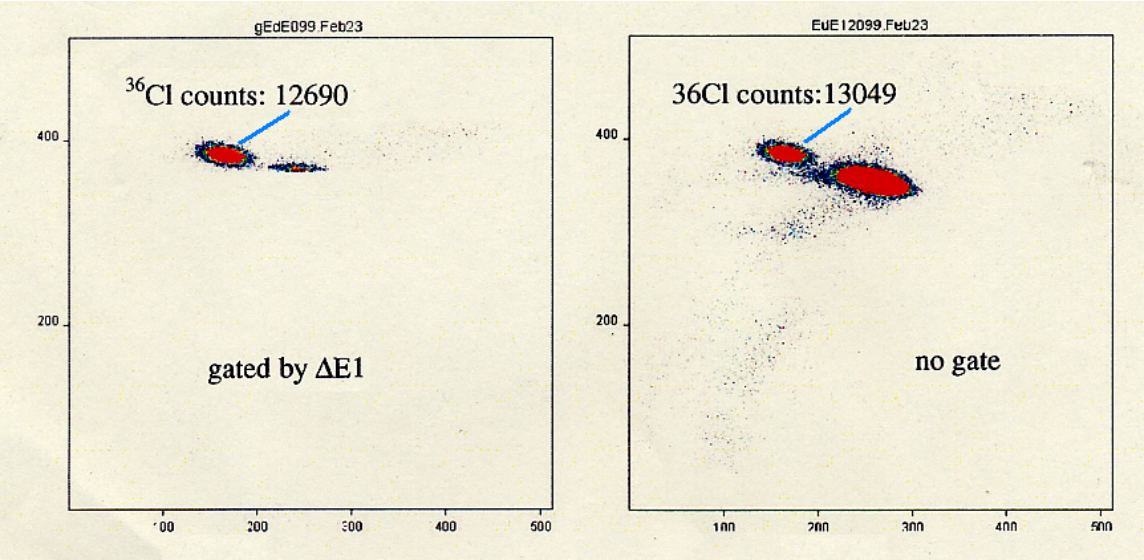

Fig. 4 Comparison of the influences of ^{36}S background on the ^{36}Cl yield with and without gate operation by ΔE_1 signal.

4.3 An environmental study with ^{36}Cl contents in the soils from many places in Japan

T. Matsuhiro, R. Seki, Y. Nagashima, K. Sasa, T. Takahashi, Y. Tosaki, He Ming[1], K. Sueki, K. Bessho, H. Matsumura, T. Miura

In our previous measurements of the ^{36}Cl contents in the several soils sampled at around Tokai-village, we could demonstrate the ratios of ^{36}Cl to Cl of the Tokai soils are 10 to 100 times larger than the ratios of Tsukuba soils. At that moment, we regarded Tsukuba soils might be the background samples because there are no nuclear facilities in the circumference of Tsukuba city. This estimation is, however, only speculation.

In order to confirm the results of Tokai village, both of an average and a fluctuation of ^{36}Cl contents in the soils of Japan are essentially important information. So, this year, we started the sampling of soils in Japan and commenced the measurements of ^{36}Cl contents in them. The soils in outer most layer were only sampled because radioisotope fallout in the atmosphere reaches first to the soils on the earth surface. Sampling points are carefully selected. An agricultural land, farm, creation land, reclamation land, and well-maintained places were counted out. The places in which there are no human activities have been selected. The back yard of a shrine was one of a nice candidate. Fig. 1 shows the sampling places in Japan. The sampling points were widely scattered from northern part of Japan, such as Hokkaido, to southern part of Japan like Nagasaki. The ratios ^{36}Cl : Cl are summarized in the Fig. 1. The average ratio of ^{36}Cl to Cl derived from ^{36}Cl AMS measurements of 23 samples corrected from 14 places in Japan is $(4.7 \pm 3.6) \times 10^{-13}$. The background ratios of 13 places fall within the order of 10^{-13}, but the Batoucho Nasu Tochigi gives 10^{-12} order of ratio. The origin why Batouchou gives so large ratio is not clear now.

Adding to the measurements of ^{36}Cl background, it is very interesting to compare the results of Tokai village with the results of the ^{36}Cl contents in the soils sampled in the vicinity of another nuclear facilities. Two big nuclear power plants are in Fukushima and total 10 BWRs are operated stationary for more than 30 years. We chose these sites for the comparison study. Total 21 places were selected as the sampling points and are summarized in Fig. 2 together with the ratio of ^{36}Cl to Cl. The average ratio of ^{36}Cl to Cl derived from ^{36}Cl AMS measurements of 21 places is $(4.6 \pm 2.7) \times 10^{-13}$. This ratio has no difference from the average background ratio of Japan. In contradiction to the results of Tokai village, it is obvious that there is no radioisotope leakage to the environment from the Fukushima nuclear power facilities.

Fig. 3 shows the chemical procedures for taking out Chlorine from the soil. After drying up, the soils is added 0.8M nitric acid and the mixture is separated into a solution and a residuum with a centrifugal separator. The solution contains Chlorine species. In order to improve the collection efficiency, the residuum is mixed into pure water and is repeated centrifugal separation again. The purpose of ammonium addition in the second step is to separate the metal such as Fe and Al. the metals are separated

[1] Present address China Institute of Atomic Energy, Beijing, China

from Chlorine with another centrifugal separation. The solution is concentrated to about 10ml by heating up. Then, the condensed solution is changed to acidity with concentrated nitric acid. As final step, In order to take Chlorine out as a silver chloride, 0.25M silver nitrate is added into the condensed solution. In average, about 10mg of Silver chloride can be collected from about 100g of soils with this procedure.

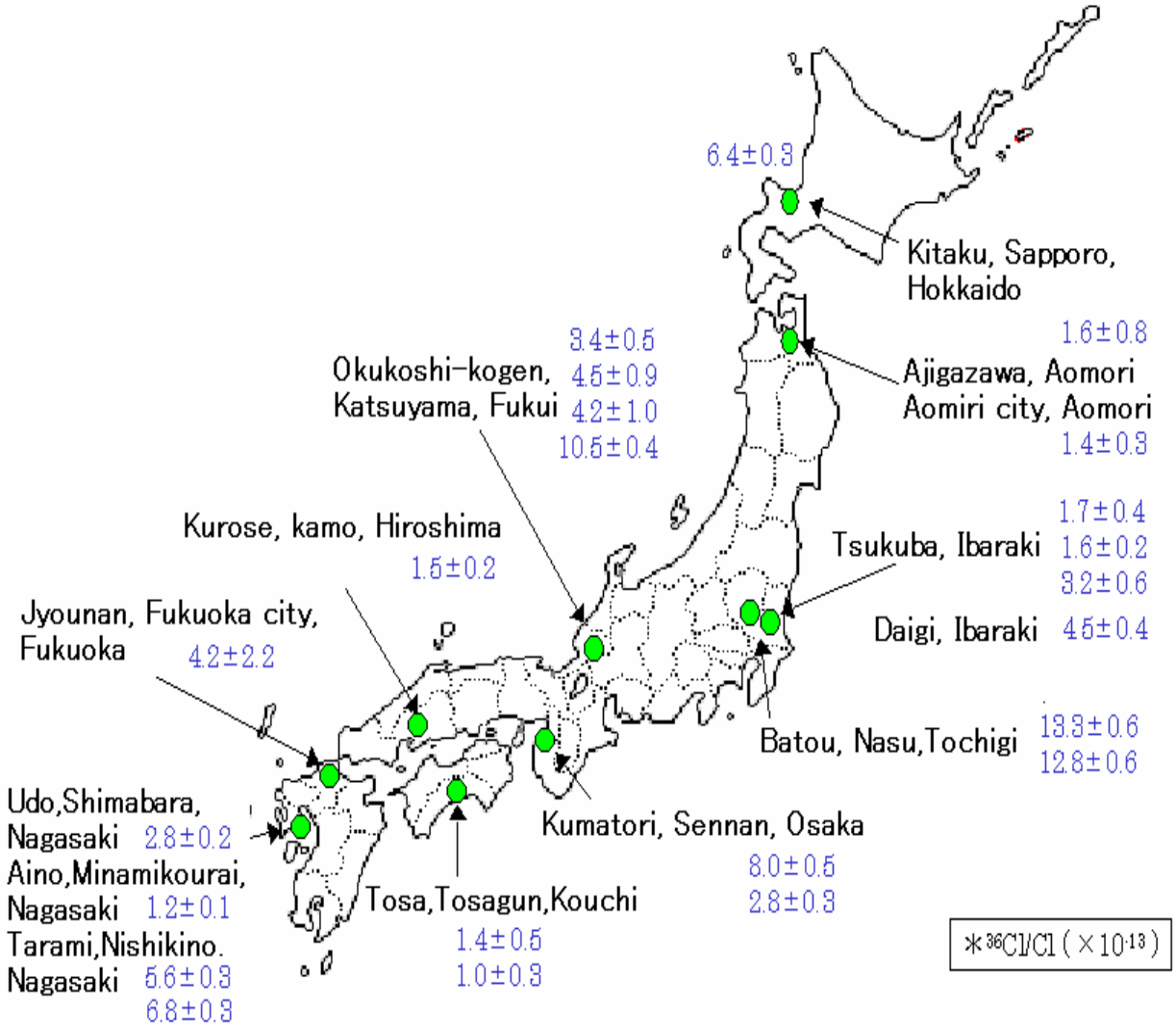

Fig. 1 ^{36}Cl background map. The backgrounds are expressed as a ratio of ^{36}Cl to Cl.

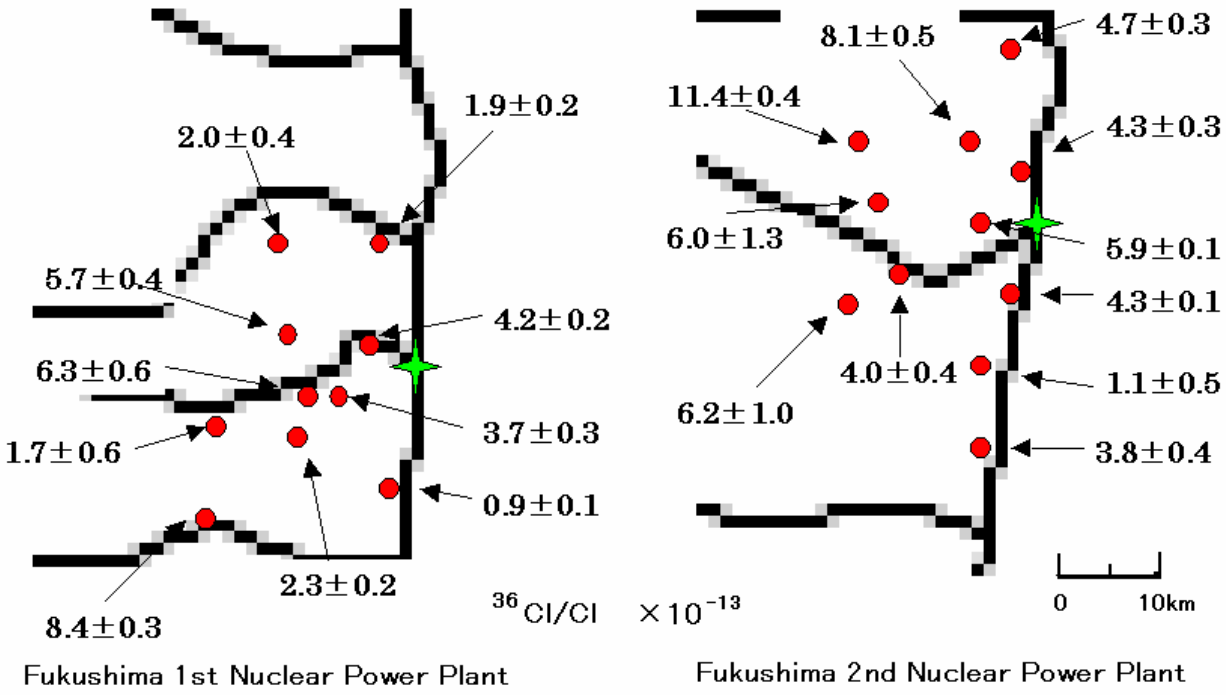

Fig. 2 The ratios of ^{36}Cl to Cl. The 6 BWRs are running in Fukushima 1st nuclear power plant and 4 BWRs are working in Fukushima 2nd nuclear power plant.

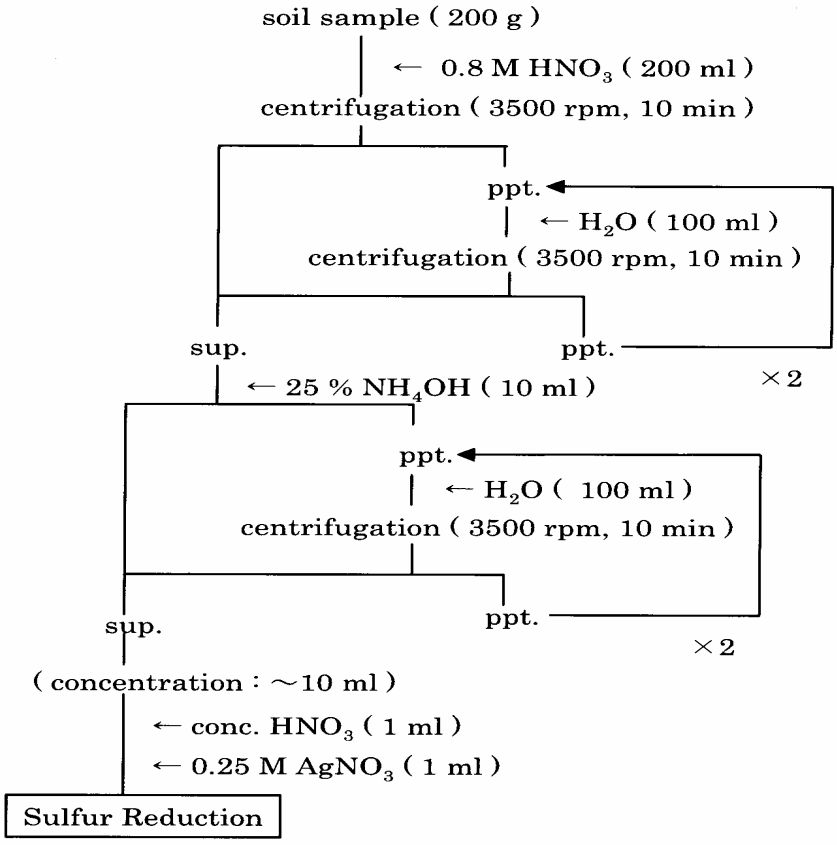

Fig. 3 Sample preparation scheme. Cl contents in soil are extracted as Silver chlorine.

4.4 Application of ^{36}Cl as a tracer in groundwater hydrology

Y. Tosaki, N. Tase, Y. Nagashima, R. Seki, T. Matsuhiro, T. Takahashi, K. Sasa, M. He, K. Sueki, T. Miura[1], K. Bessho[1] and H. Matsumura[1]

For the continuous use of groundwater resources, the knowledge of groundwater residence time plays very important role. Tritium (^{3}H) is one of the useful environmental tracers in groundwater study because its fallout rates had a peak caused by nuclear bomb tests conducted during the 1950s and 1960s. Due to the short half life (12.43 years), however, the ^{3}H bomb peak has been attenuated recently through radioactive decay. Hence, the groundwater tracer which can estimate the residence time of several decades is necessary in place of ^{3}H. Chlorine-36 (^{36}Cl) also had a bomb peak in its fallout rates mainly caused by oceanic nuclear bomb tests [1]. The ^{36}Cl has a half life of 301000 years which is much longer than that of ^{3}H, so the bomb peak has not been attenuated through radioactive decay. Therefore, the ^{36}Cl bomb peak can be a tracer in groundwater study. The objectives of this study are to investigate whether the ^{36}Cl bomb peak could be used as a tracer in groundwater and to explain the relation between the distributions of ^{36}Cl in groundwater and the residence time of groundwater.

Some groundwater samples were collected from observation wells at Tsukuba Upland, Ibaraki (Fig. 2). Site 1 is the experimental field at the Terrestrial Environment Research Center, University of Tsukuba. Site 2 is located at the northeastern part of Tsukuba Upland. Detail of Site 2 is described in Fig. 3.

Collected Groundwater samples were prepared as AgCl (Fig. 1). The ^{36}Cl/Cl ratios of the groundwater samples were measured by the AMS at the Tandem Accelerator Center, University of Tsukuba.

The results of ^{36}Cl measurements of groundwater samples are shown in Fig. 4-6. The results demonstrate that ^{36}Cl/Cl ratios of deep groundwater were somehow higher than those of shallow one. It suggests that the ^{36}Cl produced by oceanic nuclear bomb tests during the late 1950s still remains in deep groundwater. The results of this study indicate that the ^{36}Cl bomb peak could be used as a tracer in groundwater.

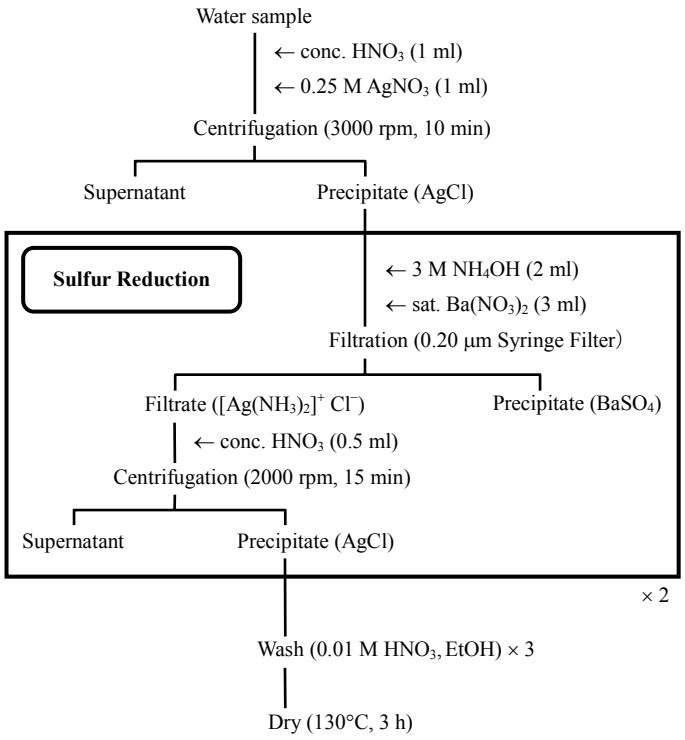

Fig. 1. Sample preparation for ^{36}Cl AMS measurement.

Reference

[1] H.-A. Synal, J. Beer, G. Bonani, M. Suter and W. Wolfli, Nucl. Instr. Meth. B52(1990)483-488.

[1] Radiation Science Center, High Energy Accelerator Research Organization

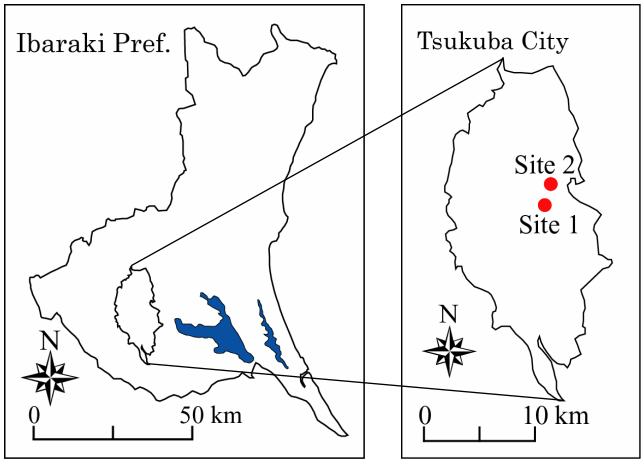

Fig. 2. Location of sampling sites.

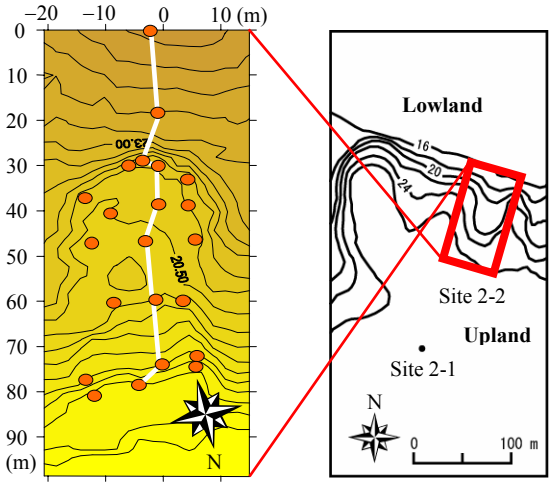

Fig. 3. Detail of Site 2.

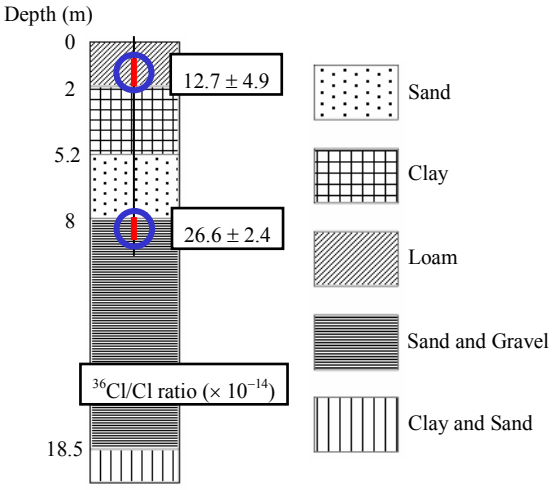

Fig. 4. ^{36}Cl/Cl ratios of groundwater at Site 1.

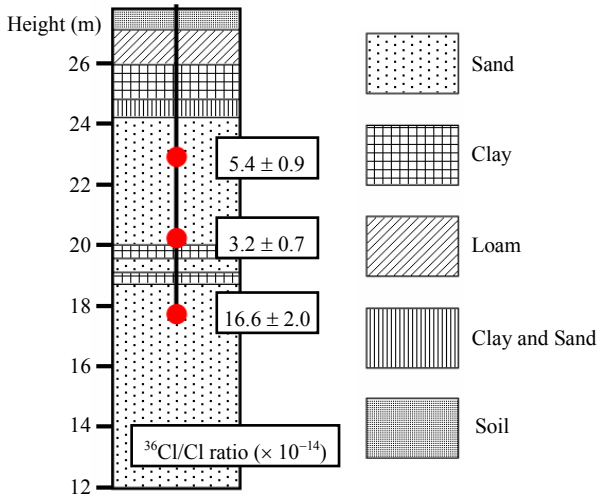

Fig. 5. ^{36}Cl/Cl ratios of groundwater at Site 2-1.

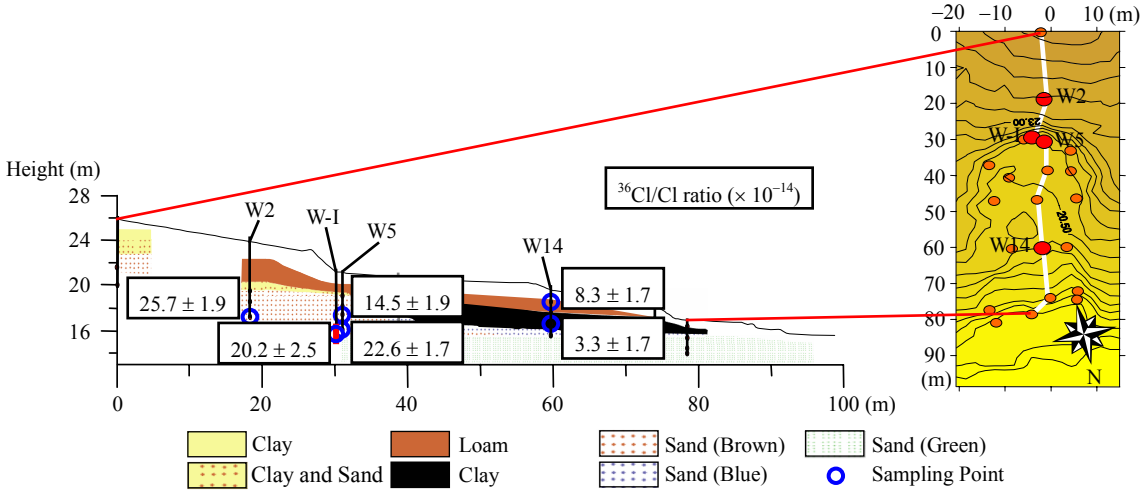

Fig. 6. ^{36}Cl/Cl ratios of groundwater at Site 2-2.

4.5 AMS measurement of ^{36}Cl in shielding concrete of various accelerator facilities

K. Bessho[1], H. Matsumura[1], T. Miura[1], Q. Wang[1], K. Masumoto[1], T. Matsuhiro, Y. Nagashima, R. Seki, T. Takahashi, K. Sasa and K. Sueki

At the accelerator facilities, shielding concrete and concrete walls around beam lines are exposed to secondary particles during machine operation, and various radionuclides are produced and accumulated in them. Quantitative evaluation of radionuclides induced in the shielding concrete is important for radioactive waste management in reconstruction or decommissioning of accelerator facilities. Most of the main radionuclides can be directly determined by a Ge detector for γ-emitters and a liquid scintillation counter for β-emitters such as ^{3}H, respectively[1]. On the other hand, long-lived ^{36}Cl can be measured only by accelerator mass spectrometry (AMS) because of its high detection sensitivity to ^{36}Cl. Last year, our group developed the suitable sample preparation for AMS of ^{36}Cl in the concrete of accelerator buildings and successfully applied for three kinds of accelerator facilities[2]. In this year, accuracy and reproducibility of the method were reexamined, and concrete samples collected at other accelerator facilities were analyzed.

The AMS system constructed in the 12UD tandem accelerator of UTTAC has been applied for ^{36}Cl analysis in soil and concrete samples related to Hiroshima atomic bomb, JCO critical accident, and other environmental samples[3,4]. The UTTAC ^{36}Cl AMS system is suited for the ^{36}Cl / ^{35}Cl ratio in the range 10^{-10} - 10^{-13}, while the ^{36}Cl / ^{35}Cl ratios in the above samples are in the range 10^{-12} - 10^{-13}, so the AgCl targets for AMS can be directly prepared by the extraction of Cl from concrete and soil samples. On the other hand, the ^{36}Cl / ^{35}Cl ratios in shielding concrete exceed 10^{-9} and are too high for applying AMS. Therefore the following procedure was developed. Chlorine in concrete samples was partially extracted into dilute nitric acid by heating in a tightly closed vessel. After the concentration of Cl extracted from sample was determined with an ion chromatography, the ^{36}Cl / ^{35}Cl ratio of Cl was diluted by adding a suitable amount of NaCl solution, in which ^{36}Cl / ^{35}Cl ratio was less than 10^{-13}. Chlorine was precipitated as AgCl by adding $AgNO_3$ solution under the acidic condition. The target preparation scheme including dilution steps was described in detail in the pervious report[2]. Amounts of concrete samples are 1 - 5 g when ^{36}Cl / ^{35}Cl ratios in samples are higher than 10^{-10}.

Validity of the sample preparation was evaluated by comparing the ^{36}Cl / ^{35}Cl ratios obtained at different dilution factors. **Table 1** shows examples of the ^{36}Cl / ^{35}Cl ratios determined by AMS measurements and the calculated original ratios in concrete samples. Samples No. 1 - 4 were collected from various accelerator facilities. For sample No. 1, we prepared two kinds of AgCl targets which are with or without dilution after Cl extraction. The ^{36}Cl / ^{35}Cl ratio of the diluted sample was in agreement with the ratio of the sample without dilution. For sample No. 2, AMS results of three kinds of dilution factors gave agreed results of the original ^{36}Cl / ^{35}Cl ratios. Similar results were obtained for sample No.

[1] Radiation Science Center, High Energy Accelerator Research Organization

3 and No.4. All of these results prove accuracy and reproducibility of this procedure.

In this year, concrete samples were obtained at 1.3 GeV electron synchrotron (Tanashi Branch, High Energy Accelerator Research Organization), AVF cyclotron and ring cyclotron (Research Center for Nuclear Physics, Osaka University). The depth profiles of ^{36}Cl / ^{35}Cl ratios in these concrete samples were analyzed. Other radionuclides were also measured with a Ge detector or a liquid scintillation counter.

Table 1 Examples of the ^{36}Cl / ^{35}Cl ratios determined by AMS measurements and the calculated original ratios in concrete samples

Sample	Dilution factor	$^{36}Cl/^{35}Cl$	
		AMS measurement	Calculated original ratio
No.1	1	$(7.46 \pm 0.59) \times 10^{-11}$	$(7.46 \pm 0.59) \times 10^{-11}$
	33.5	$(2.36 \pm 0.13) \times 10^{-12}$	$(7.90 \pm 0.44) \times 10^{-11}$
No.2	60	$(5.43 \pm 0.19) \times 10^{-12}$	$(3.26 \pm 0.11) \times 10^{-10}$
	75	$(4.60 \pm 0.28) \times 10^{-12}$	$(3.43 \pm 0.21) \times 10^{-10}$
	83	$(3.99 \pm 0.35) \times 10^{-12}$	$(3.30 \pm 0.29) \times 10^{-10}$
No.3	134	$(9.51 \pm 0.42) \times 10^{-12}$	$(1.27 \pm 0.06) \times 10^{-9}$
	192	$(7.16 \pm 0.63) \times 10^{-12}$	$(1.37 \pm 0.12) \times 10^{-9}$
No.4	37.4	$(4.02 \pm 0.14) \times 10^{-11}$	$(1.50 \pm 0.05) \times 10^{-9}$
	331	$(4.86 \pm 0.22) \times 10^{-12}$	$(1.61 \pm 0.07) \times 10^{-9}$

Fig. 1 shows the depth profiles of ^{36}Cl / ^{35}Cl ratios together with the specific radioactivities of ^{152}Eu, ^{60}Co, ^{3}H, ^{22}Na and ^{54}Mn in the shielding concrete of the ring cyclotron. The maximum ^{36}Cl / ^{35}Cl ratio was observed at about 10 cm in depth from the surface, and the depth profile of ^{36}Cl / ^{35}Cl ratios was good agreement with those of ^{152}Eu ^{60}Co, and ^{3}H. These characteristics were common to the AVF cyclotron, the electron synchrotron and other accelerator facilities[2]. These results imply that ^{36}Cl formed in concrete of these accelerators is mainly formed by thermal neutron capture of ^{35}Cl. The ^{36}Cl / ^{35}Cl directly shows the specific activity and ^{36}Cl is a very long half-life nuclides. Therefore the ^{36}Cl / ^{35}Cl measurement is more suitable for the monitoring of cumulative thermal neutron fluence than the radioactivity measurement of ^{152}Eu and ^{60}Co.

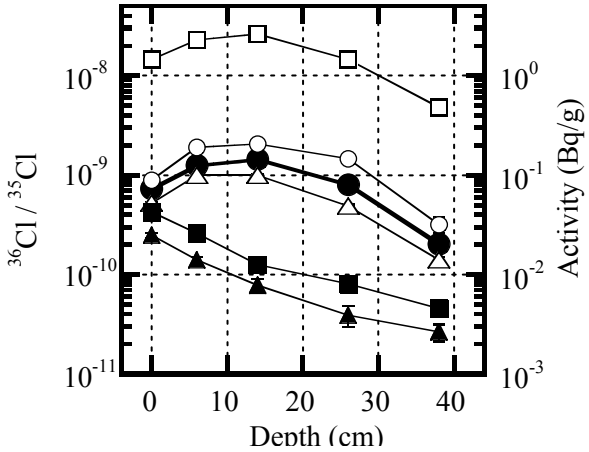

Fig. 1 Depth profiles of ^{36}Cl / ^{35}Cl ratios(● and specific radioactivities of ^{152}Eu (○), ^{60}Co (△), ^{3}H (□), ^{22}Na (■) and ^{54}Mn (▲) induced in the shielding concrete of ring cyclotron (Research Center for Nuclear Physics, Osaka University)

References

[1] T. Miura et al., J. Nucl. Sci. Technol.,Sup.1 (2000)183

[2] K. Bessho et al., UTTAC-71 (2002) 99

[3] Y. Nagashima et al., Nucl. Instr. Meth. B172(2000)129

[4] R. Seki et al., J. Radioanal. Nucl. Chem. 255(2003) 245

4.6 AMS measurement of the $^{14}N(^{16}O,\alpha)^{26}Al$ reaction at the near barrier energies

H. Ming[1], Y. Nagashima, K. Sasa, R. Seki, T. Matsuhiro, T. Takahashi, Y. Tosaki, and K. Sueki

The 1.809MeV γ-line due to the decay of ^{26}Al has been observed in the interstellar medium in 1980s. Since the ^{26}Al half-life (3×10^6 yr) is much shorter than the time-scale of the galactic evolution ($\sim10^9$ yr), the detection of this radioactivity shows that the nucleosynthesis is still active in our Galaxy. Many models have been proposed to explain the source of the 1.809MeV γ-ray, but the origin is still remaining as a mystery in astrophysics. The $^{14}N(^{16}O,\alpha)^{26}Al$ reaction might be one of the source of 1.809MeV γ-ray in the interstellar medium during the supernova explosion such as SNIa. Therefore, the $^{14}N(^{16}O,\alpha)^{26}Al$ reaction cross sections have been measured by using the prompt γ-ray detection method. However, Due to the small cross sections at low stellar temperatures (T_9=0.06~0.2) and resulting extremely low counting rate, there are no reliable data of this reaction at sub-barrier energy now.

Here, we report an AMS measurement as an alternative method for the determination of the $^{14}N(^{16}O,\alpha)^{26}Al$ reaction cross section. The high sensitivity of the AMS is very efficient for the detection of very rare element and allows the determination of radioisotope concentrations such as ^{26}Al at the level down to 10^{-15} of ^{26}Al to ^{27}Al ratio. The ^{26}Al elements have been created through $^{14}N(^{16}O,\alpha)^{26}Al$ reaction at three incident energies, Ec.m.=9.5, 7.9, and 6.6 MeV. The irradiation is performed at the tandem accelerator laboratory in the Peking University. TiN foil being evaporated on the high-purity Cu backing foil is used as a ^{14}N target. A 20μm thick Cu foil is selected as the backing foil and that is thick enough to catch not only ^{16}O beams but also ^{26}Al and ^{14}N recoils. The thickness of the evaporated TiN is comparably thick and its thickness is precisely estimated by comparing the weight of before and after the evaporation. The total amount of ^{16}O dose is also carefully measured with an ORTEC current integrator, see Table 1. Fig. 1 shows the arrangement of the TiN target in an insulated chamber with an electrode for electron suppress. Thus, the chamber is functioned not only as a target chamber but also as a Farady-cup for the measurement of the total dose of the ^{16}O impinging beam. The TiN target with Cu backing is tightly fixed to a bottom of the chamber in order to keep a nice heat conductivity. To prevent an extremely rise of the target temperature, the chamber is continuously cooled down by cooling water and the target is kept to low temperature during the one day bombardment with 3μA ^{16}O accelerated beam. Both size and shape of the ^{16}O beam on the target was monitored by exchange the target housing for a quartz housing. This monitoring has been repeated every ~3 hours in order to confirm the ^{16}O beam qualities. The beam was very stable and there was no observation in beam deterioration. Accounting into both the sensitivity of ^{26}Al-AMS measurements, $^{26}Al/^{27}Al=\sim10^{-15}$, and the smallest required amount of ^{27}Al carrier, ~2mg, $\sim10^6$ atoms of ^{26}Al must be produced in the bombardment. So, in the case of the lowest bombarding energy (6.6MeV), the target was irradiated for 3 days by ~ 2μA ^{16}O beam.

The procedures for extracting the ^{26}Al elements from the TiN target material are followings. First,

[1] Present address: China Institute of Atomic Energy

both of the TiN target and ^{27}Al carrier that is measured precisely are dissolved into nitrohydrochloric acid solution, HNO_3 + HCl. Then, the solution is diluted to be 0.1M and condensed ammonium regent is mixed into the solution little by little in order to precipitate Al element as an aluminum hydroxide, AlOH. The centrifugation and washing the precipitate are repeated several times. At this step, all most of contaminants such as Cu are separated out from the AlOH precipitate. Finally, the AlOH precipitate are dried and then it is changed to Al_2O_3 by heating up to 1000°C for two hours.

^{26}Al contents in three Al_2O_3 samples, which are produced through $^{14}N + {}^{16}O$ fusion reactions, are measured by means of AMS. The Al_2O_3 samples are mixed with powder of pure silver and an amount of enriched ^{26}MgO regent. The purposes of the silver and ^{26}MgO addition are to keep an electronic conductivity and to create $^{26}MgO^-$ control beam for the tandem voltage stability, respectively. Both $^{26}Al^{7+}$ and $^{26}Mg^{7+}$ with 78MeV energy are selected by the 90° analyzing magnet and are transported into the 2nd charge exchange foil. After passing through the foil, $^{26}Al^{13+}$ fully stripped ions are selected by the following energy and momentum selectors and are forwarded to the ΔE-E ionization counter in the AMS beam line. We measure the standard samples before and after sample measurement, with one set consisting of three measurements: measurement of standard sample - measurement of a sample - measurement of a standard sample. We conduct four sets of measurements for each sample to obtain average value. Though dependent on the ^{26}Al concentration of the samples, one set of measurement require 40 - 60 min. The measurements are still undergoing.

Bombarding energy ($E_{c.m.}$, MeV)	Dose of ^{16}O beam (C)	TiN thickness ($\mu g/cm^2$)	^{27}Al carrier added (mg)
9.5	6.47×10^{-3}	317	5.8
7.9	3.63×10^{-2}	260	3.9
6.6	4.72×10^{-1}	280	2.8

Table 1 List of samples. TiN targets are evaporated on the pure Cu backing foils. The bombarded target together with an Al carrier is dissolved into dense solution of HNO_3 and HCl mixture. The chemical pure Al regent is used as an Al carrier.

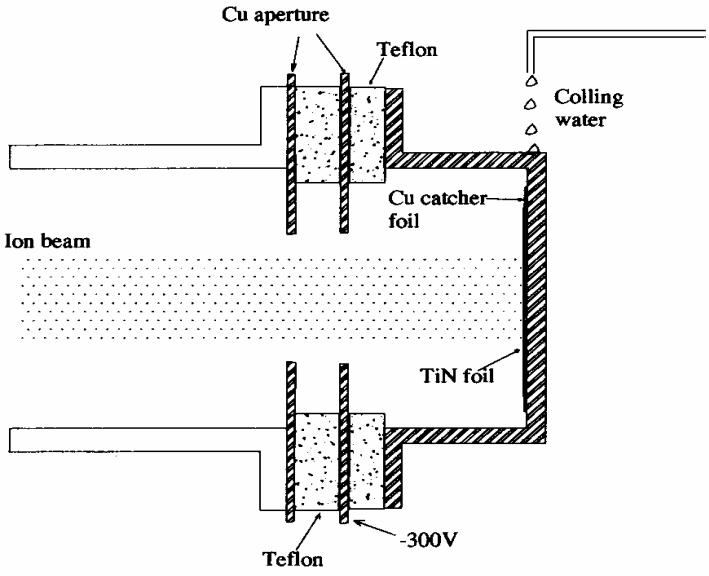

Fig .1 Cross section of the bombarding chamber. TiN foil on the Cu backing is set on the bottom of the chamber. The chamber is cooled continuously with the drop of water.

4.7 Qualitative measurement of hydrogen depth profile by using ERCS for melt inclusions in quartz crystal

T. Komatsubara, K. Sasa, S. Ishii, Y. Yamato, K. Miyakawa, T. Kurosawa, K. Furuno

Proton-proton elastic recoil coincidence spectrometry (ERCS) is powerful method to analyze hydrogen content[1]. This analysis is quite convenient and non-destructive. It is also possible to deduce depth profile of hydrogen content. New project by using this spectrometry has been started at Tandem Accelerator Center, University of Tsukuba, combined with the micro beam system[2, 3]. In this report, our recent developments for the hydrogen analysis in melt inclusions of mineral samples will be described.

For the analysis of the mineral samples, positioning of the irradiation point is quite important. Typical size of the quartz sample is about 3 mm in diameter. The thickness of the sample is 0.2 mm or less. As our object of the analysis, the quartz samples contain several melt inclusions that size are in range from 30 - 300 μ m. In the micro beam irradiation system, micro scope has been installed to observe the irradiation point. For more clear view of the target, two thin mylar films were used to hold the samples in vacuum. Aluminium foils of 5 mm in thickness were used to shade particle detectors, as the observation is possible during the irradiation measurements.

Since the mylar films contain hydrogen, the scattering yields from these supporting films are also available for the calibration. Scattering yield Y [counts] can be calculated as

$$Y = 3.759 \, \frac{d\sigma}{d\Omega} \, \Omega \, Q \, w$$

where difference cross section is denoted by dσ/dΩ in mb/sr, solid angle of detector is Ω sr, and irradiation charge is Q in nano Coulomb. Target thickness is given by w μg/cm^2[H] as the corresponding hydrogen weight density. Weight ratio of the contained hydrogen in the mylar film was measured to be 4.49 $\pm$ 0.03 wt.%[H] by using CHN trace element analysis. Thickness of the films is measured to be 348 $\pm$ 3 μg/cm^2. The mylar films were purchased from Chemplex Industries Inc. and nominally described as 2.5 μ m in thickness. This hydrogen density corresponds to 15.6 $\pm$ 0.2 μg/cm^2[H] as the hydrogen target thickness. Scattering yield from one mylar film is measured to be 2722 $\pm$ 17 counts for 50 nano Coulomb irradiation. Solid angle of the coincidence system is calculated to be 0.0156 sr which is defined by the detector slits of ϕ 5.4 in diameter at 38 mm from the scattering center. The differential cross section is deduced to be 59.5 $\pm$ 0.7 mb/sr in laboratory frame which corresponds to 21.0 $\pm$ 0.3 mb/sr in center of mass. This measured value is rather consistent to singles measurement as dσ/dΩ = 24.6 $\pm$ 0.3 mb/sr at 19.8 MeV [4].

If the irradiation power is strong, some hydrogen could be emitted out from the target or the supporting mylar films. If the irradiation damage occurs, power density should be reduced by decreasing beam current. In Fig. 1a, the variation of the scattering yields is shown when the same position of the mylar film was irradiated by 130 pA of ϕ 30 μm micro beam. This figure shows slight decrease of the scattering yield. The reduction in a 50 n Coulomb irradiation measurement can be estimated as 1.2 %. Kapton film shows more persistent than the mylar film shown in the Fig. 1b. However, yellow color of the kapton film gives worse transparency than mylar. We have chosen mylar films as the supporting films for more clear micro scope view.

As reported in the previous annual report a solid angle for the coincidence experiment strongly depends on the irradiation position. With simple assumption, the solid angle depending on the displacement along to beam direction (z axis) can be calculated as following formula.

$$\Omega = \frac{2\theta r^2 - |z|\sqrt{2r^2 - |z|^2}}{d^2}$$

$$\theta = \mathrm{Arccos}\frac{|z|}{\sqrt{2}r}$$

where r denotes a radius of collimators in front of the detectors and d is a distance between the collimators and a target. These formula are identical to the previous report.

For more detail dependence on the displacements, computer simulation was performed. As the result of the calculation, detection solid angle with coincidence condition exhibits strong dependence on y direction and less sensitive to x direction, as shown in Fig. 2(a), (b) and (c). When displacements occur for two directions simultaneously, solid angle varies smoothly at Z=0 position as shown in Fig. 2(d) and (e). In these calculations, the present geometry of ϕ 5.4 mm slits at 38 mm from an irradiation point is assumed.

For the ERCS method, a measured spectrum of sum energy of two protons implies depth profile of hydrogen, because stopping powers for the scattered protons are twice higher than that of incident proton. Therefore, the measured sum energy spectrum can be modified to be depth profile of hydrogen. If one consider to reconstruct the hydrogen profile from the measured sum energy spectrum, there are several effects which should be taken into account; those are stopping power, secondary scattering, multiple scattering, lateral and longitudinal straggling, variation of material, and displacement.

In order to evaluate the effect of the stopping power, computer simulation were performed. Calculated sum energy spectra of scattered particles which are degraded by the stopping power are shown in Fig. 3(a). The data of stopping power is referred from SRIM table. Targets are assumed to be SiO_2 with a homogeneous hydrogen content. Thickness of the SiO_2 plates are 100, 200, 300, and 400 μm. The sum energy depends on the position of the scattering in depth, however, the dependence is not linear. For the reconstruction of the constant hydrogen density, a quadrant term is introduced to convert a channel x as follows;

$$x' = C_0 + C_1 \times (x - C_0) + C_2 \times (x - C_0)^2$$

where x' is a new channel number to indicate depth position. By using the two parameters as $C_1 = 1.0$ and $C_2 = 9.56 \times 10^{-4}$, modified spectra show rather constant hydrogen densities as shown in Fig. 3(b).

As a realistic example of the data, a measured sum spectrum of a multi-layer sample is shown in Fig. 4(a). At first, channel number is modified as described above as shown in Fig. 4(b). For the compensation of the exponential decrease by the secondary scattering, measured counts are multiplied as

$$Y'(x') = Y(x') \times e^{\mu(C_0 - x')}$$

where the parameter μ can be obtained from scattering yields and peak positions of two mylar films on the surfaces. In Fig. 4(c) the modified spectrum is shown as hydrogen profile.

References

[1] B.L. Cohen, C.L. Fink, J.H. Degnan, J. Appl. Phys., **43**, 19 (1972).

[2] K. Sasa, H. Oshima, Y. Yamato, T. Komatsubara, T. Katabuchi, K. Shima, K. Furuno, M. Kurosawa, N. Yanagisawa, Nucl. Inst. Meth. **B190**, 287 (2002).

[3] K. Furuno, T. Komatsubara, K. Sasa, H. Oshima, Y. Yamato, S. Ishii, H. Kimura, M. Kurosawa, Nucl. Inst. Meth. **B210**, 459 (2003).

[4] J.W. Burkig, J.R. Richardson, G.E. Schrank, Phys. Rev. **113**, 290 (1959).

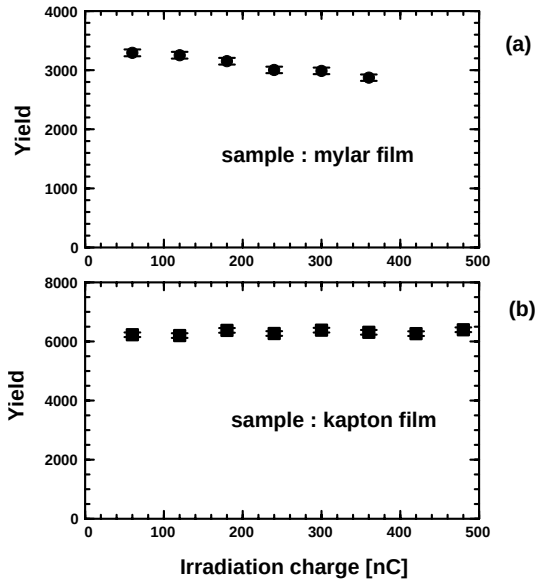

Fig. 1(a) Scattering yields from the same position of mylar film. By repeating measurements, slightly decrease of the yield was observed. Fig. 1(b) Repeated measurements with kapton film. The kapton film shows more persistence.

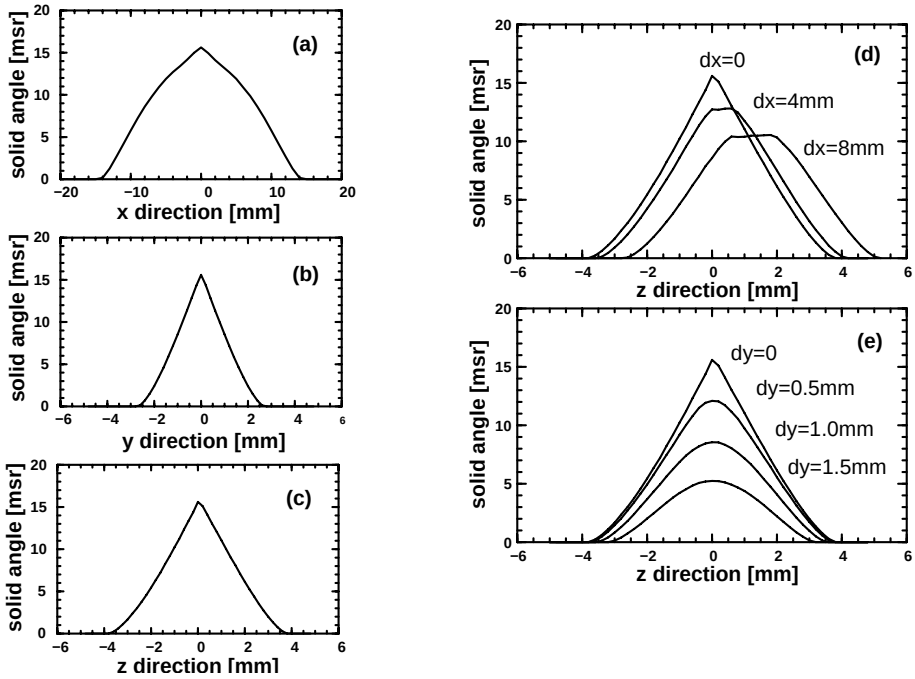

Fig. 2. Calculated solid angles by changing irradiation position. Figs. 2(a), 2(b) and 2(c) show calculated solid angles depending on the position moving along to x-, y- and x- directions, respectively. When displacements occur for x and z directions at same time, solid angle is not maximum at dz = 0 position as shown in Fig. 2(d). Combination of the displacement for y- and z- directions show more serious reduction of the solid angle as shown in Fig. 2(e).

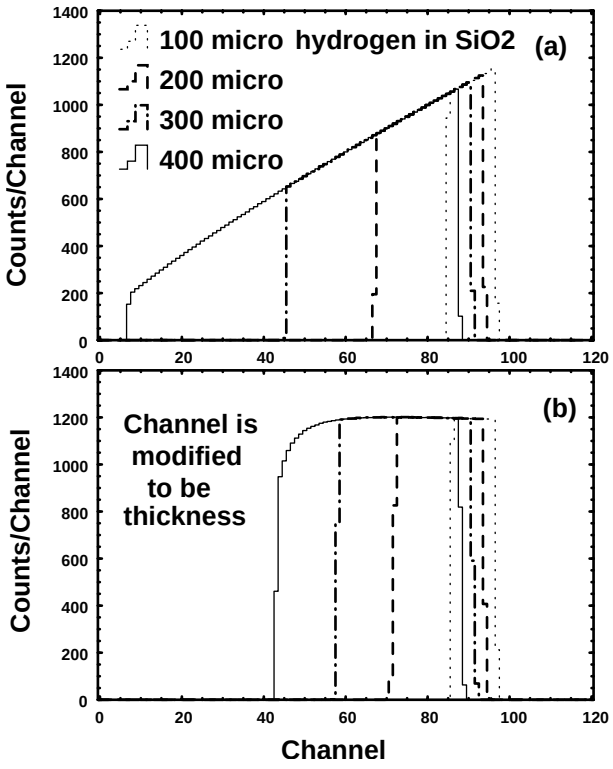

Fig. 3(a) Simulated spectra of sum energy for the proton-proton coincidence measurement by using calculation of stopping power for incident and scattered protons. Hydrogen density is assumed to be constant in SiO_2 of 100, 200, 300 and 400 μ m in thickness. Channel number is equal to be 5 $\times$ sum energy in MeV. Fig. 3(b) is results of the modification from the sum energy spectra. A Method of the analysis is described in text.

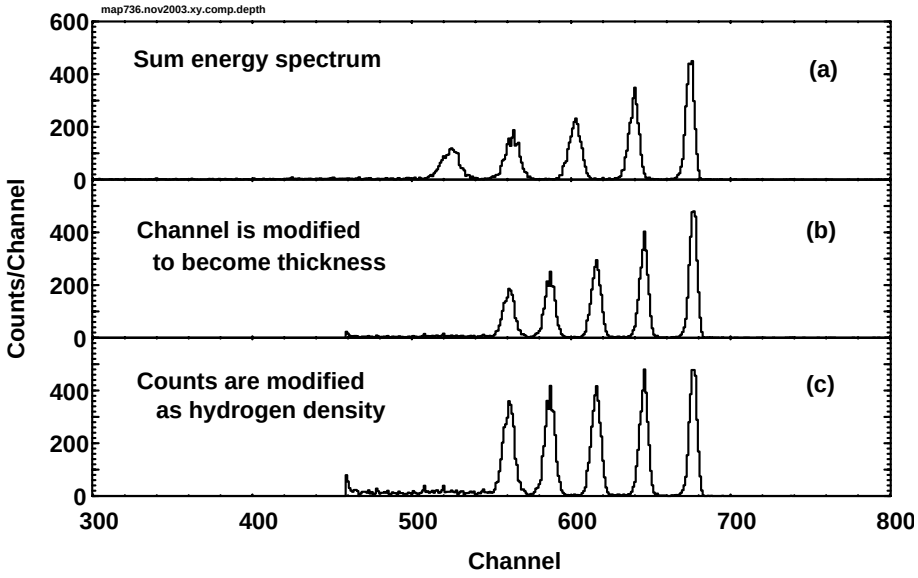

Fig. 4(a) Measured spectrum for a stacked target which consists five mylar of 2.5 μ m in thickness and SiO_2 glass of 50 μ m. Fig. 4(b) shows the result of the modification described in text. The modified channel number can correspond depth position. Fig. 4(c) is the result of correction for exponential decay of the scattering yield reduced by the secondary scattering.

4.8 High energy gamma rays from radiative capture reactions

T. Komatsubara, M. Yamaguchi, A. Maki[1], T. Haruyama[1], T. Iwamoto[2], S. Mihara[2], H. Nishiguchi[2], Y. Hisamatsu [2], W. Ootani[2], K. Ozone[2], R. Sawada[2], T. Mitsuhashi[2]

[1] High Energy Accelerator Research Organization

[2] International Center for Elementary Particle Physics, University of Tokyo

A radiative capture process is known as a gamma-ray transition from a unbound scattering state to a bound state. This reaction can be considered as a two-step process where a intermediate state is excited by the nuclear reaction at first and de-excitation process follows by the electromagnetic interaction [1]. However reaction cross section of this process is rather small, energy of the emitted gamma rays can be reached to be more than 20 MeV. New project with large xenon scintillation detector system has been started to seek $\mu \rightarrow e\gamma$ decay mode emitting a 52.6 MeV photon as collaboration with PSI and KEK[3]. For the development of the high energy gamma ray detectors, high energy photon sources are desired for the precise calibration.

A nuclear reaction of ^{11}B(p,γ) 12C is considered for the test experiment providing a high energy gamma ray by the radiative capture reaction. A gamma-transition was reported from E^* = 22.6 MeV with $\Gamma_{c.m.}$ = 3.2 MeV as a giant resonance in the ^{12}C[4]. However, better resolution of 380keV (FWHM) was reported by using thin target of 400 μg/cm^2 in thickness [2]. Reaction cross sections was reported as $d\sigma/d\Omega(90^\circ) = 13.1 \pm 1.3$ μb/sr at the bombarding energy of 7.2 MeV for the proton beam [4].

The test experiment has been performed by the proton beam irradiated on some compound material targets including boron powder. Bombarding energy of the proton beam is 7.2 MeV. Gamma ray spectra were measured by a 5' $\times$ 5' NaI scintillator surrounded by four veto counters to eliminate back ground of cosmic rays. Fig. 1 shows the measured spectrum in which several high energy peaks appear around 20 MeV. However, rather similar spectrum is observed for another target without boron powder shown in Fig. 2. The origin of these peaks are under consideration.

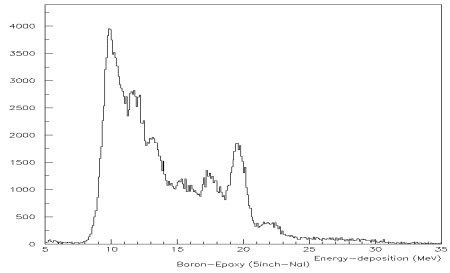

Fig. 1. Gamma-ray spectrum obtained by the irradiation of 7.2 MeV proton beam on the compound material including boron powder. Gamma-rays were measured by by 5' $\times$ 5' NaI scintillation detector surrounded by four veto counters.

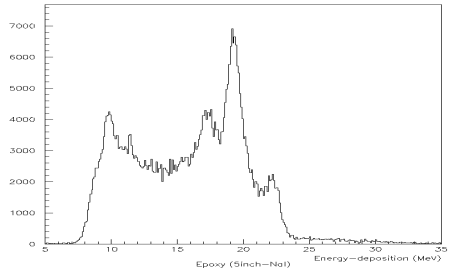

Fig. 2. Gamma-ray spectrum obtained by another target which does not contain boron.

References

[1] H. Ejiri and M.J.A de Voigt, "Gamma-ray and electron spectroscopy in nuclear physics", **Oxford science publications**, Clarendon Press, Oxford, (1989).

[2] A. H åkansson, J. Blomgren, S. Crona, A. Likar, A. Lindholm, L. Nilsson, N. Olsson, R. Zorro, Nucl. Inst. Meth. **A273**, 211, (1988).

[3] T. Doke, T. Haruyama, T. Ishida, A. Maki, T. Mashimo, S. Mihara, T. Mitsuhashi, T. Mori, H. Nishiguchi, W. Ootani, S. Orito, K. Ozone, R. Sawada, S. Suzuki, K. Terasawa, M. Yamashita, J. Yashima, T. Yoshimura, Nucl. Inst. Meth. **A505**,199, (2003).

[4] F. Ajzenberg-Selove, Nucl. Phys. **A433**, 1, (1985).

5. LIST OF PUBLICATIONS

NUCLEAR PHYSICS – EXPERIMENT

M. Yamaguchi, K. Sawada, T. Katabuchi, N. Kawachi, N. Yoshimaru, K. Shiga and Y. Tagishi High-efficiency polarimeter for a secondary proton beam of 16-22 MeV Nucl. Inst. and Meth. **A 506**, 35-40, (2003).

H.Miyatake, H.Ueno, Y.Yamamoto, N.Aoi, K.Asahi, E.Ideguchi, M.Ishihara, H.Izumi, T.Kishida, T.Kubo, S.Mitsuoka, Y.Mizoi, M.Notani, H.Ogawa, A.Ozawa, M.Sasaki, T.Shimoda, T.Shirakura, N.Takahashi, S.Tanimoto, and K.Yoneda, Spin-parity assignments in $15C^*$ by a new method: β-delayed spectroscopy for a spin-polarized nucleus, Phys. Rev. **C 67**, 014306 (2003).

A.Ozawa, Y.Yamaguchi, M.Chiba, R.Kanungo, K.Kimura, S.Momota, T.Suda, T.Suzuki, I.Tanihata, T.Zheng S.Watanabe, T.Yamaguchi, and K.Yoshida, Search for ^{21}B, Phys. Rev. **C 67**, 014610 (2003).

A.A.Korsheninnikov, E.Yu.Nikolskii, E.A.Kuzmin, A.Ozawa, K.Morimoto, F.Tokanai R.Kanungo, I.Tanihata, N.K.Timofeyuk, M.S.Golovkov, A.S.Fomichev, A.M.Rodin, M.L.Chelnokov, G.M.Ter-Akopian, W.Mittig, P.Roussel-Chomaz, H.Savajols, E.Pollacco, A.A.Ogloblin, M.V.Zhukov, Experimental evidence for the Existence of ^{7}H and for a Specific Structure of ^{8}He, Phys. Rev. Let. **90**, 082501 (2003).

D.Cortina-Gil, J.Fernandez-Vazquez, F.Attallah, T.Baumann, J.Benlliure, M.J.G.Borge, L.V.Chulkov, C.Forssen, L.M.Fraile, H.Geissel, J.Gerl, K.Itahashi, R.Janik, B.Jonson, S.Karlsson, H.Lenske, S.Mandal, K.Markenroth, M.Meister, M.Mocko, G.Munzenberg, T.Ohtsubo, A.Ozawa, Yu.Parfenova, V.Pribora, A.Richter, K.Riisager, R.Schneider, H.Scheit, G.Schrieder, N.Shulgina, H.Simon, B.Sitar, A.Stolz, P.Strmen, K.Summerer, I.Szarka, S.Wan, H.Weick, M.Zhukov, Nuclear and Coulomb breakup of ^{8}B, Nucl. Phys. **A 720**, 3-19 (2003).

F.Schümann, F.Hammache, S.Typel, F.Uhlig, K.Sümmerer, I.Böttcher, D.Cortina, A.Förster, M.Gai, H.Geissel, U.Greife, N.Iwasa, P.Koczon, B.Kohlmeyer, R.Kulessa, H.Kumagai, N.Kurz, M.Menzel, T.Motobayashi, H.Oeshler, A.Ozawa, M.Ploskon, W.Prokopowicz, E.Schwab, P.Senger, F.Strieder, C.Sturm, Zhi-Yu Sun, G.Surowka, A.Wagner, and W.Walus, Coulomb Dissociation of 8B and the Low-Energy Cross Section of the ^{7}Be(p,γ)^{8}B Solar Fusion Reaction, Phys. Rev. Let., **90** 232501 (2003).

S.Nishimura, M.Kurata-Nishimura, K.Morimoto, Y.Nishi, A.Ozawa, T.Yamaguchi, T.Ohnishi, T.Zheng, M.Chiba, I.Tanihata, Systematic studies of scintillation detector with timing resolution of 10 ps for heavy ion beam, Nucl. Instr. Meth. **A 510**, 377-388 (2003).

T.Yamaguchi, T.Zheng A.Ozawa, M.Chiba, R.Kanungo, T.Kato, K.Katori, K.Morimoto, T.Ohnishi,

T.Suda, I.Tanihata, Y.Yamaguchi, A.Yoshida, K.Yoshida, H.Toki, N.Nakajima, Momentum distributions of ^{14}C and ^{15}C fragments from ^{16}C breakup, Nucl. Phys, **A 724** 3-13 (2003).

T.Baumann, H.Ikeda, M.Kurokawa, M.Miura, T.Nakamura, Y.Nishi, S.Nishimura, A.Ozawa, T.Sugimoto, I.Tanihata, M.Thoennessen, Using passive converters to enhance detection efficiency of 100-MeV neutrons, Nucl. Instr. and Meth. **A 505**, 25-28 (2003).

R.Kanungo, M.Chiba, S.Adhikari, D.Fang, N.Iwasa, K.Kimura, K.Maeda, S.Nishimura, Y.Ogawa, T.Ohnishi, A.Ozawa, C.Samanta, T.Suda, T.Suzuki, Q.Wang, C.Wu, Y.Yamaguchi, K.Yamada, A.Yoshidaa, T.Zheng, I.Tanihata, Possibility of a two-proton halo in ^{17}Ne, Phys, Lett. **B 571** 21-28 (2003).

L.S.Geng, H.Toki, A.Ozawa and J.Meng, Proton and neutron skins of light nuclei within the relativistic mean field theory, Nucl. Phys., **A 730**, 80-94 (2003).

C.Y. Xie, X.H. Zhou, Y. Zheng, Y.H. Zhang, Z. Liu, Z.G. Gan, T. Hayakawa, M. Oshima, T. Toh, T. Shizuma, J. Katakura, Y. Hatsukawa, M. Matsuda, H. Kusakari, M. Sugawara, K. Furuno, T. Komatsubara, Level structure of Tb-146, Eur. Phys. J. **A 19**, pp. 7-9 (2004).

C.B. Moon, T. Komatsubara, K. Furuno, Band structures in I-116, Nucl. Phys. **A 730**, pp.3-22 (2004).

Y.H.Zhang, M.Oshima, Y.Toh, X.H.Zhou, M.Koizumi, A.Osa, A.Kimura, Y.Hatsukawa, T.Morikawa, M.Nakamura, M.Sugawara, H.Kusakari, T.Komatsubara, K.Furuno, H.L.Wang, P.Luo, C.S.Wu, F.R.Xu, Rotational bands and signature inversion in odd-odd 172Re, Phys.Rev. **C 68**, 054313 (2003).

C.B. Moon, T. Komatsubara, T. Shizuma, Y. Sasaki, K. Furuno, C.S. Lee, Collective bands in odd-odd 118I, Nucl. Phys. **A728**, pp.350-364 (2003).

C.-B.Moon, T.Komatsubara, K.Furuno, A Dipole Band in 122Xe, Journal of the Korean Physical Society **43**, pp.574-577 (2003).

C.B. Moon, T. Komatsubara, K. Furuno, Collective bands in 115I, Journal of the Korean Physical Society **43**, pp.319-324 (2003).

Y.H. Zhang, F.R. Xu, J.J. He, Z. Liu, X.H. Zhou, Z.G. Gan, M. Oshima, T. Hayakawa, Y. Toh, T. Shizuma, J. Katakura, Y. Hatsukawa, M. Matsuda, H. Kusakari, M. Sugawara, K. Furuno, T. Komatsubara, T. Une, S.X. Wen, Z.M. Wang, High-spin states and signature inversion in odd-odd Au-182, Science in China Series G-Physics Astronomy **46**, pp.382-389 (2003).

Z. Liu, Y.H. Zhang, Y.J. Ma, Y. Sasaki, K. Yamada, H. Oshima, H. Yokose, M. Ishizuka, T. Komatsubara, K. Furuno, High-spin states of Sb-125: Particle-core excitation coupling, Science in China Series G-Physics Astronomy **46**, pp.390-397 (2003).

K. Sasa, K. Furuno, Y. Yamato, H. Ohshima, S. Ishii T. Komatsubara, M. Kurosawa, The Tsukuba high-energy nuclear microprobe for hydrogen analysis of mineral samples, Nucl. Instr. and Meth. **B210**, 48-53 (2003).

K Furuno, T. Komatsubara, K. Sasa, H. Ohshima, Y. Yamato, S. Ishii, H. Kimura, M. Kurosawa, Measurement of hydrogen concentration in thick mineral or rock samples, Nucl. Instr. and Meth. **B210**, 459-463 (2003).

K. Sasa, K. Shima, T. Komatsubara, H. Kudo, Applied research by the 12MV tandem accelerator and the 1MV tandetron accelerator, Genshikaku Kenkyu, **Vol.48**, No.5, 43-52 (2003).

HIGH ENERGY NUCLEAR PHYSICS

T. Abbott, Y. Miake, *et al.*, Further observations on midrapidity et distributions with aperture corrected scale, Phys. Rev. **C68** :034908, (2003).

M. Aizawa, S. Esumi, Y. Miake, *et al.*, PHENIX central arm particle id detectors, Nucl. Instrum. Meth. **A499** :508-520, (2003).

K. Adcox, S. Esumi, Y. Miake, *et al.*, PHENIX detector overview, Nucl.Instrum.Meth.**A499** :469-479, (2003).

S. Nikolaev, Y. Miake, *et al.*, Photon flow in 158-A-GeV Pb + Pb collisions, Nucl.Phys.**A715**:579-582, (2003).

S.S. Adler, S. Esumi, Y. Miake, *et al.*, Absence of suppression in particle production at large transverse momentum in s(NN)**(1/2) = 200-GeV d + Au collisions, Phys.Rev.Lett.**91**:072303, (2003).

A. Drees, S. Esumi, Y. Miake, *et al.*, Heavy ion collisions at collider energies: insights from PHENIX, Pramana 60:639-650, (2003).

S.S. Adler, S. Esumi, Y. Miake, *et al.*, Suppressed π^0 production at large transverse momentum in central Au + Au collisions at s(NN)**1/2 = 200 GeV, Phys.Rev.Lett.**91**:072301, (2003).

Bedangadas Mohanty, Y. Miake, *et al.*, Particle density fluctuations, Nucl.Phys.**A715**:339-348, (2003).

K. Adcox, S. Esumi, Y. Miake, *et al.*, Centrality dependence of the high p(t) charged hadron suppression in Au+Au collisions at s(NN)**(1/2) = 130-GeV, Phys.Lett.**B561**:82-92, (2003).

M.M. Aggarwal, Y. Miake, *et al.*, Centrality dependence of charged neutral particle fluctuations in

158-A-GeV Pb-208 + Pb-208 collisions, Phys.Rev.**C67**:044901, (2003).

S.S. Adler, S. Esumi, Y. Miake, *et al.*, Mid-rapidity neutral pion production in proton proton collisions at S**(1/2) = 200-GeV, Phys.Rev.Lett.**91**:241803, (2003).

S.S. Adler, S. Esumi, Y. Miake, *et al.*, Elliptic flow of identified hadrons in Au+Au collisions at s(NN)**(1/2) = 200-GeV, Phys.Rev.Lett.**91**:182301, (2003).

S.S. Adler, S. Esumi, Y. Miake, *et al.*, Scaling properties of proton and anti-proton production in s(NN)**(1/2) 200-GeV Au+Au collisions, Phys.Rev.Lett.**91**:172301, (2003).

D. Adamova, S. Esumi, *et al.*, Event by event fluctuations of the mean transverse momentum in 40, 80 and 158 A GeV/c Pb - Au collisions, Nucl.Phys.**A727**, 97-119, (2003).

D. Adamova, S. Esumi, *et al.*, Enhanced production of low mass electron pairs in 40-AGeV Pb+Au collisions at CERN SPS, Phys.Rev.Lett.**91**, 042301-042305 (2003).

D. Adamova, S. Esumi, *et al.*, Universal pion freezeout in heavy ion collisions, Phys.Rev.Lett.**90**, 022301-022305, (2003).

D. Adamova, S. Esumi, *et al.*, Beam energy and centrality dependence of two pion Bose-Einstein correlations at SPS energies, Nucl.Phys.**A714**, 124-144, (2003).

ATOMIC AND SOLID STATE PHYSICS, AND CLUSTER SCIENCE

I. Arai , S. Shimakura, K. Hino, T. Miyazaki and S.-M. Lee, Secondary Electron Emission from Cu Surface by Bombardment of Cu Cluster Ions, Transactions of the Materials Research Society of Japan, **28**, 859-862, (2003).

K. Teranishi, T. Miyazaki, I. Arai and S.-M. Lee, Cluster Abundance Spectra of Low Melting Temperature Metals Produced by Bombardment of 6 keV Xe Atoms, Transactions of the Materials Research Society of Japan, **28**, 863-866, (2003).

J.A. Macdonald, I. Arai, *et al.*, Apparatus for a search for T-violating muon polarization in stopped-kaon decays, Nucl. Instr. and Meth., **A506**, 60-91, (2003).

E. Takayama-Muromachi, T. Drezen, M. Isobe, N.D. Zhigadlo, K. Kimoto, Y. Matsui, E. Kita, New ferromagnets of $Sr_8ARe_3Cu_4O_{24}$(A=Sr, Ca) with an ordered perovskite structure, J. Solid. State Chem. **175** 94-103, (2003).

H. Kudo, K. Takeda, T. Suguri, W. Iwazaki, C. Sakurai, I. Arano, S. Numazawa, Electron loss from

fast partially-stripped C and O ions incident on crystal targets, S. Seki, Nucl. Instrum. and Methods **B207**, 283-290, (2003).

M. Onoda and I. Amemiya, Quasi-one-dimensional polaronic states due to the preferential reduction in the $Li_{1+x}V_3O_8$ insertion electrode, J. Phys.: Condens. Matter, **Vol. 15**, No. 19, pp. 3079-3093 (2003).

U. Manju, S. R. Krishnakumar, S. Ray, S. Raj, M. Onoda, C. Carbone and D. D. Sarma, Electron spectroscopic investigation of metal-insulator transition in $Ce_{1-x}Sr_xTiO_3$, Proc. Indian Acad. Sci. (Chem. Sci.), **Vol. 115**, No. 5 & 6, pp. 491-498 (2003).

K. Okazaki, H. Wadati, A. Fujimori, M. Onoda, Y. Muraoka and Z. Hiroi, Photoemission study of the metal-insulator transition in VO_2/TiO_2(001): Evidence for strong electron-electron and electron-phonon interaction, Phys. Rev. B **Vol. 69**, pp. 165104-1 - 165104-7 (2004).

Changqing Li, K.Kondo, T.Makimura and K.Murakami, Increase of 1.5mm luminescence from cryogenic temperature to room temperature from Er-doped SiO2 films with Si nanocrystallites fabricated by laser ablation, Jpn. J. Appl. Phys. **42**, 3432 (2003).

T.Makimura, K.Kondo, H.Uematsu, C.Li and K.Murakami, Optical excitation of Er ions with 1.5mm luminescence via the luminescent state in Si nanocrystallites embedded in SiO_2 matrices, Appl. Phys. Lett. **83**, 5422 (2003).

H.Uematsu, K.Kondo, Changqing Li, T.Makimura and K.Murakami, Optical excitation bands of Er doped SiO2 films with Si nanocrystallites and energy transfer mechanism to Er ions, 6th Int. Symp. on photoreaction control and photofunctional materials, Oct. 2003, Tsukuba, P-47, (2003).

M. Kurosawa, S. Shimano, K. Shima, S. Ishii, T. Nakajima and T. Kato, Quantitative PIXE Analysis of Single Fluid Inclusions in Quartz Vein: Chemical Composition of Hydrothermal Fluids Related to Granite, Nucl. Instrum. and Methods **B210** :464-467, (2003).

K. Awazu, S. Ishii, K. Shima, S. Roorda, and J.L. Brebner, Structure of Latent Tracks Created by Swift Heavy-ions of Amorphous SiO_2 and Zinc Phosphate Glass, Jpn. J. Appl. Phys. **42**:3950-3957, (2003).

K. Nomura, T. Nakanishi, Y. Ohki, K. Awazu, M. Fujimaki, S. Ishii and K. Shima, Structural change induced in TiO2 by swift heavy ions and its application to three-dimensional lithography, Phys. Rev. **B 68**:064106-1-064106-8, (2003).

M. Kurosawa, S. Shimano, K. Shima, S. Ishii, and T. Kato, Quantitative trace element analysis of single fluid inclusions by proton-induced X-ray emission (PIXE): application to fluid inclusion in

hydrothermal quartz, Geochimica et Cosmochimica Acta. **67**:404-419, (2003).

H. Tanimoto, T. Yamada, and H. Mizubayashi, Characteristic Mechanical Properties of High-Density Nanocrystalline Gold, Proc. of Int. Conf. on Advanced Technology in Experimental Mechanics 2003 (ATEM'03), Nagoya Congress Center, Nagoya, Japan, 10-12 Sept., 2003, ed. by Y. Akiniwa et al., OS06W0396(6pages).

H. Tanimoto, N. Yagi, T. Yamada, and H. Mizubayashi, Characterization and Mechanical Properties of High-Density Nanocrystalline Copper, Proc. of Int. Conf. on Advanced Technology in Experimental Mechanics 2003 (ATEM'03), Nagoya Congress Center, Nagoya, Japan, 10-12 Sept., 2003, ed. by Y. Akiniwa et al., OS06W0399(6pages).

6. THESES

Ph. D. Theses

Kenichiro Satou	An experimental study of shell effects of interacting nuclei on heavy-ion fusion reactions

M. Sc. Theses

Shigeto Kaminaga	Identified hadron spectra in p+p collisions at $\sqrt{s}$ NN=200GeV
Masahiro Konno	Development and construction of aerogel Cherenkov detector for the RHIC-PHENIX experiment
Hideyuki Arai	Effect of negatively biased disc to electron cyclotron resonance plasma
Satoshi Takagi	Simulation study for aerogel Cherenkov counter at RHIC-PHENIX
Masanori Kubo	Absorption of silicon atoms on gold clusters
Naoko Yoshimaru	The ^{6}Li(d,p)^{7}Li reaction with polarized deuterons at an incident energy of 90keV
Maya Shimomura	High pT charged hadron analysis in 200 GeV Au+Au collisions at RHIC-PHENIX
Yasushi Takanashi	Interaction of highly charged ion with matter
Hiroyuki Ishiguro	Measurement of energy dependence of total reaction cross section of ^{12}C+p system around (p,n) threshold energy
Takahiro Suzuki	Collision-induced nonlinear ionization by MeV atom clusters
Masaru Nagata	Resonant coherent excitation observed with electrons lost from fast ions

7. SEMINARS

Date		Title and *Speaker*
2003		
April	23	Physics for unstable nuclei; *A. Ozawa (Osaka Univ.)*
June	4	The mysterious neutral particle, does it really exist ?; *M. Sakai (Tokyo Univ.)*
Oct.	8	Perspectives of characterization of semiconductor devices by using high intensity slow positron beam; *A. Uedono (Univ. of Tsukuba)*
Nov.	12	Structure of latent tracks in titanium dioxide created by swift heavy ions and micro-fabrication using ion beams *K. Awazu (AIST)*
Nov.	19	RI beam factory project in RIKEN and storage ring; *A. Ozawa (Univ. of Tsukuba)*
Dec.	17	An experimental study of shell effects of interacting nuclei on heavy-ion fusion reactions; *K. Satou (Univ. of Tsukuba)*
Dec.	24	Identified hadron spectra in p+p collisions at $\sqrt{s}$ NN=200GeV; *Y. Kaminaga (Univ. of Tsukuba)* Development and construction of aerogel Cherenkov detector for the RHIC-PHENIX experiment; *M. Konno (Univ. of Tsukuba)* Effect of Negatively Biased Disc to Electron Cyclotron Resonance Plasma; *H. Arai (Univ. of Tsukuba)*
2004		
Jan.	14	Simulation study for Aerogel Cherenkov Counter at RHIC-PHENIX; *T. Takagi (Univ. of Tsukuba)* Absorption of silicon atoms on gold clusters; *M. Kubo (Univ. of Tsukuba)* The ^{6}Li(d,p)^{7}Li reaction with polarized deuterons at an incident energy of 90keV; *N. Yoshimaru (Univ. of Tsukuba)*
Jan.	21	Recent progress of studies on nuclear structure by using fast RI beam; *T. Motobayashi (RIKEN)*
Jan.	28	High pT charged hadron analysis in 200 GeV Au+Au collisions at RHIC-PHENIX; *M. Shimomura (Univ. of Tsukuba)* Interaction of highly charged ion with matter; *Y. Takanashi (Univ. of Tsukuba)* Measurement of energy dependence of total reaction cross section of ^{12}C+p system around (p,n) threshold energy; *H. Ishiguro (Univ. of Tsukuba)*
Feb.	25	Pursuing a Penta-quark State; *C. Rangacharyulu (Univ. of Saskatchewan, Canada)*
Mar.	31	FRS and Super-FRS - Present and Future of the GSI program with radioactive nuclear beams; *K. Suemmerer (GSI)*

8. SYMPOSIA

Unstable nuclei and nuclear synthesis with storage ring

12 March 2004

Tandem Accelerator Center, room C305, University of Tsukuba

1. Opening : *A.Ozawa (Univ. of Tsukuba)*
2. RIBF : *Y.Yano (RIKEN)*
3. Experiments at RIBF : *T.Motobayashi (RIKEN)*
4. BIG-RIPS and beam transport system : *T.Kubo (RIKEN)*
5. TARN II : *T.Kikuchi (CNS)*
6. Trigger system : *A.Ozawa (Univ. of Tsukuba)*
7. Measurements of mass and life time with TARN II : *T.Otsubo (Niigata Univ.)*
8. Internal target experiments with TARN II : *T.Onishi (RIKEN)*
9. Cluster structure in excited states of Be isotope : *M.Ito (Univ. of Tsukuba)*
10. Mass formula and r-process nuclear synthesis : *H.Koura (RIKEN)*
11. Storage ring and cluster physics : *I.Arai (Univ. of Tsukuba)*
12. Projects for RI beam physics in China : *W.Q.Shen (SINR)*
13. Search for proton halo for ^{27,28}P : *H. Zhang (CIAE)*
14. Production of unstable nucleus ^{8}Li at UTTAC : *Y.Tagishi (Univ. of Tsukuba)*
15. Measurements of magnetic moments for unstable nuclei at UTTAC : *K.Matsuta (Osaka Univ.)*
16. Study of nuclear synthesis at UTTAC : *T.Hayakawa (JAERI)*
17. β-ray angular distribution measurement on ^{20}F at UTTAC : *T.Nagatomo (Osaka Univ.)*
18. Closing : *Y.Tagishi (Univ. of Tsukuba)*

Electronic excitation and related phenomena in atomic collisions

22-23 March 2004

Tandem Accelerator Center, room C305, University of Tsukuba

1. Opening : *H.Kudo (Univ. of Tsukuba)*
2. Correlation between multiply ionized state measurement and resolving process of C_{60} Induced by fast ion bombardment : *A.Itoh (Kyoto Univ.)*
3. Production of C_{60} and measurement of their decay process using a storage ring : *S.Tomita (Univ. of Tsukuba)*
4. Present status of cluster ion acceleration at TIARA : *Y.Saito (JAERI, Takasaki)*

5. Energy transfer and electron emission induced by several atomic ions : *T.Kaneko (Okayama Univ. of Science)*
6. Review on fast cluster ion acceleration and related phenomena : *K.Sasa (Univ. of Tsukuba)*
7. Secondary electron production induced by cluster collision : *I.Arai (Univ. of Tsukuba)*
8. *In situ* observation of materials during ion bombardments : *H.Tsuchida (Nara Women's Univ.)*
9. 3-dimensional nano-fabrication of materials by fast heavy ion bombardments : *K.Awazu (NI-AIST)*
10. Comment from the viewpoint of application of cluster : *J.Matsuo (Kyoto Univ.)*
11. Charge states of ions in tandem energy region : *K.Shima (Univ. of Tsukuba)*
12. Large angle and single scattering at solid surface : *Y.Kido (Univ. of Ritsumei)*
13. Cluster ion bombardment on high polymer material : *K.Hirata (NIAIST)*
14. Effective charge model in fast atomic cluster : *H.Kudo (Univ. of Tsukuba)*
15. Closing : *K.Shima (Univ. of Tsukuba)*

9. LIST OF PERSONNEL

Accelerator Center

H. Kudo	Director, Professor
K. Shima	Associate Professor
T. Komatsubara	Assistant Professor
K. Sasa	Assistant Professor
S. Ishii	Mechanical Technician
H. Kimura	Computer Technician
H. Oshima	Electric Technician
Y. Tajima	Mechanical Technician
T. Takahashi	Electric Technician
Y. Yamato	Electric Technician
He Ming	Research Fellow
M. Yamaguchi	Research Fellow
K. Suzaki	Technical Assistant
M. Ohki	Administrative Stuff

Steering Committee

H. Kudo	Chairperson, Tandem Accelerator Center
R. Kanzaki	Inst. of Biological Science
T. Komatsubara	Tandem Accelerator Center
Y. Miake	Inst. of Physics
Y. Nagashima	Inst. of Basic Medical Science
M. Onoda	Inst. of Physics
R. Seki	Inst. of Chemistry
K. Shima	Inst. of Applied Physics
Y. Tagishi	Inst. of Physics
K. Takita	Inst. of Material Science
K. Yabana	Inst. of Physics

Scientific Guests and Fellows

K. Awazu	National Lab. Advanced Industrial Science and Technology
M. Fujimaki	Waseda Univ.
Y. Nagasawa	Waseda Univ.
I. Daito	Nagoya Univ.
M. Iio	Miyazaki Univ.
T. Hayakawa	JAERI
T. Shizuma	JAERI
H. Sasaki	Tsukuba Nano-Tech.
H. Ishiyama	KEK
H. Miyatake	KEK
M. Tanaka	KEK
N. Yoshikawa	KEK
Y. Watanabe	KEK
T. Miura	KEK
K. Masumoto	KEK
K. Bessho	KEK
H. Matsumura	KEK
He Ming	China Institute of Atomic Energy
K. Furuno	Emeritus Professor
Q.B. Wang	KEK

Research Members

Inst. of Physics

Y. Aoki	I. Arai	S. Esumi	S. Katoh	T. Komatsubara
Y. Miake	N. Okumura	M. Onoda	A. Ozawa	K. Sasa
Y. Tagishi	M. Yamaguchi			

Inst. of Applied Physics

E. Kita	H. Kudo	K. Shima	A. Uedono	H. Yanagihara

Inst. of Material Science

T. Koyano	H. Mizubayashi	K. Takita	H. Tanimoto

Inst. of Geoscience

R. Anma	M. Kurosawa

Inst. of Chemistry

R. Seki	K. Sueki

Inst. of Basic Medical Science

Y. Nagashima

Graduate Students

Doctoral Degree Programs of Physics

J. Hasegawa	K. Satoh

Doctoral Degree Programs of Engineering

T. Hao	B. Hou	N. Ookubo	N. Umeda

Doctoral Degree Programs of Pure and Applied Science

S. Hamajima	T. Harigae	A. Hatanaka	S. Igarashi	T. Ikeda
Y. Ishibashi	M. Konno	H. Masui	K. Masuo	K. Miyakawa
M. Nagata	Y. Nagata	M. Nakazumi	M. Narisawa	M. Oka
S. Sakai	J. Sawahata	K. Shibata	Y. Shimizu	M. Shimomura
T. Suzuki	S. Takagi	H. Tokano	N. Yagi	

Master's Degree Programs of Science and Engineering

H. Arai	K. Goto	T. Hinuma	M. Iijima	H. Ishiguro
S. Kaminaga	T. Kawagishi	M. Kubo	S. Miyasaka	T. Muto
T. Ooki	T. Shimada	T. Shinba	T. Shojo	T. Suzuki
Y. Takanashi	Y. Tsuruga	A. Ueki	H. Uematsu	N. Yoshimaru

Master's Degree Programs of Environmental Science

T. Matsuhiro

Under Graduates

Y. Endo	K. Fujiwara	M. Furutani	K. Ikeuchi	T. Ishikawa
K. Miki	S. Oono	Y. Oono	K. Shibata	K. Takao
R. Uchiyama	K. Uehara	H. Wakamatsu	K. Yamagishi	